

# SCIENTIFIC REPORTS



OPEN

## First *in situ* evidence of wakes in the far field behind offshore wind farms

Andreas Platis<sup>1</sup>, Simon K. Siedersleben<sup>2</sup>, Jens Bange<sup>1</sup>, Astrid Lampert<sup>3</sup>, Konrad Bärfuss<sup>3</sup>, Rudolf Hankers<sup>3</sup>, Beatriz Cañadillas<sup>4</sup>, Richard Foreman<sup>4</sup>, Johannes Schulz-Stellenfleth<sup>5</sup>, Bughsin Djath<sup>5</sup>, Thomas Neumann<sup>4</sup> & Stefan Emeis<sup>1</sup> 

Received: 3 May 2017


Accepted: 15 January 2018

Published online: 01 February 2018

More than 12 GW of offshore wind turbines are currently in operation in European waters. To optimise the use of the marine areas, wind farms are typically clustered in units of several hundred turbines. Understanding wakes of wind farms, which is the region of momentum and energy deficit downwind, is important for optimising the wind farm layouts and operation to minimize costs. While in most weather situations (unstable atmospheric stratification), the wakes of wind turbines are only a local effect within the wind farm, satellite imagery reveals wind-farm wakes to be several tens of kilometres in length under certain conditions (stable atmospheric stratification), which is also predicted by numerical models. The first direct *in situ* measurements of the existence and shape of large wind farm wakes by a specially equipped research aircraft in 2016 and 2017 confirm wake lengths of more than tens of kilometres under stable atmospheric conditions, with maximum wind speed deficits of 40%, and enhanced turbulence. These measurements were the first step in a large research project to describe and understand the physics of large offshore wakes using direct measurements, together with the assessment of satellite imagery and models.

Offshore wind farms contribute a considerable fraction to the production of renewable electrical energy. In 2015, 12 GW of offshore wind-energy capacity was successfully installed in Europe<sup>1</sup>. In Germany offshore capacity is expected to reach 7.8 GW by 2020<sup>2</sup>. In Europe, it is expected to reach 73 GW by 2030<sup>3</sup>. A significant number of these new installations will be in the North and Baltic Seas<sup>4,5</sup>.

For an optimal use of the marine areas<sup>6</sup>, wind farms are constructed at favourable locations and in clusters (see Fig. 1). As wind farms are built to extract considerable kinetic energy from the atmosphere, a downwind wake region is formed, characterised by a reduced mean wind speed and, additionally, an enhanced level of turbulence. Most research in this area focuses on wakes behind single turbines, and on the wake interaction from a larger number of turbines within one and the same wind farm<sup>7</sup>. Only some experimental and recent numerical studies consider the wakes of entire wind farms and the impact of wakes on neighbouring downwind wind farms on a larger spatial scale<sup>6,8–22</sup>. The spatial extension of wakes from offshore wind farms is not understood to the extent that the length of a wake may be predicted based on all influencing parameters, such as wind-farm characteristics, atmospheric conditions, and sea state<sup>23</sup>. The most efficient mechanism for wake recovery is the vertical transfer of momentum from higher atmospheric layers downwards<sup>24</sup>, implying atmospheric turbulence to be the decisive parameter governing wake recovery<sup>16,25,26</sup>. Atmospheric turbulence is primarily produced from vertical wind speed gradients (mechanical turbulence) and thermal convection (thermal turbulence). Over rough land surfaces, both mechanical and thermal turbulence are abundant and wakes are usually short (at maximum a few kilometres in length). Much less turbulence is produced at sea, because of the small surface friction and weak temperature gradients, since the response of the ocean to solar radiation is slow. The wakes from wind farms over the sea are, therefore, expected to extend further downwind than over land, especially under a stably stratified flow, which inhibits thermally produced turbulence<sup>5,27</sup>. Since offshore wind farms are located close to the coastline (i.e. a distance less than 100 km to the coast), warm air from land may flow over the colder sea to generate stable stratification, especially during spring and summer. While not yet verified by direct *in situ* measurements, analytical<sup>20,24,28</sup> and numerical flow models<sup>13,22,29,30</sup> predict the length of far wakes up to 100 km in

<sup>1</sup>University of Tuebingen, ZAG, Environmental Physics, 72074, Tuebingen, Germany. <sup>2</sup>Karlsruhe Institute of Technology (KIT), Institute of Meteorology and Climate Research (IMK-IFU), 82467, Garmisch-Partenkirchen, Germany. <sup>3</sup>Technische Universität Braunschweig, Institute of Flight Guidance, 38108, Braunschweig, Germany. <sup>4</sup>UL DEWI - UL International GmbH, 26382, Wilhelmshaven, Germany. <sup>5</sup>Helmholtz-Zentrum Geesthacht (HZG), Institute of Coastal Research, 21502, Geesthacht, Germany. Correspondence and requests for materials should be addressed to A.P. (email: @uni-tuebingen.de)

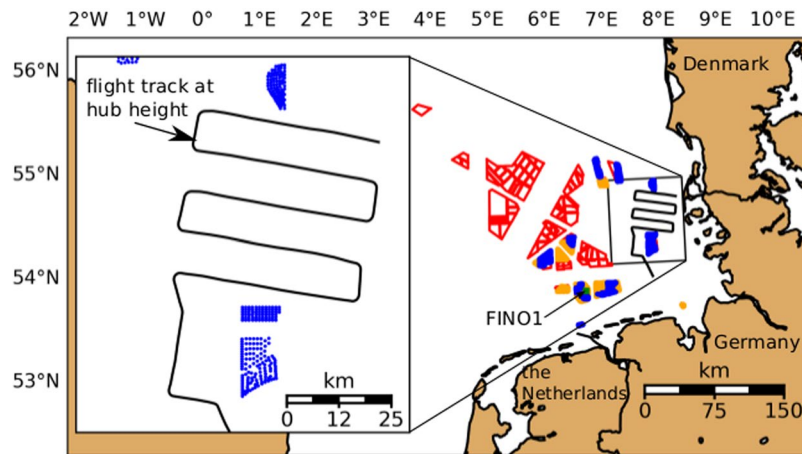


**Figure 1.** Distribution of offshore wind farms in the German Bight. Blue regions are farms currently in operation and orange regions are those wind farms that are under construction or have been approved (as of 2017). Red polygons indicate farms with a submitted application (as of 2016). The plot on the left side indicates the flight track of Flight 7 on September 10, 2016. The blue dots represent the location of the individual wind turbines.

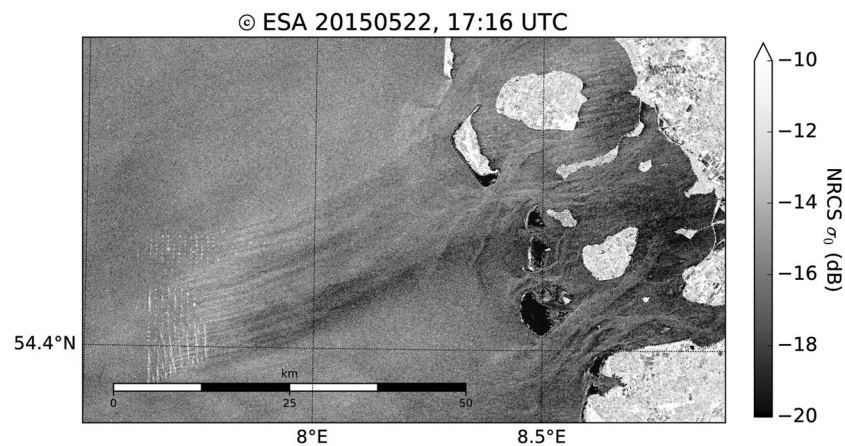


**Figure 2.** Example of a SENTINEL-1A satellite SAR image (Copernicus Sentinel data [2015]) acquired over the North Frisian Coast in the German Bight on May 22, 2015 at 17:16 UTC with westerly winds created by Matplotlib<sup>37</sup>. The white dots on the lower left are radar signatures from windfarm turbines of the three wind parks Amrumbank West, Nordsee Ost and Meerwind Süd/Ost. A wake of reduced wind speed generated by the wind turbines is indicated by darker streaks downwind of the wind farms.

stable stratification. Further, satellite images from synthetic aperture radar (SAR) suggest the existence of wake lengths of several tens of kilometres (Fig. 2) under stable atmospheric conditions, i.e., in the absence of thermally produced turbulence<sup>31,32</sup>. However, such images are rare as the repeat cycle of the satellite is about 11–12 days and lack some observational verification in addition.

Verification of numerical and analytical models and SAR is difficult because *in situ* measurements of offshore wind-farm wakes only exist in the near field, directly behind single turbines and wind farms<sup>22,33,34</sup>. In fact, *in situ* measurements of far-field wakes at hub height on a larger scale behind whole offshore wind farms are not currently available. The German research project WIPAFF (WInd Park Far Field)<sup>35</sup> has performed the first aircraft measurements of the far wakes of wind farm clusters in the North Sea. We summarise the first measurements here and compare them with numerical simulations of the Weather Research and Forecasting model (WRF)<sup>36</sup>.

## Methods

Table 1 gives an overview of all 41 measurement flights performed during the WIPAFF project with the Dornier DO 128 aircraft (Fig. 3) in 2016 and 2017 over the German Bight. The starting points of all flights were Wilhelmshaven, Borkum or Husum airport. The aircraft airspeed during the measurements was  $66 \text{ m s}^{-1}$ .

**Meteorological data.** The wind vector measurement is performed by measuring the flow speed and flow angles at the aircraft nose with a multi-hole flow probe (Figs 3 and 4), as well as the aircraft's motion and orientation in the geodetic coordinate system with an inertial measurement unit (IMU) and the ground speed vector

Flight code	Date (dd. mm. yyyy)	Start Time (UTC)	End Time (UTC)	WS ( $\text{m s}^{-1}$ )	Wind dir ( $^{\circ}$ )	Wake length (km)	Atmospheric stratification
September							
Flight 1	06.09.2016	14:13	17:20	7	190	25	stable
Flight 2	07.09.2016	09:25	13:00	4	210	20	stable
Flight 3	07.09.2016	10:00	14:00	4	190	at least 10	stable
Flight 4	08.09.2016	10:38	14:25	8	120	at least 40	stable
Flight 5	09.09.2016	10:54	14:50	6	240	at least 45	stable
Flight 6	09.09.2016	15:43	19:17	6	250	at least 5	unstable
<b>Flight 7</b>	<b>10.09.2016</b>	<b>07:30</b>	<b>11:30</b>	<b>7</b>	<b>190</b>	<b>45</b>	<b>stable</b>
Flight 8	10.09.2016	12:05	16:00	4	190	at least 20	stable
March–April							
Flight 1	30.03.2017	15:57	19:02	15	240	70	stable
Flight 2	31.03.2017	15:36	19:00	13	180	50	stable
Flight 3	05.04.2017	15:42	16:34	14	310	10	neutral
Flight 4	06.04.2017	15:29	18:22	8	310	at least 10	unstable
Flight 5	09.04.2017	12:36	16:07	7	220	at least 50	stable
Flight 6	09.04.2017	16:32	20:12	4	200	n.a.	stable
Flight 7	11.04.2017	11:25	15:10	8	300	5	unstable
Flight 8	11.04.2017	16:12	20:04	8	240–280	25	neutral
Flight 9	13.04.2017	13:35	17:39	16	290	10	neutral
May–June							
Flight 1	17.05.2017	12:35	16:28	8	110	n.a.	stable
Flight 2	17.05.2017	17:16	21:22	12	120	55	stable
Flight 3	23.05.2017	15:42	16:34	5	250	at least 25	stable
Flight 4	23.05.2017	13:18	17:15	11	310	at least 35	neutral
Flight 5	24.05.2017	07:40	11:34	8	300	n.a.	unstable
Flight 6	24.05.2017	12:13	16:11	9	270	5	unstable
Flight 7	27.05.2017	09:57	13:58	10	150	at least 50	stable
Flight 8	27.05.2017	14:39	18:36	12	140	55	stable
Flight 9	31.05.2017	09:58	13:46	8	290	2	unstable
Flight 10	31.05.2017	15:00	18:50	9	290	0	unstable
Flight 11	01.06.2017	08:55	12:54	6	300	0	unstable
Flight 12	02.06.2017	08:55	12:40	4	170	at least 15	stable
August							
Flight 1	08.08.2017	10:35	14:35	9	80	at least 35	stable
Flight 2	08.08.2017	15:06	19:07	14	80	at least 55	stable
Flight 3	09.08.2017	10:34	14:37	15	210	n.a.	unstable
Flight 4	09.08.2017	15:09	19:05	13	240	n.a.	unstable
Flight 5	10.08.2017	12:49	16:54	5	330	n.a.	unstable
Flight 6	14.08.2017	12:08	16:07	8	150	at least 35	neutral
Flight 7	14.08.2017	16:40	20:31	7	120	50	stable
Flight 8	15.08.2017	09:22	13:15	8	180	30	stable
Flight 9	17.08.2017	08:06	12:10	12	160	40	stable
October							
Flight 1	14.10.2017	14:59	18:40	15	260	n.a.	stable
Flight 2	15.10.2017	09:05	13:09	14	200	n.a.	unstable
Flight 3	15.10.2017	13:52	17:50	13	190	at least 25	stable

**Table 1.** Full list of all measurement flights conducted within the WIPAFF project. Wake length: Assessed wake distance with a wind speed deficit with more than  $0.1 \text{ m s}^{-1}$  compared to the undisturbed flow. Wake lengths measured during a flight pattern that did not cover the full extent of the wake are indicated with “at least”. Some flights focused on the processes above wind farms, hence, no data is available describing the length of the wakes, for such flights the wake length is not available (n. a.). Atmospheric stratification: Estimation of the atmospheric stability by analysing the airborne measured potential temperature vertical profiles between near surface (30 m) and hub height (100 m), which were flown close to the wind farm. WS means wind speed. Bold text marks the investigated flight in this study.



**Figure 3.** The research aircraft Dornier DO-128 of the Technische Universität Braunschweig.

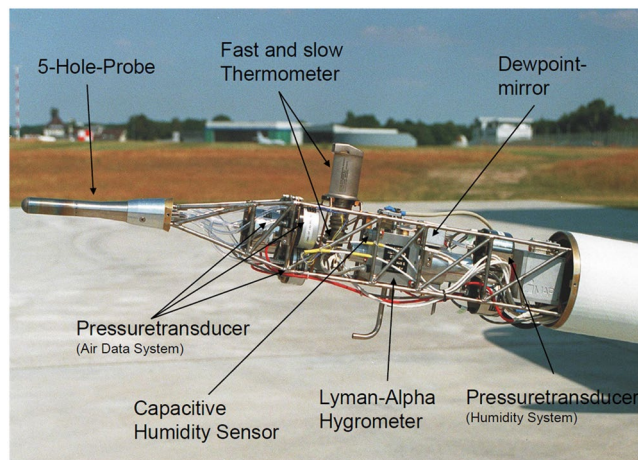


**Figure 4.** Instrumentation of the nose boom of the DO-128.

with a combination of IMU and GPS. More details on the aircraft's sensor system can be found in<sup>38–40</sup>. The total duration of a measurement flight lasted 2 to 4 h, and the main downwind flight pattern lasted about 1 h as shown in Fig. 1. The data acquisition rate is 100 Hz. Given the information of these sensors, the wind speed can be calculated as

$$\mathbf{u} = \mathbf{v}_{\text{gs}} + \mathbf{M}(\mathbf{v}_{\text{tas}} + \boldsymbol{\Omega} \times \mathbf{s}), \quad (1)$$

where  $\mathbf{u}$  is the wind speed vector,  $\mathbf{v}_{\text{gs}}$  is the ground speed vector,  $\mathbf{v}_{\text{tag}}$  is the airspeed vector,  $\mathbf{M}$  is the rotation matrix from the aircraft's fixed coordinate system with respect to the geodetic coordinate system, and  $\mathbf{s}$  is the lever arm between the IMU and the flow probe. The rate of angular rotation vector  $\boldsymbol{\Omega}$  contains the angular velocities of the aircraft fixed coordinate system relative to the geodetic coordinate system, and is among the primary output data of the IMU. A detailed description of the airborne wind speed measurement, including an error estimation, can be found in<sup>33</sup> and<sup>41</sup>.

The turbulent kinetic energy, TKE is calculated by

$$\text{TKE} = \frac{1}{2}(\sigma_u^2 + \sigma_v^2 + \sigma_w^2) \quad (2)$$

with  $\sigma_u$  representing the fluctuations of the wind vector component  $u$ ,  $\sigma_v$  of the component  $v$  and  $\sigma_w$  of  $w$ .

For example,  $\sigma_u$  is computed as

$$\sigma_u^2 = \frac{1}{N-1} \sum_{n=1}^N (u(n) - \bar{u})^2, \quad (3)$$

where  $N$  is the number of data points within the moving data window and  $\bar{u}$  denotes the average of  $u$  within the window. To study the variability of the wind speed field and TKE, it is necessary to determine a suitable horizontal length scale over which to compute the mean wind speed and the fluctuation  $\sigma$  of the wind components within

sub-legs (data windows) along a flight leg. The method is the so-called moving-average method. Given a series of values (the total data point along one flight leg) and a fixed subset size (sub-legs), the first element of the moving average is obtained by taking the average of the initial fixed subset of the time series. The subset is then modified by a forward shift, so that the first value of the series is excluded, while including the next value following the original subset in the series to create a new subset of numbers for averaging. The process is repeated over the entire data series.

However, sub-legs not exceeding the largest eddies in size insufficiently sample the dynamic wind field, causing a systematic error by systematically under- or overestimating the turbulent wind and its standard deviation<sup>42</sup>. This sampling error can be estimated by the expression stated in<sup>43</sup> and<sup>44</sup> representing the absolute systematic statistical uncertainty of the standard deviation  $\sigma_u$  related to a single flight leg on which  $\sigma_u$  was calculated,

$$\Delta\sigma_u = 2 \frac{L_u}{P_l} \cdot \sigma_u, \quad (4)$$

where  $L_u$  is the integral length scale<sup>45</sup> of  $u$  and  $P_l$  the averaging length. The  $L_u$  can be explained as the correlation time, i.e. the persistence or memory of the turbulent flow<sup>46</sup>. The integral time scale  $I_u$  for the wind speed  $u$  is

$$I_u = \int_0^{\tau_1} d\tau \frac{u'(t+\tau) \cdot u'(t)}{u'^2} = \int_0^{\tau_1} d\tau \frac{\text{Cov}_u(\tau)}{\sigma_u^2}, \quad (5)$$

where  $\text{Cov}_u$  represents the covariance of  $u$ , and is calculated by integration from zero lag to the first zero crossing at  $\tau_1$ <sup>47</sup>. The transformation into the  $L_u$  is carried out by multiplication of the  $I_u$  by the aircraft's ground speed, assuming that Taylor's hypothesis of frozen turbulence is valid<sup>45</sup>. For example, the integral length scale for the wind speed  $u$  for Flight 7 is about 90 m. To obtain an error of less than 10% of  $\sigma_u$ , the window length should be at least 1800 m according to Eq. 4. We have defined windows of 2-km width using unweighted means, sequentially shifted through the leg by increments of 0.66 m for a sampling rate of 100 Hz and an aircraft ground speed of 66 m s<sup>-1</sup>. As  $\sigma_u$  is about 0.1 m s<sup>-1</sup> for Flight 7, the error for the measured wind speed  $u$  is 1%.

**Scanning lidar.** We recorded sea surface measurements using a scanning LiDAR-system supported by a navigation grade IMU for registering the measurement points. The effective pulse rate of 22 kHz theoretically provides spatial-point densities of one per metre along, and five per metre perpendicular to, the flight direction for an effective overall measurement rate of about 4.5 kHz. In addition to spatial information, the calibrated echo amplitude is used to compute the reflectance relative to a perpendicular white target at the same distance.

Data have been calculated as the average relative reflectance over 2 s. Fewer measurement points were received within the wake because of the smoother sea surface. In the averaged data set, this resulted in a generally higher reflectance inside the wake caused by more specular reflections.

**Numerical model WRF.** We conducted numerical simulations with the Weather Research and Forecasting Model WRF (Version 3.7.1)<sup>36</sup> using three nested domains with grid size of 15 km, 5 km and 1.7 km. The nesting allows feedback between the nested domains with an update frequency of 20 s for the second domain and 60 s for the first domain. All model domains have 50 vertical levels with a spacing of approximately 40 m at the rotor area. The model top is at 100 hPa (=16 km). The initial and lateral boundary conditions are defined by the European Centre for Medium-Range Weather Forecasts (ECMWF) model operational analysis data at 6-h intervals. The ECMWF data has a grid size of 0.1 degrees (i.e. similar to the grid size of the first domain). The model is initialised at 12 UTC, 9 September 2016 (i.e. 19 h before the first measurements) and integrated for 36 h.

The following parametrizations are used for all domains: The Noah land surface model<sup>48</sup>, the WRF double-moment 6-class cloud microphysics scheme (WDM6<sup>49</sup>), the Rapid Radiative Transfer Model for the GCM scheme for short- and longwave radiation<sup>50</sup> and the Mellor-Yamada-Nakanishi-Niino boundary-layer parametrization<sup>51</sup>. The ocean surface roughness is determined by a modified Charnock relation<sup>52</sup>. In contrast to the two innermost domains, the outermost domain uses the Kain-Fritsch cumulus parametrization scheme<sup>53</sup>.

**Wind farm parameterization.** The grid size of the numerical model WRF is too large to capture the effect of a single wind farm explicitly. Therefore, we use the wind farm parametrization of Fitch *et al.*<sup>13</sup>, which acts as a momentum sink for the mean flow and as a source of turbulence at the height of the rotor. The wind turbines at the wind farms Amrumbank West (AW), Windpark Meerwind Süd/Ost (WM) and Nordsee Ost (OWPN) have a hub height ranging from 90 m to 95 m and a diameter of 120 m up to 126 m. Therefore, the rotor area of the wind turbines intersects with three model levels. The effects of the wind turbine towers on the atmosphere are neglected.

A wind turbine extracts kinetic energy from the atmosphere, with the total extracted fraction from the atmosphere described by the thrust coefficient  $C_T$ . Only a fraction of the extracted kinetic energy is converted into electrical energy as quantified by the power coefficient  $C_p$ . The difference between  $C_T$  and  $C_p$  stems from electrical and mechanical losses, and the production of non-productive drag. By neglecting the electrically and mechanically induced losses and assuming that all non-productive drag is converted into electrical energy, the difference  $C_T - C_p$  describes the amount of kinetic energy that is extracted from the mean flow and then converted into turbulent kinetic energy<sup>13</sup>.

The coefficients  $C_T$  and  $C_p$  are a function of wind speed and depend on the type of turbine<sup>13</sup>. The three wind farms of interest (AW, WM, OWPN) have two different wind turbine types: At AW and WM, Siemens SWT 3.6–120 offshore turbines are installed whereas at OWPN, Senvion 6.2 wind turbines are used, with nominal powers of 3.6 MW and 6.2 MW, respectively. Since  $C_T$  and  $C_p$  for these turbines are unavailable to the public, we adapt coefficients from the wind turbine Siemens SWT 3.6–120 onshore, as these are available online (see <http://>

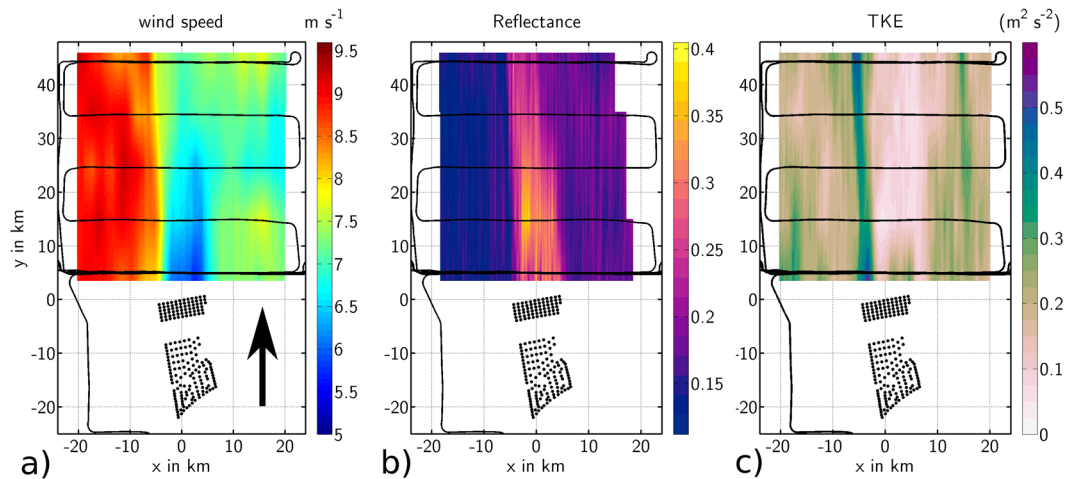


**Figure 5.** (a) Wind speed measurements at hub height (90 m) from the DO 128 flight on September 10, 2016 08:30–09:30 UTC (Flight 7). The wind speed measured along the flight track (black lines) is linearly interpolated perpendicular to the mean wind direction (south 190, indicated by the black arrow). Black dots mark the position of the wind turbines of the wind farms Amrumbank West, Nordsee Ost and Meerwind Süd/Ost. The geographical GPS-coordinates are converted into a Cartesian coordinate system aligned with the mean wind direction (190) for a better comprehension of the orientation and length of the wake. (b) As in Fig. 5a), but for the dimensionless reflectance of the sea surface. A higher reflectance may be interpreted as a lower wind speed near the ocean surface. (c) As in Fig. 5a), but for the TKE.

[www.wind-turbine-models.com/turbines/646-siemens-swt-3.6-120-onshore](http://www.wind-turbine-models.com/turbines/646-siemens-swt-3.6-120-onshore)). The model underestimates the wind at hub height by up to  $1 \text{ m s}^{-1}$ . Furthermore, the parametrisation of Fitch *et al.*<sup>13</sup> neglects the dependence of the power and thrust coefficients on the stability of the atmosphere. Therefore, the power and thrust coefficients chosen in the present study are only a suitable first approximation.

**Measurements of wind-farm wakes in the far field.** *In situ* observations from fixed platforms like FINO 1 are available, but do not provide the spatial sampling required to study the three-dimensional structure of wakes. The institutes involved in the WIPAFF project were aware of these shortcomings in currently available data sources. Therefore, we collected *in situ* data with the research aircraft Dornier DO-128 belonging to the Technische Universität Braunschweig, Germany. Measurement flights delivered wind speed and direction, turbulence, temperature, humidity, surface-temperature and sea-state data at high resolution (sampling frequency 100 Hz), similarly to campaigns documented in<sup>38,39</sup>. A laser scanner was also integrated into the research aircraft to determine sea-surface properties.

We performed 41 measurement flights between September 2016 and October 2017 downwind of wind farm clusters, such as Amrumbank West and Godewind located in the German Bight (Table 1). We discuss the results of Flight 7 on September 10, 2016 here as a typical example for the wake extent during moderate wind speeds of  $7\text{--}10 \text{ m s}^{-1}$  and under stable conditions. Throughout the September 2016 campaign, a dominant high-pressure system was located over Central and Eastern Europe, resulting in the advection of warm sub-tropical air over the German Bight from the south. The warm air over the colder water during the campaign resulted in stable atmospheric stratification (i.e. no thermal turbulence and, therefore, the prevention of convective motion), which is favourable for the generation of long wakes. By vertical profiling of the lower atmosphere with the aircraft, we observed stable conditions over the sea during the September 2016 campaign during 7 flights, where wakes over the whole flight range up to 45 km were detected. In total we detected wakes with a length of at least 10 km during 27 cases, the longest wake length was 70 km (see Table 1). The flight pattern of Flight 7 on September 10 shown in Fig. 5a)–c) measured both the undisturbed air flow and the wake dispersion downwind from the wind farm cluster Amrumbank West, Nordsee Ost and Meerwind Süd/Ost with 90% of the wind turbines running. Several flight legs of 40 km length positioned perpendicular to the mean wind direction and staggered (5, 15, 25, 35, 45 km) behind the wind farm captured both the wake and the adjacent undisturbed air flow at hub height (90 m) of the wind turbines.

Wind speed measurements from Flight 7 are shown in Fig. 5a), where data recorded from individual legs are linearly interpolated, and displayed as coloured contours. Behind the wind farm, a zone of reduced wind speed extended to at least 45 km, with a wind speed deficit up to  $3 \text{ m s}^{-1}$  at 5 km downwind and about  $1 \text{ m s}^{-1}$  at 45 km behind the wind farm resulting in a maximum wind speed deficit of 40%. In this manuscript we refer to wind speed deficit as the difference between the flow within the wake and the undisturbed flow outside of the wake on the western side along each flight leg (where the maximum wind speed was measured) instead of using the wind speed measured upstream of the wind farms as a reference. This definition is necessary because of two reasons. First, the wind speed has a gradient from East to West. Therefore, it would be difficult to define an upstream wind speed. Secondly, the upstream wind speed decreased during field experiment. Hence, using the upstream measured wind speed as reference would lead to an underestimation of the wind speed reduction. The wind

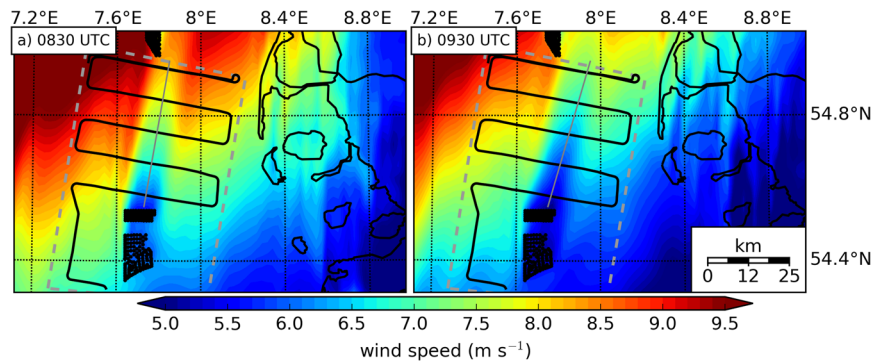


**Figure 6.** (a) WRF model simulation of the wind field at hub height (90 m) for 10 September 2016 08:30 UTC. (b) WRF model simulation for 09:30 UTC on the same day. The flight pattern over the German Bight is marked by the black line, the measurement flight domain according to Fig. 5(a)–(c) by grey dashed line, German and Danish coast by black lines and wind turbines by black dots. Grey line indicates a cross-section of the wind speed, which is displayed in Fig. 7. The figures were generated with Matplotlib<sup>37</sup>.

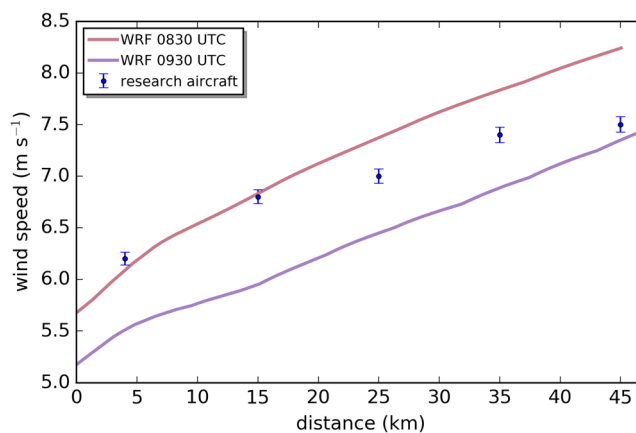


**Figure 7.** Cross-section along the wake as marked in Fig. 6 of the WRF simulations at 08:30 UTC (red) and 09:30 UTC (purple) and the *in situ* data (blue). Error bars indicate the estimated wind measurement error as explained in Section Meteorological data.

speed deficit in the wake is aligned along the mean wind direction. The wake sector has the width of the wind farm (10 km) for the closest flight legs (at 5 km and 10 km downwind) and no pronounced spreading out can be detected with increasing distance from the wind farm.

A lower wind speed results in a smoother water surface. The smoothness of the water surface was measured by laser reflectance aboard the aircraft using the downwards-looking laser scanner (Sect. Methods). The scattering of the signal transmitted by the laser is less diffuse for smoother water, hence, the probability of a specular reflection in the direction of the sensor is higher. This effect of increased reflectance at low wind speeds is well known from microwave radar altimeter studies<sup>54</sup>, which we use to help visualise the far wake and relate to SAR images. As shown in Fig. 5(b), we measured a higher reflectance by a factor of four inside the wake than in the neighbouring region, indicating lower wind speeds in the wake during Flight 7. *In situ* wind speed measurements (Fig. 5a) and laser reflectance (Fig. 5b) both show a wake throughout the whole scanning area of 45 km downwind of the wind farm. Furthermore, Fig. 5(a) and (b) display a horizontal wind speed reduction from west to east (i.e. perpendicular to the mean wind direction) caused by the higher surface friction along the coast, east of the flight path.

**Turbulence in the far wake.** The degree of atmospheric turbulence impacts the efficiency and fatigue loading of a wind turbine<sup>55</sup>. A typical parameter to describe turbulence is the turbulent kinetic energy (TKE) described in Sect. Methods. Measurements of TKE reveal a far downwind dispersion of the turbulence produced by the wind farm and as a result of the mixing of the wake with the undisturbed flow (Fig. 5c). A slender wake of TKE with a width less than 5 km is aligned with the western edge of the wind farm. A stronger horizontal wind speed gradient exists between the decelerated wind field in the wake and undisturbed wind field to the west. The eastern edge of the wake is much less pronounced as a result of the lower wind speeds along the coast. Inside the wake less turbulence is produced due to a lower wind speed than in the undisturbed flow outside the wake, thus TKE is smaller. Moreover, the eastern boundary of the cluster of wind farms is more irregular compared with the western edge (see Fig. 5c). The TKE of  $0.5 \text{ m}^2 \text{ s}^{-2}$  in the wake sector is about five times that in the undisturbed air flow and decays slowly after 10 km to about  $0.3 \text{ m}^2 \text{ s}^{-2}$ . An elevated level of TKE remains at even 45 km downwind

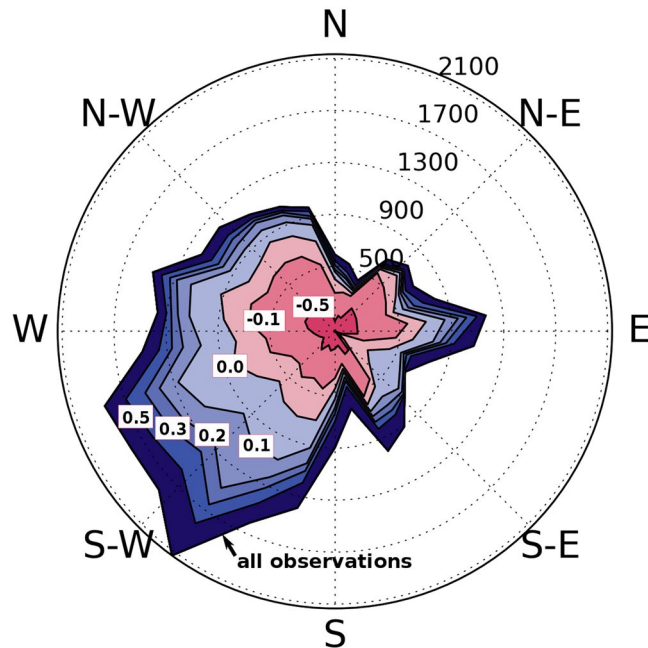


**Figure 8.** Stability wind rose indicating the frequency (number of 10-min intervals per 12° wind direction sector) of atmospheric stability. Lines are labelled in terms of the stability measure  $z/L$ , where  $z$  is the height above ground, and  $L$  is the Monin-Obukhov length. Blue and red shading indicates stable and unstable stratification, respectively. The higher the value the stronger the stability. Data are from the FINO 1 offshore platform in the North Sea for the whole year of 2005 at a height of 60 m above the sea surface. Data is available from <http://fino.bsh.de/>. Only data with wind speeds between the cut-in ( $5 \text{ m s}^{-1}$ ) and cut-off ( $25 \text{ m s}^{-1}$ ) wind speed have been considered.

of the wind farm. Within the eastern part of the wake, the TKE remains lower (below  $0.1 \text{ m}^2 \text{ s}^{-2}$ ) than in the undisturbed flow ( $0.1\text{--}0.25 \text{ m}^2 \text{ s}^{-2}$ ) at least 45 km downwind on account of the lower wind speeds and reduced horizontal wind shear.

**Comparison with model simulations.** We performed numerical simulations of the wake using the wind farm parametrisation of Fitch *et al.*<sup>13</sup> within the Weather Research and Forecasting Model for a grid size of 1.6 km. Operational analysis data from the European Centre for Medium-Range Weather Forecasts (ECMWF) provided the initial and lateral boundary conditions. The model results (Fig. 6) have been obtained for two times at the beginning of the measurement pattern and at the end.

The model simulations reveal a similar structure and orientation of the far wake for the 10 September 2016 as observed by the airborne data (Fig. 6), with a wind speed of about  $6 \text{ m s}^{-1}$  at the first flight leg 5 km downwind (08:30 UTC) and  $7.3 \text{ m s}^{-1}$  at the last flight leg (09:30 UTC) 45 km downwind (Fig. 7). However, the observations indicate higher wind speeds within the wake than the simulations (Fig. 7). This finding is consistent with the wind speed observations taken upwind of the wind farm where the model is underestimating the wind speed. Consequently, the wind speed within the wake has to be lower than the *in situ* data, otherwise the wind farm parameterization would underestimate the wind speed deficit induced by the wind farm.

The wind speed averaged over the measurement domain during the flight decreases from approximately  $7 \text{ m s}^{-1}$  (08:30 UTC) to  $5 \text{ m s}^{-1}$  (09:30 UTC), which is consistent with flight measurements. The attenuated wind field along the coast observable in the simulations matches well with *in situ* observations (Fig. 5a).

## Discussion

As expected from the results of remote sensing observations, numerical and analytical studies<sup>13,20,22,24,28,30–32,56,57</sup>, the wind speed deficits downwind of offshore wind farms tend to be larger in stable than in unstable conditions, and the lengths of wakes are longer. Likewise, our aircraft measurements show strong indications for longer wakes for all flights under stable situations, whereas wakes were not observed far away from the farms during unstable conditions (see Table 1). These first airborne *in situ* results fortify assumptions from the previous studies. A further detailed analysis of the stratification and wake length will be presented in a future work, as an exact stability analysis is very complex and must be done for each single flight, which is beyond the scope of this paper.

The question now is how often do stable conditions occur, and are stable conditions coupled to certain wind directions? Fig. 8 displays a stability wind rose (32,736 10-min mean values for the relevant wind speed range of  $5 \text{ m s}^{-1}$  to  $25 \text{ m s}^{-1}$ ) from the offshore research platform FINO 1<sup>58</sup> located in the German Bight to the north of the island of Borkum (see Fig. 1) for the whole of the year 2005. While 20% of all values exceed a moderate stability of  $z/L = 0.2$ , 10% of all values still exceed a stability of  $z/L = 0.5$ .



Figure 8 also demonstrates a correlation between the wind direction and atmospheric stratification, which is typical for mid-latitudes on the northern hemisphere<sup>59</sup>, resulting from the alternating warm and cold sectors of the eastward moving cyclones at this latitude. Stable situations are most likely found for south-west wind directions, from which we can infer that this is the most likely direction producing long wakes in the North Sea. Further, the predominant wind directions in the North Sea are west and south-west wind directions as 42% of all values in Fig. 8 come from the 90 sector from south to west, meaning we expect stable situations from this predominant sector about 5% of the time. For wind farms located several tens of kilometres downwind of neighbouring wind farms along the main wind direction, the productivity of the downwind farms may be reduced during periods with stable stratification.

Our airborne observations provide the first *in situ* confirmation of the existence of far wakes extending at least 45 km downwind from wind farms, confirming the ability of numerical simulations and SAR satellite images in capturing the spatial structure of wind-farm wakes. Further analysis for different atmospheric conditions are foreseen to provide a clearer quantitative relationship between wind speed, turbulence intensity, atmospheric stability and wake length.

## References

- Colmenar-Santos, A., Perera-Perez, J. & Borge-Diez, D. *et al.* Offshore wind energy: A review of the current status, challenges and future development in Spain. *Renew. Sustain. Energy Rev.* **64**, 1–18 (2016).
- Neddernann, B., Realistic, T. N. Scenario for the Offshore Wind Power Development in Germany. *DEWI Mag.* **47** (2015).
- van Hoof, J. Unlocking Europe's offshore wind potential. *PwC Nederlande* **March 2017**, 40 (2017).
- GWEC. Global wind report, annual market update 2013. *Global Wind Energy Council* 80pp (2013).
- Dörenkämper, M., Optis, M., Monahan, A. & Steinfeld, G. On the offshore advection of boundary-layer structures and the influence on offshore wind conditions. *Boundary-Layer Meteorol.* **155**, 459–482 (2015).
- Nygaard, N. G. & Hansen, S. D. Wake effects between two neighbouring wind farms. *J. Physics: Conf. Ser.* **753**, 032020 (2016).
- Martinez-Tossas, L. A., Churchfield, M. J. & Meneveau, C. Large eddy simulation of wind turbine wakes: detailed comparisons of two codes focusing on effects of numerics and subgrid modeling. *J. Physics: Conf. Ser.* **625**, 012024 (2015).
- Jensen, L. E., Mørch, C., Sørensen, P. & Svendsen, K. Wake measurements from the Horns Rev wind farm European Wind Energy Conference. *European wind energy conference* **9** (2004).
- Frandsen, S. *et al.* The shadow effect of large wind farms: measurements, data analysis and modelling. *Report from Risø National Laboratory for Sustainable Energy–Risø-R1615 (EN)* (2007).
- Baidya Roy, S. & Traiteur, J. J. Impacts of wind farms on surface air temperatures. *Proc. Natl. Acad. Sci.* **107**, 17899–17904 (2010).
- Fiedler, B. & Bukovsky, M. The effect of a giant wind farm on precipitation in a regional climate model. *Environ. Res. Lett.* **6**, 045101 (2011).
- Zhou, L. *et al.* Impacts of wind farms on land surface temperature. *Nat. Clim. Chang.* **2**, 539–543 (2012).
- Fitch, A. C. *et al.* Local and mesoscale impacts of wind farms as parameterized in a mesoscale NWP model. *Mon. Weather. Rev.* **140**, 3017–3038 (2012).
- Barthelmie, R. *et al.* Offshore wind turbine wakes measured by SODAR. *J. Atmospheric Ocean. Technol.* **20**, 466–477 (2003).
- Fitch, A. C., Lundquist, J. K. & Olson, J. B. Mesoscale influences of wind farms throughout a diurnal cycle. *Mon. Weather. Rev.* **141**, 2173–2198 (2013).
- Prospathopoulos, J. & Chaviaropoulos, P. Numerical simulation of offshore wind farm clusters. In *European Wind Energy Association, Conference proceedings* (2013).
- Vautard, R. *et al.* Regional climate model simulations indicate limited climatic impacts by operational and planned European wind farms. *Nat. communications* **5** (2014).
- Wolken-Möhlmann, G., Gottschall, J. & Lange, B. First verification test and wake measurement results using a ship-lidar system. *Energy Procedia* **53**, 146–155 (2014).
- Jiménez, P. A., Navarro, J., Palomares, A. M. & Dudhia, J. Mesoscale modeling of offshore wind turbine wakes at the wind farm resolving scale: a composite-based analysis with the Weather Research and Forecasting model over Horns Rev. *Wind. Energy* **18**, 559–566 (2015).
- Hasager, C. B. *et al.* Using satellite SAR to characterize the wind flow around offshore wind farms. *Energies* **8**, 5413–5439 (2015).
- Lu, H. & Porté-Agel, F. On the impact of wind farms on a convective atmospheric boundary layer. *Boundary-Layer Meteorol.* **157**, 81–96 (2015).
- Volker, P., Badger, J., Hahmann, A. N. & Ott, S. The Explicit Wake Parametrisationv1. 0: a wind farm parametrisation in the mesoscale model WRF. *Geosci. Model. Dev.* **8**, 3715–3731 (2015).
- Troldborg, N. *et al.* Numerical simulations of wake interaction between two wind turbines at various inflow conditions. *Wind. Energy* **14**, 859–876 (2011).
- Emeis, S. A simple analytical wind park model considering atmospheric stability. *Wind. Energy* **13**, 459–469 (2010).
- Hansen, K. S., Barthelmie, R. J., Jensen, L. E. & Sommer, A. The impact of turbulence intensity and atmospheric stability on power deficits due to wind turbine wakes at Horns Rev wind farm. *Wind. Energy* **15**, 183–196 (2012).
- Wu, Y.-T. & Porté-Agel, F. Atmospheric turbulence effects on wind-turbine wakes: An LES study. *Energies* **5**, 5340–5362 (2012).
- Smedman, A.-S., Bergström, H. & Grisogono, B. Evolution of stable internal boundary layers over a cold sea. *J. Geophys. Res. Ocean.* **102**, 1091–1099 (1997).
- Emeis, S. *Wind energy meteorology: atmospheric physics for wind power generation*. Springer Science & Business Media (2012).
- Vermeer, L., Sørensen, J. N. & Crespo, A. Wind turbine wake aerodynamics. *Prog. aerospace sciences* **39**, 467–510 (2003).
- Fiedler, B. & Adams, A. A subgrid parameterization for wind turbines in weather prediction models with an application to wind resource limits. *Advances in Meteorology* **2014** (2014).
- Christiansen, M. B. & Hasager, C. B. Wake effects of large offshore wind farms identified from satellite SAR. *Remote. Sens. Environ.* **98**, 251–268 (2005).
- Li, X. & Lehner, S. Observation of TerraSAR-X for studies on offshore wind turbine wake in near and far fields. *IEEE J. Sel. Top. Appl. Earth Obs. Remote. Sens.* **6**, 1757–1768 (2013).
- Wildmann, N., Hofsaß, M., Weimer, F., Joos, A. & Bange, J. MASC—a small remotely piloted aircraft (RPA) for wind energy research. *Adv. Sci. Res.* **11**, 55–61 (2014).
- Jacobsen, S., Lehner, S., Hieronimus, J., Schneemann, J. & Kühn, M. Joint offshore wind field monitoring with spaceborne SAR and platform-based Doppler LIDAR measurements. *The Int. Arch. Photogramm. Remote. Sens. Spatial Inf. Sci.* **40**, 959 (2015).
- Emeis, S. *et al.* Exploring the wakes of large offshore wind farms. *J. Physics: Conf. Ser.* **753**, 092014 (2016).
- Skamarock, W. C. *et al.* A description of the advanced research WRF version 2. Tech. Rep., National Center For Atmospheric Research Boulder Co Mesoscale and Microscale Meteorology Div (2005).
- Hunter, J. D. Matplotlib: A 2D graphics environment. *Comput. In Sci. & Eng.* **9**, 90–95 (2007).

38. Bange, J. & Spieß, T. Airborne measurements in the early-morning shallow convective boundary layer. In *17th Symposium on Boundary Layers and Turbulence* 11 pp. (Amer. Meteorol. Soc., San Diego, CA, USA, 2006).
39. Bange, J., Zittel, P., Spieß, T., Uhlenbrock, J. & Beyrich, F. A new method for the determination of area-averaged turbulent surface fluxes from low-level flights using inverse models. *Bound.-Layer Meteorol.* **119**, 527–561 (2006).
40. Corsmeier, U., Hankers, R. & Wieser, A. Airborne turbulence measurements in the lower troposphere onboard the research aircraft Dornier 128-6, D-IBUF. *Meteorol. Zeitschrift* **10**, 315–329 (2001).
41. van den Kroonenberg, A. C., Martin, T., Buschmann, M., Bange, J. & Vörsmann, P. Measuring the wind vector using the autonomous Mini Aerial VehicleM<sup>2</sup>AV. *J. Atmos. Ocean. Technol.* **25**, 1969–1982 (2008).
42. Grossmann, S., Lohse, D., Lvov, V. & Procaccia, I. Finite size corrections to scaling in high Reynolds number turbulence. *Phys. review letters* **73**, 432 (1994).
43. Mann, J. & Lenschow, D. H. Errors in airborne flux measurements. *J. Geophys. Res. Atmospheres (1984–2012)* **99**, 14519–14526 (1994).
44. Lenschow, D., Mann, J. & Kristensen, L. How long is long enough when measuring fluxes and other turbulence statistics? *J. Atmospheric Ocean. Technol.* **11**, 661–673 (1994).
45. van den Kroonenberg, A., Martin, S., Beyrich, F. & Bange, J. Spatially-averaged temperature structure parameter over a heterogeneous surface measured by an unmanned aerial vehicle. *Boundary-Layer Meteorol.* **142**, 55–77 (2012).
46. Kaimal, J. C. & Finnigan, J. J. *Atmospheric boundary layer flows: their structure and measurement* (Oxford University Press, 1994).
47. Lenschow, D. H. & Stankov, B. B. Length scales in the convective boundary layer. *J. Atmos. Sci.* **43**, 1198–1209 (1986).
48. Chen, F. & Dudhia, J. Coupling an Advanced Land Surface-Hydrology Model with the Penn State-NCAR MM5 Modeling System. Part I: Model Implementation and Sensitivity. *MWR* **129**, 569–585 (2001).
49. Lim, K.-S. S. & Hong, S.-Y. Development of an Effective Double-Moment Cloud Microphysics Scheme with Prognostic Cloud Condensation Nuclei (CCN) for Weather and Climate Models. *Mon. Wea. Rev.* **138**, 1587–1612 (2010).
50. Iacono, M. J. *et al.* Radiative forcing by long-lived greenhouse gases: Calculations with the AER radiative transfer models. *J. Geophys. Res.* **113** (2008).
51. Nakanishi, M. & Niino, H. An Improved Mellor–Yamada Level-3 Model with Condensation Physics: Its Design and Verification. *Bound.-Layer Meteorol.* **112**, 1–31. <https://doi.org/10.1023/B:BOUN.0000020164.04146.98> (2004).
52. Fairall, C., Bradley, E. F., Hare, J., Grachev, A. & Edson, J. Bulk parameterization of air-sea fluxes: Updates and verification for the COARE algorithm. *J. climate* **16**, 571–591 (2003).
53. Kain, J. S. The Kain-Fritsch Convective Parameterization: An Update. *J. Atmos. Sci.* **43**, 170–181 (2004).
54. Chelton, D. B. & Wentz, F. J. Further development of an improved altimeter wind speed algorithm. *J. Geophys. Res. Ocean.* **91**, 14250–14260 (1986).
55. Lee, S., Churchfield, M., Moriarty, P., Jonkman, J. & Michalakes, J. Atmospheric and wake turbulence impacts on wind turbine fatigue loadings. In *50th AIAA Aerospace Sciences Meeting including the New Horizons Forum and Aerospace Exposition*, 540 (2012).
56. Barthelmie, R., Frandsen, S., Rethore, P. & Jensen, L. Analysis of atmospheric impacts on the development of wind turbine wakes at the Nysted wind farm. In *European Offshore Wind Conference*, vol. 6 (2007).
57. Türk, M. & Emeis, S. The dependence of offshore turbulence intensity on wind speed. *J. Wind. Eng. Ind. Aerodyn.* **98**, 466–471 (2010).
58. Türk, M., Grigutsch, K. & Emeis, S. The wind profile above the Sea-Investigations basing on four years of FINO 1 data. *DEWI Mag* **33**, 12–16 (2008).
59. Coelingh, J., Van Wijk, A. & Holtslag, A. Analysis of wind speed observations over the North Sea. *J. Wind. Eng. Ind. Aerodyn.* **61**, 51–69 (1996).

## Acknowledgements

The authors would like to thank the additional crew of the WIPAFF campaign, Per Schachtebeck, Thomas Feuerle, Helmut Schulz and Thomas Rausch, for their support. The project WIPAFF is funded by the German Federal Ministry for Economic Affairs and Energy (Bundesministerium für Wirtschaft und Energie) on the basis of a decision by the German Bundestag grant number: FKZ 0325783. TerraSAR-X data were kindly provided by the German Aerospace Center (DLR) in the framework of the WIPAFF\_TSX AO for scientific use. We thank the European Space Agency (ESA) for making SENTINEL-1 data available.

## Author Contributions

Andreas Platis contributed by writing the manuscript, analysing the data and conducting the measurement campaign. Astrid Lampert, Konrad Bärfuss, Rolf Hankers and Jens Bange contributed by organising and conducting the measurement campaign, data analysis and discussion. Simon Siedersleben performed the numerical simulations with the WRF model and contributed Figs 1, 6 and 7, Bughsin Djath and Johannes Schulz-Stellenfleth provided analysis of TerraSAR-X and SENTINEL-1 SAR data. Beatriz Canadillas contributed with FINO 1 data analysis and discussions. Richard Foreman took care of the overall structure of the paper and helped with the English language. Tom Neumann and Stefan Emeis had organised the WIPAFF project as a whole and contributed to the Introduction and Discussion, and Stefan Emeis made the analysis displayed in Fig. 8.

## Additional Information

**Competing Interests:** The authors declare that they have no competing interests.

**Publisher's note:** Springer Nature remains neutral with regard to jurisdictional claims in published maps and institutional affiliations.



**Open Access** This article is licensed under a Creative Commons Attribution 4.0 International License, which permits use, sharing, adaptation, distribution and reproduction in any medium or format, as long as you give appropriate credit to the original author(s) and the source, provide a link to the Creative Commons license, and indicate if changes were made. The images or other third party material in this article are included in the article's Creative Commons license, unless indicated otherwise in a credit line to the material. If material is not included in the article's Creative Commons license and your intended use is not permitted by statutory regulation or exceeds the permitted use, you will need to obtain permission directly from the copyright holder. To view a copy of this license, visit <http://creativecommons.org/licenses/by/4.0/>.

© The Author(s) 2018

# Long-range modifications of the wind field by offshore wind parks – results of the project WIPAFF

ANDREAS PLATIS<sup>1\*</sup>, JENS BANGE<sup>1</sup>, KONRAD BÄRFUSS<sup>3</sup>, BEATRIZ CAÑADILLAS<sup>4</sup>, MARIE HUNDHAUSEN<sup>1</sup>, BUGHSIN DJATH<sup>5</sup>, ASTRID LAMPERT<sup>3</sup>, JOHANNES SCHULZ-STELLENFLETH<sup>5</sup>, SIMON SIEDERSLEBEN<sup>2</sup>, THOMAS NEUMANN<sup>4</sup> and STEFAN EMEIS<sup>2</sup>

<sup>1</sup>University of Tuebingen, ZAG, Environmental Physics, Tübingen, Germany

<sup>2</sup>Karlsruhe Institute of Technology – Institute of Meteorology and Climate Research – Atmospheric Environmental Research, Garmisch-Partenkirchen, Germany

<sup>3</sup>Technische Universität Braunschweig, Institute of Flight Guidance, Braunschweig, Germany

<sup>4</sup>UL International GmbH, Oldenburg, Germany

<sup>5</sup>Helmholtz-Zentrum Geesthacht Zentrum für Material- und Küstenforschung GmbH, Geesthacht, Germany

(Manuscript received December 18, 2019; in revised form March 5, 2020; accepted March 6, 2020)

## Abstract

This publication synthesizes the results of the WIPAFF (WInd Park Far Fields) project. WIPAFF focused on the far field of large offshore wind park wakes (more than 5 km downstream of the wind parks) located in the German North Sea. The research project combined *in situ* aircraft and remote sensing measurements, satellite SAR data analysis and model simulations to enable a holistic coverage of the downstream wakes. The *in situ* measurements recorded on-board the research aircraft DO-128 and remote sensing by laser scanner and SAR prove that wakes of more than 50 kilometers exist under certain atmospheric conditions. Turbulence occurs at the lateral boundaries of the wakes, due to shear between the reduced wind speed inside the wake and the undisturbed flow. The results also reveal that the atmospheric stability plays a major role in the evolution of wakes and can increase the wake length significantly by a factor of three or more. On the basis of the observations existing mesoscale and industrial models were validated and updated. The airborne measurement data is available at PANGAEA/ESSD.

**Keywords:** WIPAFF, wind energy, offshore, wakes, marine boundary layer

## 1 Introduction

Wind park wakes have found increasing interest in recent years, when industry and authorities have started to plan wind parks closer together for good reasons (e.g. nature conservation, bundling of grid access, public acceptance), especially in offshore regions. As wind parks are built to extract kinetic energy from the atmosphere, downwind wake regions form behind turbines and wind parks, characterised by reduced mean wind speed and enhanced levels of turbulence (LISSAMAN, 1979). Both effects downgrade the conditions for downstream turbines and wind parks and are thus relevant for the expected power output from and the endurance of the installations. However, a deeper understanding of the physics of atmospheric flow in wind park wakes is needed to obtain better operational forecasts of wind energy production or scenario simulations (VEERS *et al.*, 2019; ROHRIG *et al.*, 2019).

We distinguish here between the near wake of wind parks (a few hundreds of metres to a few kilometres behind the parks) where the effects of single turbines are

clearly discernible, and the far wake (about five kilometres and more behind the parks) where the wakes of the single turbines have merged into a more or less uniform park wake (e.g. LI and LEHNER, 2013a). Most research on wakes so far has focused on near wakes behind single turbines and on wake interactions from a larger number of turbines within one and the same wind park (e.g., MARTÍNEZ-TOSSAS *et al.*, 2015; TRABUCCHI *et al.*, 2015). Only some experimental and recent numerical studies consider the wakes of entire wind parks and the impact of far wakes on neighbouring downwind wind parks on a larger spatial scale (e.g., CHAVIAROPOULOS, 2013; NYGAARD and HANSEN, 2016; SCHNEEMANN *et al.*, 2019).

The impact of far wakes from offshore wind parks on the regional climate has only been addressed in isolated studies (e.g., BOETTCHE *et al.*, 2015) with hardly any definite conclusions. Recent studies for onshore wind parks found similar effects of the impact PRYOR *et al.*, 2018. Wind park far wakes are of particular interest for offshore installations, because turbulence intensity – which is the main driver for wake dissipation – is much lower over the ocean than over land. Therefore, wakes behind offshore wind turbines and wind parks are expected to be much longer than behind onshore wind turbines and parks (see e.g., BARTHELMIE *et al.*, 2007; PORTÉ-AGEL *et al.*, 2020). Analytical studies (EMEIS,

\*Corresponding author: Andreas Platis, University of Tuebingen, ZAG, Environmental Physics, 72074 Tübingen, Germany, e-mail: andreas.platis@uni-tuebingen.de

2010; EMEIS, 2018; PORTÉ-AGEL et al., 2020) as well as numerical simulations (e.g. FITCH et al., 2012) have predicted these prolonged wind park wakes as well. Wake lengths up to about 100 km were found in these simulations (FITCH et al., 2012). Observational evidence of such long wakes has been available only indirectly so far from the evaluation of satellite data (CHRISTIANSEN and HASAGER, 2005).

*In situ* measurements of the far wakes were missing before the initiation of the research project WIPAFF (WInd PARK Far Fields), the main results of which are reported here. WIPAFF has been funded by the German Federal Ministry for Economic Affairs and Energy and ran from November 2015 to April 2019. The main goal of WIPAFF (EMEIS et al., 2016) was – for the first time – to perform a large number of *in situ* measurements from aircraft operations at hub height behind wind parks in the German Bight (North Sea), to evaluate further SAR images and to update and validate existing mesoscale and industrial models on the basis of the observations. First results from WIPAFF aircraft operations have been reported by PLATIS et al. (2018).

This publication is designed to give an integrative overview on the results of WIPAFF. Results from the evaluations of the different measurement and modelling efforts in the project (see EMEIS et al., 2016; DJATH et al., 2018; PLATIS et al., 2018; SIEDERSLEBEN et al., 2018b; SIEDERSLEBEN et al., 2018a; SIEDERSLEBEN et al., 2020; LAMPERT et al., 2020; PLATIS et al., in review; DJATH and SCHULZ-STELLENFLETH, 2020; CAÑADILLAS et al., 2020) are put into a common perspective. The airborne data set of the WIPAFF project is accessible to the community via the PANGAEA database (BÄRFUSS et al., 2019; LAMPERT et al., 2020). Section 2 gives the initial hypotheses of the project and Section 3 briefly reviews methods and their state of the art at the beginning of the project. The main results of WIPAFF are summarized in Section 4. Section 5 concludes the study and prepares an outlook to further necessary research.

## 2 The WIPAFF project's initial hypotheses

Wind turbines generate rotating wake vortices in which wind speed, turbulence intensity and turbulent fluxes are modified compared to the undisturbed flow. In a wind park with many wind turbines arranged in a tight grid, these single wakes are considered to superimpose each other (MARTÍNEZ-TOSSAS et al., 2015; TRABUCCHI et al., 2015). For the successful planning of further offshore parks, it is therefore crucial to identify the parameters that affect the wake development. There have been some model approaches of varying complexity that simulate these wake processes (FRANDSEN, 1992; EMEIS and FRANDSEN, 1993; VERMEER et al., 2003; EMEIS, 2010; FITCH et al., 2012; FIEDLER and ADAMS, 2014; VOLKER et al., 2015). A validation, however, of these models has not yet been available so far due to the lack of large offshore wind parks. With the installation of the first large

wind park cluster in the German Bight in the recent decade, this has become possible now. The WIPAFF project aimed to understand the wake development in the lee of wind parks, the corresponding decay dynamics and the size and impact of the wakes downstream of entire offshore wind parks by considering all influencing parameters. In the following, we address the four initial hypotheses of the WIPAFF project.

### 2.1 Hypothesis 1: Wake appearance is related to atmospheric stability

The most efficient mechanism for wake recovery is the vertical transfer of momentum from higher atmospheric layers downwards by atmospheric turbulence (EMEIS, 2010; ABKAR and PORTÉ-AGEL, 2015a; et al., 2015a; EMEIS, 2018). Because of the small surface friction and weak temperature gradients over the sea, much less mechanical turbulence is produced compared to onshore sites (SMEDMAN et al., 1997; et al., 2015b) and, hence, longer wakes are expected. For this reason, surface roughness and atmospheric stability are regarded to be the decisive parameters governing the generation of turbulence and thus the wake recovery (BARTHELMIE et al., 2009; BARTHELMIE and JENSEN, 2010; HANSEN et al., 2012; WU and PORTÉ-AGEL, 2012; CHAVIARPOULOS, 2013).

Wakes of several tens of kilometres were expected to be especially pronounced at offshore locations during stable conditions (HANSEN et al., 2012). This presumption of the existence of far wakes was supported by observational hints of long reaching wakes on satellite images of the sea surface from synthetic aperture radar (SAR, Figure 2). In stable stratifications, long wakes with a length exceeding 20 km have been assessed from synthetic aperture radar data (CHRISTIANSEN and HASAGER, 2005; LI and LEHNER, 2013a).

In addition to the fact that stability may play a very important role in the generation of far wakes, studies such as FRANDSEN et al. (2006); PORTÉ-AGEL et al. (2014); PORTÉ-AGEL et al. (2013); BARTHELMIE et al. (2009) showed that the wake intensity within the wind park depends crucially on the wind direction and the park layout. A larger initial wind speed deficit is observed when the wind direction is parallel to the turbine rows and the turbines are aligned. This larger initial wind speed deficit was expected to cause longer wakes according to EMEIS (2010).

### 2.2 Hypothesis 2: Wakes are associated with increased turbulence

Besides the reduction of the wind speed in the wake, turbulent effects, such as high turbulent kinetic energy (TKE) and increased momentum flux were expected. The degree of atmospheric turbulence impacts the efficiency and fatigue loading of a wind turbine (LEE et al., 2012). Two factors were considered responsible for the

production of turbulence. Firstly, the rotating wake vortices by the wind turbines and secondly, the production of turbulence as a result of the mixing of the wake and its decelerated wind field with the undisturbed flow. So far, mesoscale numerical models parameterize wind turbines as elevated moment sinks, and some of them as a source of TKE (BLAHAK et al., 2010; FITCH et al., 2012; ABKAR and PORTÉ-AGEL, 2015b; VOLKER et al., 2015). In large-eddy simulation (LES) studies and wind-tunnel experiments, these effects were determined at a distance of almost 20 times the wind turbine rotor diameter  $d$  ( $20d$ ) (WU and PORTÉ-AGEL, 2012). However, a validation with *in situ* measurement data has not yet been carried out, except in VOLKER et al. (2015) who used tower measurements collected during neutral conditions to evaluate the wind parks parameterizations of FITCH et al. (2012) and VOLKER et al. (2015).

### 2.3 Hypothesis 3: Wakes have the potential to impact other wind parks downstream

For an optimal use of the marine areas, wind parks are constructed at favourable locations and in clusters in order to minimize the expense of grid connections and due to other constraints like military zones, pipelines, and nature preserves. However, the close proximity can undermine power production in other wind parks downstream, due to wakes from upwind wind parks, causing an economic loss (KAFFINE and WORLEY, 2010; NYGAARD, 2014; NYGAARD and HANSEN, 2016; BODINI et al., 2017; LUNDQUIST et al., 2019). Simple analytical models and first studies confirmed that especially during thermally stable stratification wakes have an impact on downwind wind parks reducing their efficiency.

### 2.4 Hypothesis 4: Wakes impact local climate

Large wind farm impose an obstacle in a flat environment, which decelerate the flow locally associated with a flow-around and overflow effects. As a result, the turbulent fluxes and heat in the atmospheric boundary layer (ABL) may change.

It was already known that onshore wind parks can impact the near surface temperature, and the turbulent fluxes of sensible heat, CO<sub>2</sub>, and water vapour (latent heat) (e.g. ROY and TRAITEUR, 2010; ZHOU et al., 2012; RAJEWSKI et al., 2013; RAJEWSKI et al., 2014; ARMSTRONG et al., 2016). For example, ZHOU et al. (2012) observed a warming of 0.5 K in the vicinity of onshore wind parks, especially during nocturnal stable conditions. But only a few studies have investigated the potential effect of offshore wind parks on the marine boundary layer (MBL). These studies were motivated by visible cloud effects as they were seen in photos taken at a wind park at the coast of Denmark (EMEIS, 2010; HASAGER et al., 2013; HASAGER et al., 2017), indicating fog formation and dispersion due to enhanced mixing and adiabatic cooling downwind of wind parks. Associated with

enhanced mixing, FOREMAN et al. (2017) reported a decreased sensible heat flux downwind of a small offshore wind park during stable conditions in the German Bight by using eddy-covariance measurements of heat and humidity fluxes at the research platforms FINO1 mast.

Also numerical simulations have indicated a change in air temperature and humidity in the downwind direction of offshore wind parks. VAUTARD et al. (2014) identified increased temperatures in the area of offshore wind parks in their simulations, whereby WANG and PRINN (2011) reported a potential cooling effect in the vicinity of offshore wind parks due to an increased latent heat flux. These thermal effects were not investigated by field measurements, so far. Therefore, in the framework of the WIPAFF project, their spatial extent was investigated together with the possibility that larger wind parks may have an influence on the local climate.

## 3 Methods used in the WIPAFF project

### 3.1 Airborne Data

Airborne *in situ* data were collected with the research aircraft Dornier DO-128 operated by the Technische Universität Braunschweig, Germany. 41 measurement flights over the German Bight during the WIPAFF project during 2016 and 2017 delivered (in general at a sampling frequency of 100 Hz) 3D wind vector, temperature, humidity, and sea surface-temperature. A detailed explanation of the used measurement instruments and the aircraft can be found in CORSMIEIER et al. (2001); PLATIS et al. (2018); LAMPERT et al. (2020). The starting points of the flights were Wilhelmshaven, Borkum or Husum airport, respectively. A typical flight pattern to capture the wakes is displayed in Figure 1 is the so-called "meander pattern", with several flight legs at hub height (at about 100 m above sea level) positioned downstream of the wind-park cluster. The data is freely available from BÄRFUSS et al. (2019) and further explained in LAMPERT et al. (2020).

Besides the meteorological *in situ* data, a downward-looking scanning lidar system measuring the distance aboard the research aircraft recorded the sea-surface state for deriving the shape and distribution of the sea waves, and for characterizing the far-field wakes.

### 3.2 Satellite information for retrieving surface properties

Active microwave radar sensors such as Synthetic Aperture Radar (SAR) are powerful instruments for sunlight and weather independent measurements of the ocean surface roughness at high spatial resolution. The capability of SAR to provide information on offshore windpark wakes has been amply demonstrated (CHRISTIANSEN and HASAGER, 2005; LI and LEHNER, 2013a; DJATH et al., 2018). Far field wake effects of more than 10 km downstream of offshore wind parks have for the

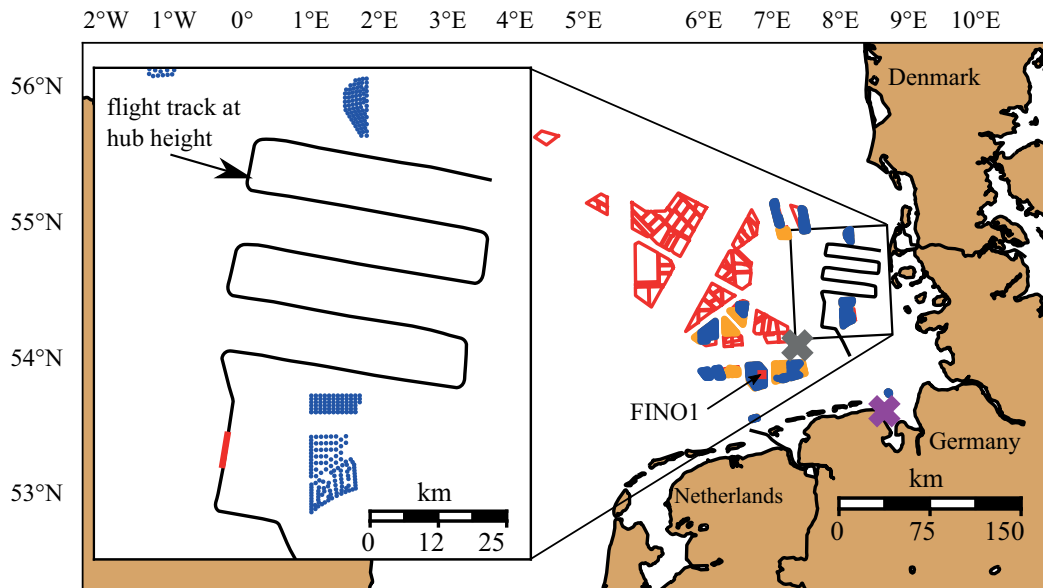


**Figure 1:** Distribution of offshore wind parks in the German Bight as of December 2017. Blue regions are parks currently in operation, red indicate parks still in the approval process. Orange regions are those wind parks that are under construction. The red line within the close-up indicates the area where typically the vertical profiles were flown to capture the atmospheric stratification in close vicinity to the wind farm. The map is adapted from data of the German Federal Maritime and Hydrographic Agency (BSH) and adapted from [PLATIS et al., 2018](#). The magenta and grey colored crosses show locations of climb flights as indicated in Figure 16.

first time become evident based on the analysis of SAR images ([CHRISTIANSEN and HASAGER, 2005](#); [LIN et al., 2008](#); [LI and LEHNER, 2013b](#)). In the WIPAFF project, SAR revealed changes of surface properties downwind of wind parks, expanding the airborne observations to a scale beyond 100 km.

SAR measures near surface wind fields in an indirect way through the small scale roughness of the sea surface. The wind influences the sea surface by generating cm-scale roughness, which is captured by active microwave sensors due to the Bragg-scattering principle. Low image intensities thus indicate areas of reduced wind speed.

Sentinel-1A (launched in 2014) and Sentinel-1B (launched in 2016) are twin satellites that provide SAR data in the German Bight on a regular basis. They were launched into a sun-synchronous orbit and operate at C-band (5.405 GHz) at vertical receive and transmit polarization (VV). Each satellite has an exact repeat cycle of 12 days for the same imaging geometry (i.e., incidence angles and area covered are identical), but can provide data for a particular spot at one or two day intervals, if different imaging geometries are acceptable. Thus, the combination of both satellites provide an image every 6 days with identical geometry. The estimation of wind speeds from SAR requires the radiometric calibration of the SAR raw data and the inversion of a so called geophysical model function (GMF) ([HERSBACH et al., 2007](#); [VERHOEF et al., 2008](#)). Wind direction information can be retrieved either from SAR image structures or alternatively external sources (e.g., atmospheric models) are used.

Wind speed deficits were estimated from SAR using a technique proposed in [CHRISTIANSEN and HASAGER \(2005\)](#) and a new filter approach described in [DJATH and SCHULZ-STELLENFLETH \(2020\)](#). The overall challenge in this application is the estimation of the undisturbed background wind speed, which is not available at the exact location of the wake. The use of wind speeds in neighbouring areas as a proxy leads to certain errors, which depend on spectral properties of the background wind field and which are discussed in more detail in [DJATH and SCHULZ-STELLENFLETH \(2020\)](#).

A spectral analysis of wind fields in the German Bight was conducted as follows. SAR scenes from both satellites were collected for the period September 2016 to December 2017. The occurrence of wakes around the wind park Amrumbank West was analysed (Figure 1). Only the scenes that included the entire Amrumbank West were considered and overall, 177 scenes were collected. Wave-number spectra were then computed from the SAR derived 10 m-wind speed maps. Wind field data were classified considering the stability conditions based on the thermal stratification from FINO1 data. Wind fields associated with stable conditions (STA) and unstable conditions (NOSTA) were considered. A 2D spectral analysis was applied to a square box of 320×320 grid points (with a grid spacing of 300 m, i.e. spatial resolution) aside the wind turbines (see blue box in Figure 2). Using this area, a wavelength range between 0.6 km and 100 km is covered. A 2D Fast Fourier Transform (FFT) was applied to the SAR derived wind fields after the mean was removed. The resulting 2D wavenumber spectrum was scaled in

such a way, that integration of the entire spectral domain equalled the total variance of the wind field. As the wavenumber and directional dependency were also analysed, the spectra were interpolated from the original 2D Cartesian grid to a polar grid. The 1D spectrum was then computed by integrating over all directions.

Besides the observational data, different (numerical) model types were used to investigate the far field of offshore wind parks.

### 3.3 Mesoscale model and wind-park parameterizations (WPPs)

All mesoscale numerical simulations were performed with the Weather Research and Forecasting Model WRF (version 3.8.1). We used the wind park parameterization of FITCH *et al.* (2012) to simulate the wakes of offshore wind parks in the German Bight. Wind park parameterizations (WPPs) allow one to simulate the impact of several wind parks on the marine boundary layer due their low computational costs. Nowadays, offshore wind parks cover an area on the order of 100 km<sup>2</sup> and the corresponding wakes exceed 50 km downwind (Figure 2). Consequently, large offshore wind parks affect a large area, hence, high resolution large-eddy simulations covering the wake area and the corresponding wind park are computationally too expensive to estimate the economic potential loss of planned offshore wind parks or the regional climate impact of wind parks. For such purposes, WPPs are a suitable tool.

The wind park parameterization of FITCH *et al.* (2012) extracts momentum from the mean flow at the rotor area and adds TKE at rotor height. In contrast, others (e.g. JACOBSON and ARCHER, 2012; e.g. VOLKER *et al.*, 2015) do not add any TKE as they assume that the TKE develops due the resolved shear. However, both approaches simulate wakes of offshore wind parks with a length exceeding 50 km during neutral conditions (VOLKER *et al.*, 2015).

Evaluation studies testing the performance of WPPs for offshore wind parks during stable conditions are rare. HASAGER *et al.* (2015) compared SAR retrieved wind speed to mesoscale simulations. VOLKER *et al.* (2015) tested their WPP and that of FITCH *et al.* (2012) with real case data using idealized simulations. However, all these evaluation studies were either based on remote sensing data allowing only an evaluation of the wind speed 10 m above mean sea level (msl) or on idealized simulations omitting moisture effects and assuming a stationary inflow. Therefore, studies investigating the performance of WPPs for real case simulations are necessary.

### 3.4 Analytical model

Analytical wind park models for the assessment of wakes can be constructed in two ways. These models are either bottom-up models which are based on overlays of several single-turbine wakes (the description of which

dates back to JENSEN, 1983) or they are top-down models which consider wind parks as a whole, e.g., as an additional surface roughness, as an additional momentum sink or as a gravity wave generator in association with a temperature inversion aloft at the top of the boundary layer (for the latter idea see SMITH, 2010), which modifies the mean flow above wind parks (NEWMAN, 1977; BOSSANYI *et al.*, 1980; FRANDBSEN, 1992). Such models have analytical solutions which make them attractive, although they necessarily contain considerable simplifications. Nevertheless, they can be used for first-order approximations in wind park design. Furthermore, a significant advantage of top-down models that they implicitly include the ‘deep array’ effects (BARTHELMIE and JENSEN, 2010). Wind turbines in a large array influence the flow in the atmosphere above the wind farm (CHAMORRO and PORTE-AGEL, 2011). It has been proposed that this prevents the entrainment of momentum from the air above the wind farm, restricting the wake recovery (NYGAARD, 2014).

The analytical wind park model of EMEIS (2010) is an extension of earlier ideas documented in FRANDBSEN (1992) and EMEIS and FRANDBSEN (1993). An updated version which additionally includes the turbulence generated by the turbines in the wind park itself is documented with all equations in Chapter 6 of EMEIS (2018). The basic idea of this model is that the overall momentum consumption of the turbines in very large wind parks, which is proportional to the drag coefficient of the turbines and the wind speed at hub height, can only be compensated for by a turbulent momentum flux from above. This leads to an analytical equation for the reduced horizontal wind speed at hub height in the interior of large wind parks. In the wake behind such large wind parks the wind speed at hub height can only recover again due to a turbulent momentum flux from above. This leads to an exponential function for the wind speed recovery at hub height in the wake. The length of the wake is arbitrarily defined as the distance behind the wind park where the wind speed has recovered to more than 95 % of the undisturbed value ahead of the wind park. We note that the decay coefficient used here is not the wake decay coefficient (WDC) used in the quadratic decay function of JENSEN (1983). In this analytical model the wind speed reduction at hub height within a large wind park is given as a function of the areal density of turbines in the park, (sea) surface roughness, turbine-induced turbulence and the thermal stability of the atmospheric boundary layer. The wake length in the analytical model depends on the reduced wind speed right after the wind park and the latter three parameters mentioned before. The park layout, i.e., the spatial arrangement of turbines within a wind park, is not covered by this analytical model.

### 3.5 Engineering models

Engineering models are widely used in the wind energy industry due to their low computational costs and ease

of use to account for wind park wakes. Direct wakes of each individual turbine are simulated with the ‘modified PARK’ model (KATIC et al., 1987). Alternatively, the ‘Eddy Viscosity’ model AINSLIE (1988) could be used. Experience shows that the differences between the two models are particularly relevant in the first kilometers behind the wake-generating turbine. Since in the WIPAFF context, however, the effects beyond 10 km on the lee side of the wind park are particularly relevant, the ‘modified PARK’ model is used here due to the significantly shorter computing time.

In large (offshore) wind parks, the turbines cannot be regarded as independent of the free wind field. Rather, they extract momentum from the wind and therefore act like an area with increased roughness. This results in the formation of an internal boundary layer (IBL) with reduced wind speed behind each turbine. The exact shape of the IBL and the resulting wind speed reduction depends on the orientation of the wind park layout relative to the wind direction (DNV-GL, 2013a).

Both (the ‘modified PARK’ model combined with an IBL) together allow a reasonable simulation of the wake in offshore wind parks and wind park clusters and are often used in this combination for the determination of wind park yields. Importantly, as the individual turbine wake and IBL models have been developed assuming neutral conditions, stratification needs to be explicitly accounted for by tuning the parameters of these models to match the observations (PEÑA and RATHMANN, 2014) and to get an accurate estimation of energy production.

## 4 Results

In the following the four hypotheses described in Section 2 are tested.

### 4.1 On hypothesis 1: Wake Appearance

#### 4.1.1 Appearance of wakes from SAR and airborne data

28 out of the total 41 flights during the WIPAFF project included a flight strategy which allowed for the determination of wakes behind wind parks. For 12 out of the 28 flights, the wake length, defined as the distance to 95 % recovery of the wind field, exceeded the length of the flight meander pattern and for two flights the wake length was observed to be shorter than the downwind distance of the first measured leg. The observed wakes within the WIPAFF campaigns range from nearly 0 km in unstable atmospheric conditions to over 65 km in atmospheric stable conditions (see for further results and discussion Section 4.1.2). The flow inside the wakes was reduced up to 43 % compared to the undisturbed flow, two examples are shown in Figure 4 and 10a).

In addition to the airborne observations, wakes were identified by the analysed surface roughness and backscatter signal (Normalized Radar Cross Section –

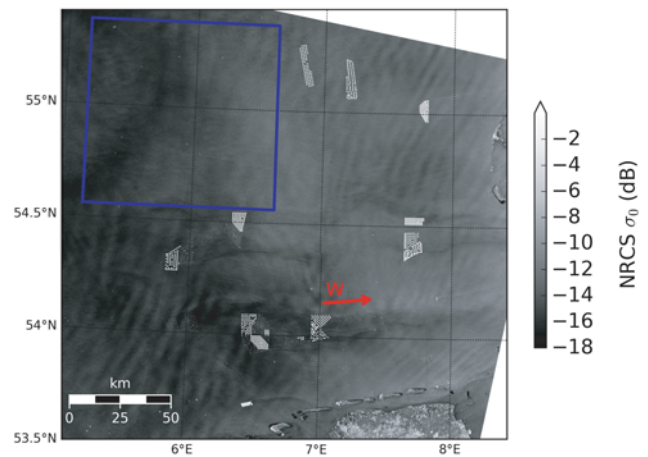


**Figure 2:** NRCS from Sentinel-1A acquired on 27 May 2019 at 05:49 UTC (Copernicus Sentinel data [2019]). Dark streaks in East-West direction behind the wind parks represent atmospheric wakes. Strong atmospheric related NRCS modulation are also found in North-South direction. The blue box was used for the estimation of 2D wavenumber wind spectra. The red arrow indicates the wind direction.

NRCS) from SAR Sentinel – 1A and 1B observations, e.g. Figure 2. The images exhibit darker streaks downwind of wind parks and brighter features at the edges of the wakes, which indicate that surface roughness is reduced downstream of wind parks, and increased along the edges of the wind parks. An example of recent Sentinel-1A SAR image on 27 May 2019 in Figure 2 shows the wakes through the east-west oriented dark streaks behind the wind parks and are in line with the wind direction coming from West. The wind direction is given by the German weather service (DWD) that provides hourly weather data. The wake behind individual wind parks are longer than 30 km. Statistical analysis from SAR data and atmospheric stability by DJATH et al., 2018 showed wakes longer than 50 km and also revealed that the wakes are longer for stable conditions. Overall, from the total 177 collected scenes between 2016 and 2017, 38 % of them show wakes downstream of offshore wind parks. The case with missing wakes on SAR could be related to either strong atmospheric instability or the fact that the wind farms are not in operation.

#### 4.1.2 Longer wakes during stable stratification

Experimental observations by SAR and aircraft indicated that the wake length depends on the stability of the surrounding atmospheric flow. Therefore, a detailed correlation analysis was performed in order to quantify the effect of different stability definitions on the wake length.

A layer is considered as stable, when vertical motion is suppressed, and as unstable or convective, when vertical motion is enhanced (STULL, 2012). By theory and as outlined in EMEIS et al. (2016), it is typical over the ocean for the northern hemisphere in the temperate west-wind belts that warm sector winds most fre-



quently come from the south-west and thus are followed by rather stable conditions, whereas cold-sector winds come from the north-west and predominantly bring convective conditions. For the German Bight, long term studies conducted during recent years support these assumptions (WESTERHELLWEG et al., 2010; SATHE, 2010; MUÑOZ-ESPARZA et al., 2012; EMEIS et al., 2016).

A common stability parameter is the static stability or lapse rate  $\gamma$ , which takes solely buoyancy into account. The lapse rate is defined by the derivation of the virtual potential temperature  $\theta_v$  with respect to the vertical coordinate  $z$ , and can be approximated by the temperature difference  $\Delta\theta_v$  between two levels separated by height difference  $\Delta z$ :

$$\gamma = \frac{d\theta_v}{dz} \approx \frac{\Delta\theta_v}{\Delta z} \quad (4.1)$$

Thus,  $\gamma$  is negative during convective conditions and positive for stable cases.

Common parameters that express dynamic stability, considering both buoyancy and shear, are the Obukhov length and the bulk Richardson number (STULL, 2012; MUÑOZ-ESPARZA et al., 2012). Moreover, there are measures of the magnitude of turbulence, not considering any thermal stratification at all. Most common in ABL science is the turbulence kinetic energy (TKE) per volume and unit mass

$$k = \frac{1}{2} \cdot (\overline{u'^2} + \overline{v'^2} + \overline{w'^2}) \quad (4.2)$$

taking the turbulent part of the wind speed components into account.

We used SAR and flight data in the WIPAFF project to investigate the correlation between stability and wake length.

In a first step SAR scenes taken over the offshore windpark Alpha Ventus were analysed and wake lengths were estimated using the technique described in CHRISTIANSEN and HASAGER (2005). This technique consists of estimating the velocity deficit from two parallel transects defined such that one transect encloses the wake area and the second transect is defined outside the wake, which is characterised as freestream conditions. The length at which the wind speed inside the wake has recovered to the freestream characterizes the maximum length of the wake. The scenes were collocated with estimates of the vertical gradient of potential temperature obtained from the nearby FINO-1 platform. The vertical gradient is based on the measurement of the hourly sea surface temperature at FINO1 and the air temperature at 50 m height. The resulting scatter plot is shown in Figure 3. One has to emphasize that this analysis only includes measurements during the early period (2011–2015), where the Alpha Ventus windpark was not affected by neighbouring wind farms, like it is today. One can clearly see a relationship between increasing atmospheric stabilities and growing lengths of the offshore wind farm wake. More details are given in DJATH et al. (2018).

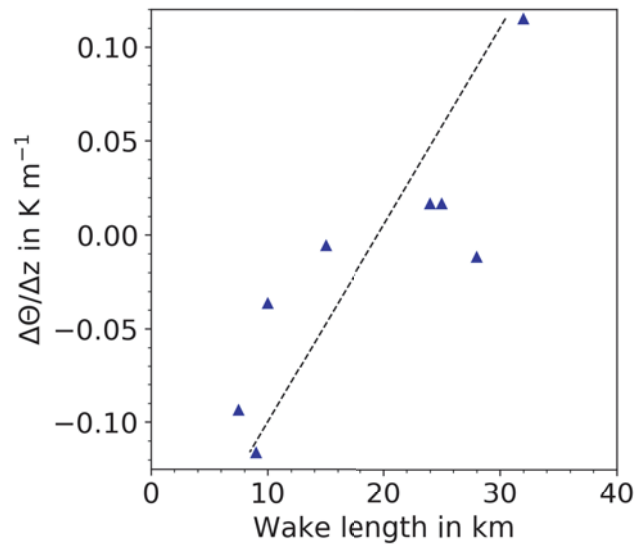


**Figure 3:** Scatterplot of SAR derived wake lengths versus atmospheric lapse rate  $\gamma = \frac{\Delta\theta_v}{\Delta z}$  derived from FINO-1 data (adapted from DJATH et al. (2018)).

The second data source for the determination of the stability were the airborne measurements. We used the vertical profiles obtained during the WIPAFF measurement flights close to the wind parks as marked in Figure 1 for the stability estimation. Further, to examine the relationship between wake expansion and stability, the wake length obtained from flight data (e.g Figure 4) was compared to the stability parameters such as  $L$ ,  $Ri_B$ , and  $\gamma$ . However, a general statement is difficult. Most promising results were achieved using  $\gamma$  (Figure 5a), using a height interval  $\Delta z$  from the uppermost position of the wind turbine blade tip (at 150 m agl for the Amrumbank West wind park AW, for instance) to the lowest position (at 30 m agl for AW). Thus, the height interval covers the entire rotor area, as this was assumed to be the most representative height interval with respect to the wake origin.

Looking at the distinct wind park clusters (Figure 5), the correlation between wake length and stronger stability, as observed for the wind parks GO (Godewind) and AW, can be approximated by two different exponential functions. This is an indication that there are more parameters that govern the wake length, in addition to stability – possibly also the wind-park architecture as considered in the analytical model. Moreover, strong stability coincides with the absence of short wakes. In addition, there is a correlation between higher wind speed deficit with more stable atmospheric conditions (not shown), while small wind deficits occur during more convective conditions.

Using the airborne data set of the WIPAFF project, a distinct correlation between the wake length and the other stability parameters  $L$  and  $Ri_B$  (not shown) was not apparent. Summing up, the correlation analysis for wake length and stability exhibits large uncertainty and data scatter. A major problem is the exact determination

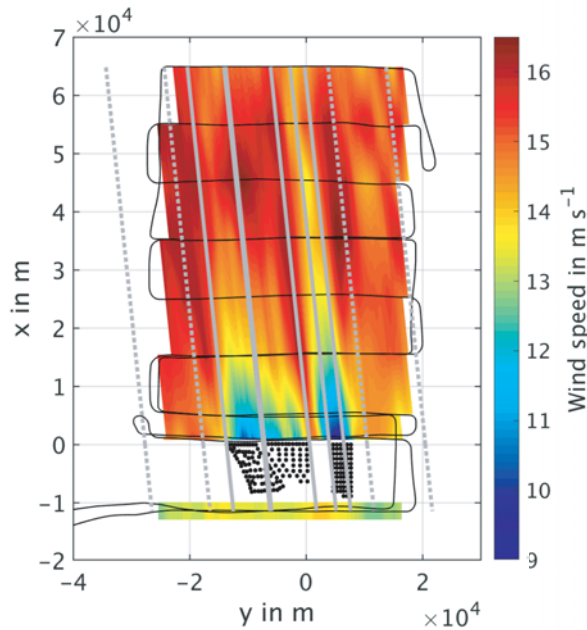


**Figure 4:** Contour plot of the interpolated wind field, measured during Flight 31 on 08 August, 2017, including the indication of the undisturbed wind field (grey dashed lines) and the wake boundaries (grey solid lines). The black line refers to the flight track (so-called “meander pattern”), black dots indicate the wind turbines of the wind park cluster Amrumbank West, Nordsee Ost and Meerwind Süd/Ost. The mean wind direction is from the east. The top of the map is oriented towards the west. Adapted from [PLATIS et al. \(in review\)](#).

of stability. A variation of e.g. the height interval for the lapse rate  $\gamma$  or the occurrence of an inversion below the hub height (cf. Section 4.1.3) changes the results significantly. A more detailed analysis will be shown in a following study.

#### 4.1.3 Vertical Structure of wakes

The vertical structure of the atmospheric boundary layer approaching the wind park has a decisive impact on the wake forming. Especially the occurrence of temperature inversions is important. The aircraft data documented several cases where the inversion was either below, at the rotor area of the turbines, or above ([SIEDERSLEBEN et al., 2018b](#)). In each of these cases a different behaviour of the wake could be observed. The main challenge with inversions near to or at hub height is that the thermal stratification of the atmospheric boundary layer and the respective level of turbulence are different below and above the inversion. This makes it very difficult to assign a specific thermal stratification to an observed wake development. An inversion below the rotor area decouples the wake development from the state of the sea surface. An inversion above the rotor area prevents the wake from spreading into higher parts of the boundary layer. Inversions are quite common above the North Sea, especially if the flow comes from land upstream. Internal boundaries form when the flow transits across the shoreline from land to water (see, e.g., [SMEDMAN et al., 1997](#)).

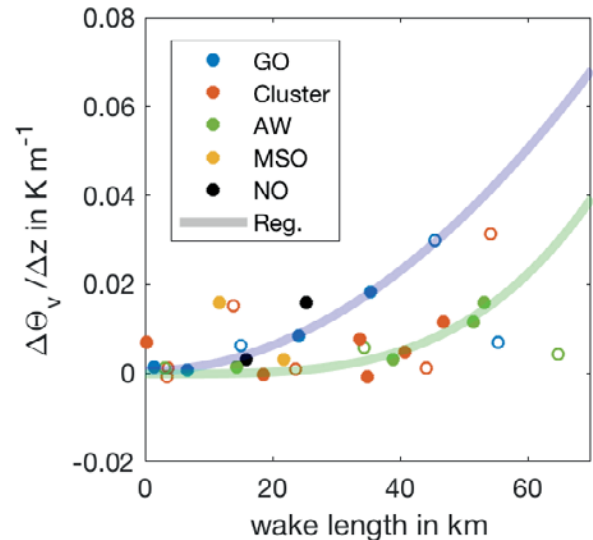


**Figure 5:** Scatter plots of the wake length versus lapse rate  $\gamma = \frac{\Delta\Theta_v}{\Delta z}$  obtained from the flight measurement. The according wind park is colour coded. Wakes were measured downstream of the wind parks Amrumbank West (AW), Nordsee Ost (NO), Meerwind Süd/Ost (MSO), Godewind (GO). Cluster implies that only one single wake was identified downstream of the wind park cluster consisting of the wind parks AW, NO and MSO. The regression lines (Reg.) are color coded with respect to the color of the respective wind farm cluster. The regression line is plotted is blue for the wind farm GO green and for the AW. In the case the wake length exceeds the coverage of the flown meander pattern (cf. Figure 4), the non-filled marker is used for the minimum measured wake length.

Given the distance of the North Sea wind parks from the coast the top of this internal boundary layer is very often found in the height range of the rotor area ([LAMPERT et al., 2020](#)). There are not only newly-formed inversions at the top of internal boundary layers but also inversions advected from the land upstream where they had formed due to radiative cooling in the nocturnal boundary layer. If these cold near-surface layers are advected over warmer sea water, the layer underneath the inversion can be turned into a neutral or even slightly unstable layer while the stratification above the inversion remains more or less unchanged. The propagation conditions for wind park wakes may be further complicated by jet-like wind maxima at the top or just above the internal boundary layer (see, e.g. [SMEDMAN et al., 1996](#)). The variety of different vertical profiles of potential temperature and wind speed from 26 aircraft operations in WIPAFF is documented in [SIEDERSLEBEN et al. \(2018b\)](#); [LAMPERT et al. \(2020\)](#) while a case study from one flight is presented in [SIEDERSLEBEN et al. \(2018a\)](#). It is not only the propagation of the wake which is determined by the vertical structure of the air approaching the wind parks but the vertical structure also determines whether the air at hub height behind the wind park is warmer or cooler than before. Figure 6 shows a schematic of this dependence. An inversion in the upper part or just above the rotor area associated with turbulent vertical

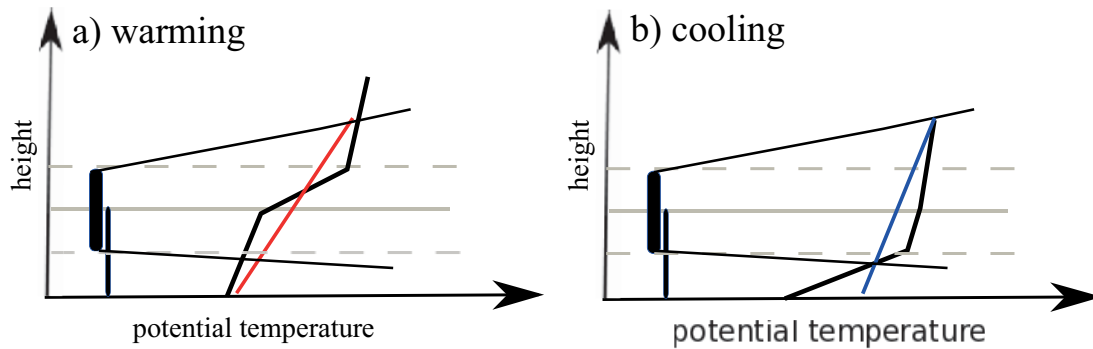


**Figure 6:** Schematic of stability-dependent temperature change at hub height in wind park wakes (left: warming, right: cooling). Bold vertical line: rotor disk, cone-like structure: wake, black vertical profile: initial temperature profile, red and blue curves: temperature profiles modified by the wake. (From [SIEDERSLEBEN et al., 2018b](#))

mixing within the wake results in a warming of the air at that height. In contrast, an inversion in the lower part or just below the rotor area results in a cooling of the air at that height. In a constantly stable boundary layer without inversions turbulent mixing within the wake will lead to warming below hub height and cooling above hub height. This warming below hub height is similar to satellite observations of nocturnal surface warming behind onshore wind turbines (see, e.g. [XIA et al., 2017](#) and references therein). Nevertheless, the observed temperature changes are merely a vertical re-distribution of heat by the additional turbulence in the wake.

#### 4.1.4 Wakes covered by mesoscale and industrial models

The numerous observations of wakes allowed the evaluation of wake simulations. Within the WIPAFF project, two kind of simulations were evaluated. First of all, mesoscale simulations using WRF and the wind park parameterization of [FITCH et al. \(2012\)](#) were compared against the airborne observations. Secondly, we tested the ability of commonly used industrial models to capture wakes of large offshore wind parks during stable conditions. In this overview paper we focus on observations covering simulations of a wake event observed on 10 September 2016 during atmospheric stable conditions and moderate wind speed of around  $8.5 \text{ m s}^{-1}$ .

The WRF simulations captured the horizontal dimensions of the wake but overestimated the vertical extent ([SIEDERSLEBEN et al., 2018a](#)). The wake observed on 10 September 2016 extended more than 45 km downwind of the wind park Amrumbank West, agreeing with the simulations [PLATIS et al., 2018](#). However, the vertical extent of the wake was overestimated in the simulations. For example, a wind deficit in the order of 5%–10% was observed 5 km downwind of the last turbines of Amrumbank West at 200 m above MSL. In contrast, a wind deficit on the order of 20% and 15% was simulated (not shown).

The simulated wind speed upwind of the wind parks was  $1.5 \text{ m s}^{-1}$ – $2 \text{ m s}^{-1}$  too low [SIEDERSLEBEN et al., 2018a](#). Consequently, the wind speed within the wake of

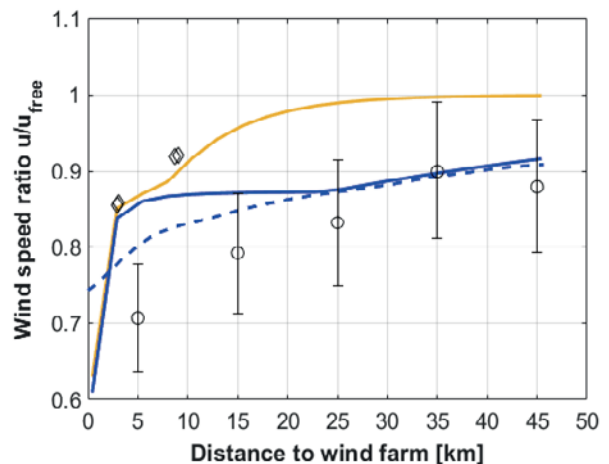


**Figure 7:** Wind speed reduction relative to free wind speed (10 m/s) in the wake of the wind park cluster Amrumbank/North Sea Ost/Meerwind on 10 September 2016. Shown are the flight data (black dots with error bars), the WRF simulation (blue dashed line), as well as two wake simulated with WindFarmer: default settings (orange solid line) and adjusted settings (blue solid line) the diamonds correspond to the original measurements used to calibrate the default WindFarmer set-up [DNV-GL, 2013b](#).

the simulations was underestimated as well (Figure 7). Aircraft vertical profiles of the atmosphere obtained by climb flights revealed that the simulated stratification of the atmosphere was too unstable at the transition area from land to open ocean. Therefore, we suggest that the overestimated vertical extent of the simulated wake is rooted in a wrongly simulated stratification of the atmosphere.

To compare the WRF simulation and the industrial model (WindFarmer Version 5.2.11 was used within the project) with the flight measurements, a methodology similar to that described in [CAÑADILLAS et al. \(2020\)](#) was used to extract the minimum value of the wind speed along the wake centerline. Layouts and turbine types were chosen identical to those used in the WRF simulation. In WindFarmer, the model options “modified PARK” and “IBL” (internal boundary layer) were selected. This combination is based on the best repre-

sensation of the park effects in offshore wind parks and clusters to determine park yields. While the wind speed deficit in the modified PARK and Eddy Viscosity models decreases with increasing turbine spacing, this is not the case in the IBL implementation, which is of course unphysical. The recovery of the wind velocity deficit from the IBL model was therefore realized by an additional function (so-called “wake recovery function”). Downstream of the wind farm, the wind speed recovery is modelled explicitly as a power function [DNV-GL, 2013a](#)

$$U_R(x) = 1 - \left(1 - \frac{U}{U_\infty}\right) 0.5^{\left(\frac{x-x_{\text{start}}}{x_{50\%}}\right)}, \quad (4.3)$$

where  $x_{\text{start}}$  is the downstream distance specifying the start of the power function, and  $x_{50\%}$  is the location where the wind speed recovery  $U_R$  has recovered to half its initial value.

The standard parameterization of the wake recovery function starts at  $x_{\text{start}} = 60D$  ( $D$  is the rotor diameter; here  $D = 120$  m) behind the turbine and after another  $x_{50\%} = 40D$  has reduced half of the wind speed deficit. These values were derived by WindFarmer from mast measurements at the lee side of the Danish wind parks “Horns Rev” and “Nysted”. With this parameterization the wake curve (orange solid line) is obtained by [DNV-GL, 2013b](#), which is shown in Figure 7. Apparently the wind speed recovers much faster with this parameterization than measured by the research aircraft on 10 September 2016.

A more detailed analysis shows that the measuring masts at “Horns Rev” and “Nysted” are each installed east of the parks, so that the park wake there can only be determined with westerly winds. It is known from stability studies conducted at the offshore mast FINO1 that neutral to stable stability conditions dominate in westerly winds ([EMEIS et al., 2016](#)). Probably the parameters for the wake recovery function in WindFarmer were determined on the basis of neutral to unstable stratifications. By contrast, neutral to slightly stable conditions prevailed on 10 September 2016.

It is known from the observations in WIPAFF ([CAÑADILLAS et al., 2020](#)) and from the analytical wake model of Section 4.1.5, that considerably larger wake lengths result with stable atmospheric stratification compared to neutral and unstable stratification. This supports the assumption that the wake length differences between the measurements and the standard parameterization in WindFarmer are mainly due to an incorrect accounting of stability effects in the default set-up of Wind Farmer. However, the measurements can be well reproduced by a different parameterization (start of wake recovery at  $200D$ , 50% recovery after another  $200D$ ) for distances beyond 22 km from the wind park cluster (Figure 7). For further discussions, please refer to [CAÑADILLAS et al. \(2020\)](#).

#### 4.1.5 Wake Decay Formula

Besides the numerical models, a simple analytical model approach to determine the wake length and wind speed recovery was validated based on the flight data collected during WIPAFF [PLATIS et al., in review](#). The analysis of several different case studies (Figure 8) suggests that the recovery in terms of the wind speed ratio (wake wind speed to undisturbed wind speed at hub height) can be characterized by an exponential function as expected from the analytical model described in [EMEIS \(2010\)](#); [EMEIS \(2018\)](#).

The advantage of the model is that the spatial behavior of the reduced wind speed  $u_r(x)$  in the wake at the downstream distance  $x$  is described in a single equation. It solely depends on the initial wind speed deficit  $u_{r0}$  directly downstream of the wind farm and the wake recovery rate  $\alpha$ .

$$u_r(x) = u_f + (u_{r0} - u_f) \exp(-\alpha x) \quad (4.4)$$

where  $u_f$  is the undisturbed (free) wind speed (outside the wake) at hub height. The wake recovery rate  $\alpha$  is

$$\alpha = \frac{K_m}{(\Delta z)^2}, \quad (4.5)$$

where  $K_m$  is the momentum exchange coefficient. The height  $z = h + \Delta z$  describes the height where the undisturbed wind speed is reached above the wind farm.

By testing the analytical model against the airborne data set, we showed in [PLATIS et al. \(in review\)](#); [CAÑADILLAS et al. \(2020\)](#) that the analytical model performs very well as a first-order approximation. This strengthens the hypothesis that the vertical downward momentum flux is the dominating factor for the wake recovery. Best agreement of the exponential wake recovery curve with the observations was achieved for the case study for Flight 31 (Figure 4). The wind data was extracted based on the method described in [PLATIS et al. \(in review\)](#) and plotted in Figure 8, showing the relative wind speeds between the wind speed in the wake and the undisturbed speed behind several wind farms during which stable and homogeneous conditions prevailed. Further results are discussed in detail in [PLATIS et al. \(in review\)](#); [CAÑADILLAS et al. \(2020\)](#).

A drawback of the analytical model is the determination of the separation height between the hub height and the undisturbed flow above the wind park which must be specified in order to determine the decay coefficient in the exponential wake recovery relation as already noted by [PEÑA and RATHMANN \(2014\)](#). It is also expected, that  $\Delta z$  might not be constant along the wake. Further, the impact of the park layout on the intensity and length of the wake is only covered by the analytical model through the initial deficit. Apart from that, the decay coefficient in the analytical model does not depend on the turbine-induced turbulence left over from the wind park, but only on the upstream conditions. As expected by [PORTÉ-AGEL et al. \(2020\)](#) a modification of

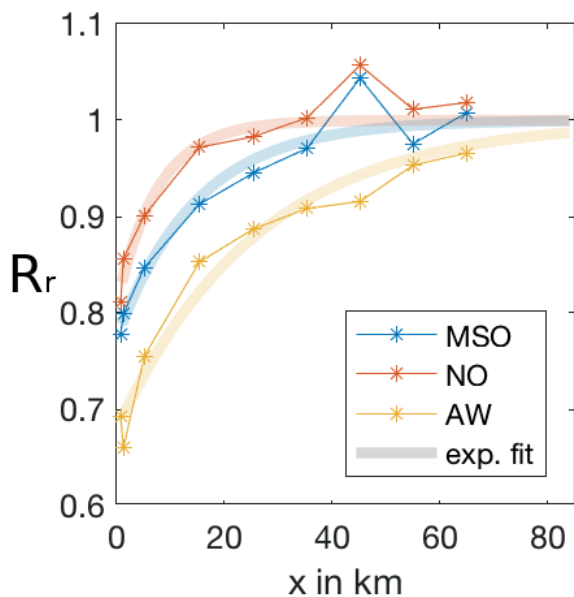


**Figure 8:** Wind speed ratio  $R_r = \frac{u_r}{u_f}$  between the wind speed inside ( $u_r$ ) and outside the wake ( $u_{um}$ ) of flight 31 on August 8, 2017. Dots indicate the measured ratios  $R_r = \frac{u_r}{u_{um}}$  and the line the exponential fit according to the analytical model. Blue indicates the wind speed analysis in the wake downstream of the wind farm Meerwind Süd/Ost (MSO), red Nordsee Ost (NO) and yellow Amrumbank West (AW). Adapted from PLATIS et al. (in review)

the atmospheric stability (e.g.  $u_*$ ) by forming a farm-induced internal boundary layer (IBL) is likely and has to be considered in further editions of this model.

#### 4.1.6 Wakes change the sea surface

Wakes downstream wind parks are visually detectable on SAR images and usually characterized by dark streaks in line with wind direction (Figure 2). However, some images show brighter areas (increase of NRCS and thus wind speed) within the first 10 km downstream the wind parks. An example of an increase of NRCS downstream of the wind park is shown on Figure 9 acquired on 18 June, 2017 at 05:48 UTC during stable stratification (air temperature is 16 °C, while SST is 15.4 °C). This leads to an inferred increase of wind speed in Figure 9b, which is an unusual behavior. The mechanism of this behaviour is unknown. Nevertheless, a theoretical model was proposed in DJATH et al. (2018), which tried to explain this atypical observation by an increased downward momentum flux associated with increased turbulence generated by the wind park. Indeed, the turbulence, which is generated mechanically by the wind turbines, leads to an increase of friction velocity and radar cross section. The turbulence slowly dissipates downstream and after some distance the downward momentum flux is not effective any more. Mechanisms of this kind can be expected to be most effective in atmospheric stable stratification with strong vertical wind speed gradients. The SAR observations are confirmed by airborne laser scanner observations: Within the wake,

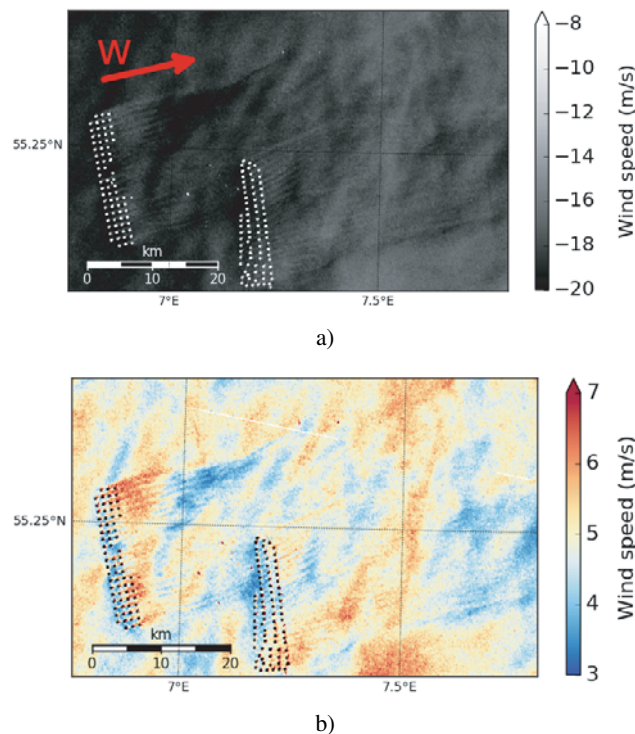


**Figure 9:** Normalised radar cross section (a) associated with sea surface roughness as derived from a Sentinel-1B image acquired on 18 June 2017 at 05:48 UTC (Copernicus Sentinel data [2007]) and derived near surface wind speed (b) showing an increase of NRCS and wind speed within the first 10 km downstream Sandbank (wind park on the left) and DanTysk (wind park on the right) wind parks. The red arrow indicates the wind direction.

the reflectance is significantly enhanced (Figure 10c). An explanation is the flatter surface, which reflects back more energy of individual laser pulses, as they are only little scattered. Further, the number of returned pulses is reduced. A smoother surface reflects the laser pulses more directed, reducing the probability of receiving a reflected laser pulse.

## 4.2 On hypothesis 2: Wakes and increased turbulence

### 4.2.1 Turbulence in the wake

The reduction of the wind speed by wind turbines leads to an area of low wind speed which can generate large horizontal shear at the boundary between the undisturbed wind field and the wake. For flights perpendicular to the wake at hub height, the measurements show strongly enhanced turbulence parameters at the edges of the wakes. For pronounced far-reaching wakes, the turbulent kinetic energy (TKE) at the edges of the wake is still at the same level several 10 km behind the wind park (Figure 10b). During the airborne measurements, the enhanced aircraft vibrations during entering and leaving the wake were noticeable to the crew. Turbulence was found to be particularly enhanced for high wind speed gradients between the wake and the undisturbed flow

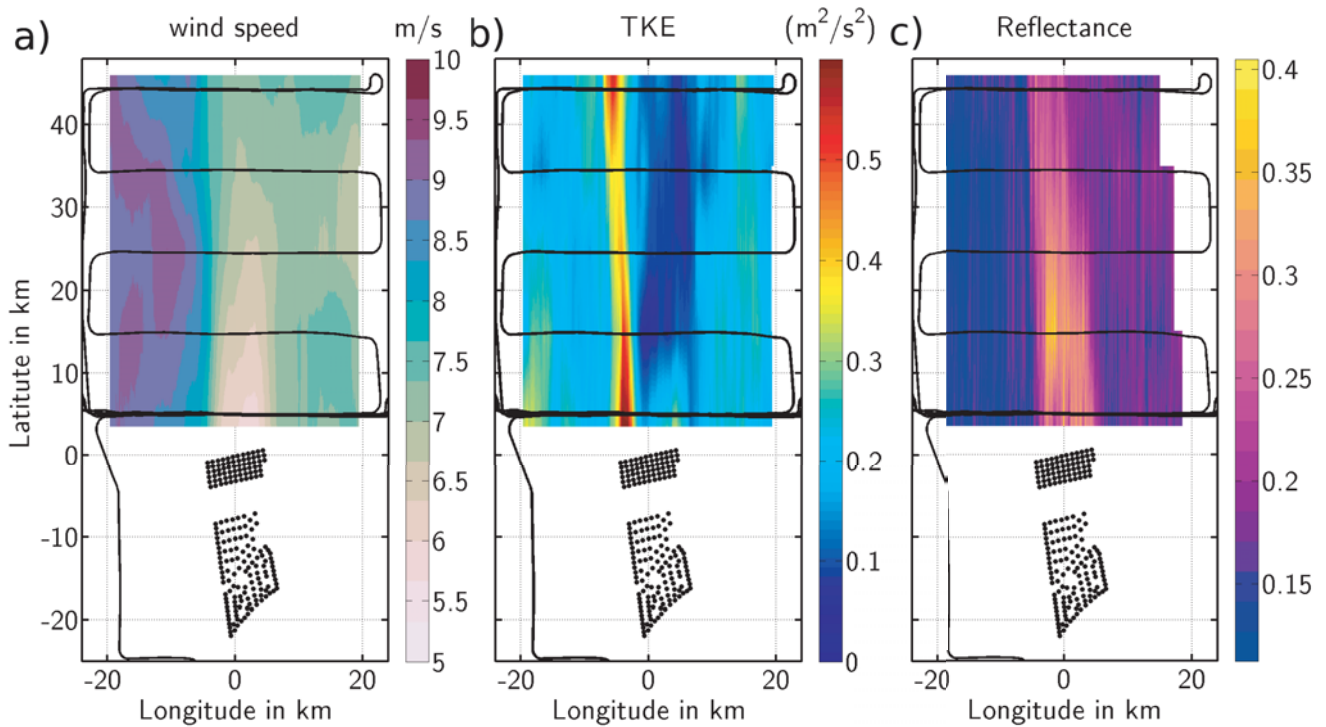


**Figure 10:** Measurements of wind speed (a), turbulent kinetic energy (b) and surface reflectance (c) downwind of the wind parks Amrumbank West, Nordsee Ost and Meerwind Süd/Ost. The measurement flight took place on 10 September 2016. Adapted from [PLATIS et al. \(2018\)](#).

(Figure 10a, b), and for denser wind park geometries. In contrast, within the wake, turbulent kinetic energy is reduced even compared to the undisturbed flow (Figure 10b).

As any change in wind field at the turbine level affects also the sea surface, SAR is capable of detecting the horizontal shear on the edge of the wake through the roughness as well. Figure 9a shows an example of the roughness by the indication of the Normalized Radar Cross Section (NRCS), obtained by Sentinel-1A on June 18, 2017 at 05:48 UTC during stable conditions (air temperature at 50 m was 16 °C and 15.4 °C for the sea surface temperature). Strong increases of NRCS and friction velocity can be seen at the boundaries of wakes downstream wind parks at the northern edge of the two wind parks.

Similarly, the derived wind speed at 10 m altitude (Figure 9b) using the geophysical model function CMOD5N GMF ([HERSBACH et al., 2007](#); [VERHOEF et al., 2008](#)) tuned for C-band displays an increase of amplitude at the edge. These features can be explained by the considerable horizontal shear that exists between the wind field inside the wake and outside the wake. This shear leads to an increase in turbulence, which is also captured in numerical model simulations ([ABKAR and PORTÉ-AGEL, 2015a](#)). The higher turbulence levels at the boundaries of wakes have also been confirmed by airborne lidar surface roughness measurements ([PLATIS et al., 2018](#)), see Figure 10. This turbulence then causes an increase in the downward momentum flux, which can

explain a growth of the friction velocity and hence the radar cross section. This effect can be expected to be particularly effective in stable situations with strong vertical wind speed gradients. These are actually the conditions where wakes are most visible on SAR images. A semi-empirical model to describe the effect of increased downward momentum flux associated with turbulence on surface roughness measured by SAR is given in [DJATH et al. \(2018\)](#).

#### 4.2.2 TKE above the wind park

The mixing above offshore wind parks determines the wake recovery as pointed out in [EMEIS \(2010\)](#). Consequently, mesoscale WPPs should represent the enhanced mixing above offshore wind parks to capture the correct wake extent. In [SIEDERSLEBEN et al. \(2020\)](#) we presented three aircraft case studies, where the TKE above the wind parks Godewind and neighbouring wind parks Nordsee Ost and Meerwind Süd/Ost was measured and compared to mesoscale simulations.

The most important ingredient for capturing the TKE above offshore wind parks with WPPs are correctly simulated upwind conditions. The WPP of [FITCH et al. \(2012\)](#) captured the enhanced TKE above the wind parks Godewind 1, 2 during onshore winds. In contrast, the model overestimated the TKE above the wind parks during offshore winds. By the use of vertical profiles taken by the aircraft close to the coast, we showed that the boundary layer parameterization (MYNN 2.5, [NAKANISHI and NIINO, 2004](#)) was not able to represent the

transition from land to open ocean close to the coast in case of offshore winds. Hence, we suggest the deviation of the simulated and observed TKE above offshore wind parks is largely rooted in the deviation of the simulated and observed upwind conditions. These results agree with the findings in [SIEDERSLEBEN et al. \(2018a\)](#) (Section 4.1.4) where the overestimated extent of the wake was related to deviations between the simulated and observed stratification of the atmosphere.

We recommend using the TKE source of the WPP of [FITCH et al. \(2012\)](#) for offshore wind park simulations during stable conditions, especially for simulations having a horizontal grid coarser or equal to 5 km. For example, simulations with a horizontal grid size of 16 km did not capture the enhanced mixing over the wind parks although the WPP of [FITCH et al. \(2012\)](#) adds additional TKE to the model to account for the not resolved shear within the simulations.

The WPP of [FITCH et al. \(2012\)](#) adds too much TKE at the upwind side of a wind park. During two case studies it was observed that TKE above the wind parks increased with the path of the air through the wind park resulting in a higher TKE at the downwind side of a wind park than on the upwind side. In contrast, the WPP simulated the highest TKE at the upwind side of the wind park associated with the highest wind speeds and wind park density at the front row turbines. On the other hand, the wind speed deficit is underestimated with a disabled TKE source. Therefore, we suggest to use the TKE source for stable conditions ([SIEDERSLEBEN et al., 2020](#)) although the TKE at the upwind side of the wind park might be overestimated.

#### 4.2.3 Wave-number spectrum vs. stability

Wave-number spectra were computed from the 10 m-wind speed derived from the SAR dataset taking into account the stability conditions based on the thermal stratification from the FINO1 data. The spectral analysis is performed for the period September 2016 to May 2017 and considered stable and unstable stratification cases. The results for all stability cases are shown in Figure 11. Each spectrum represents the average over the considered period. Although their spectral forms appear to be different at high wavenumber, the shapes look quite similar in general at low wavenumber. The slope is quite close to the  $k^{-5/3}$  power law ([POND et al., 1966](#); [KAIMAL et al., 1972](#); [NICHOLLS and READINGS, 1981](#); [CHIN et al., 1998](#); [WIKLE et al., 1999](#); [CHO et al., 1999b](#); [CHO et al., 1999a](#); [HÖGSTRÖM et al., 2002](#); [TULLOCH and SMITH, 2009](#); [XU et al., 2011](#)).

The change in stability does not affect the spectral slope in general, but rather modifies the amplitude of spectral power. The spectral power for unstable conditions (green curve in Figure 11) is indeed higher than the spectral power of stable conditions (black in Figure 11). This analysis is in agreement with the previous works ([KAIMAL et al., 1972](#); [NICHOLLS and READINGS, 1981](#); [DJATH and SCHULZ-STELLENFLETH, 2020](#)).

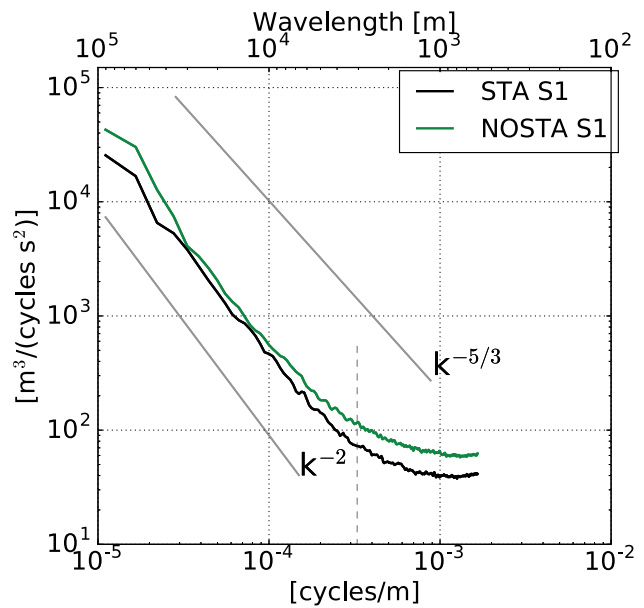


**Figure 11:** Wavenumber spectra computed from near-surface wind fields derived from Copernicus Sentinel-1 data. “STA” stands for stable cases (black curve) and “NOSTA” for unstable cases (green curve).

The high spectral power associated with the unstable stratification confirms that the unstable flows are more turbulent than stable flows. Within the wind park wake context, the generation of turbulence increases mixing and therefore dampens the wake, which lead to having no or short wakes during unstable conditions, while long wakes are pronounced for stable stratification ([CHRISTIANSEN and HASAGER, 2005](#); [DJATH et al., 2018](#)).

#### 4.2.4 Anisotropy spectra aligned wind direction

2D wind spectra were also computed from the mean normalised wind speed (Figure 12). As the stable atmospheric boundary layers are favorable conditions, where wakes are most pronounced, the spectrum is estimated by averaging over the spectra of SAR derived wind fields for stable cases as derived from FINO1. The spectrum is oriented with the wind direction along the horizontal axis. It is interesting to note, that the isolines are bunched in the wind direction, at least for wave lengths shorter than about 10 km. This is equivalent to the occurrence of wind field structures, which are aligned in wind direction. For instance, the atmospheric boundary rolls are aligned with wind direction and are used to estimate the wind direction on SAR images ([KOCH, 2004](#)).

### 4.3 On hypothesis 3: Impact on other wind parks downstream

The impact of far wakes on the environment and on other wind parks depends on the wake length and on the shape of the wind speed recovery within the wakes. In [CAÑADILLAS et al. \(2020\)](#) data from 11 flight measurements collected within the wakes at several downstream

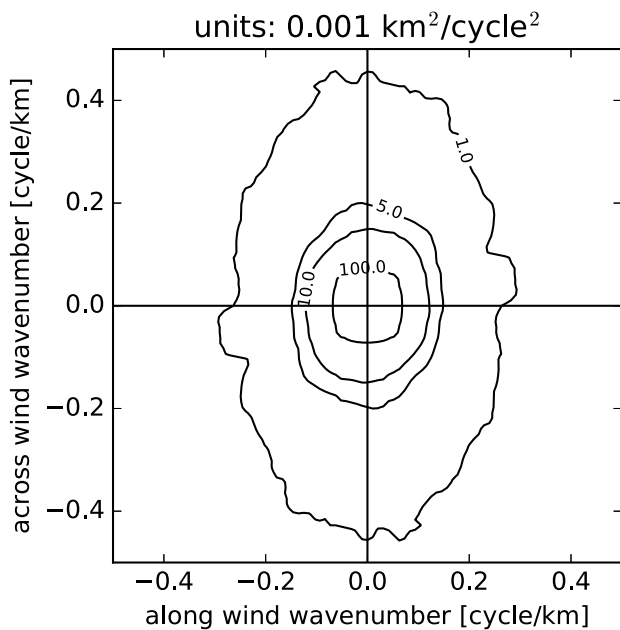


**Figure 12:** Mean 2D wind modulation spectrum estimated from SAR derived normalised wind field spectra.

distances of two offshore wind park clusters were analyzed.

A method was developed to extract the wake recovery function of each measurement flight and a median value was computed for each stable and neutral/unstable atmospheric conditions group. It allowed to calibrate the engineering model WindFarmer used in WIPAFF project. For further details please refer to CAÑADILLAS et al. (2020).

The findings from this study support the results in Section 4.1.1–4.1.2 that stable stratifications is associated with significantly longer wakes characterized by a slower wind speed recovery compared to unstable conditions. The results show that the average wake length under stable conditions exceeds 50 km, while under neutral/unstable conditions, the wake length typically extends to 15 km similar to the results presented in Section 4.1.2. The default settings of the engineering model WindFarmer have to be modified to account for a slower wind speed recovery in stable stratification, as the observed length of wakes under these conditions highly exceeds the wake length arising from the default settings (see Figure 7).

The examination of the effect of the modified recovery on the park efficiency of an isolated downstream wind farm cluster reveals that, for distances > 30 km, the calculated reduction of the wind park efficiency does not exceed 0.5 %. This is considered to be a lower limit of the actual economic effect, as distances between most wind park clusters in the German exclusive economic zone (EEZ) and other offshore regions are < 30 km. However, modelling wakes at distances < 30 km downstream requires modification of not only the stability behaviour of the wind speed recovery, but also of the direct wake and IBL models.

### 4.3.1 Influence of park architecture

The effect of wind park architecture was estimated when distinct wakes were visible downstream of single wind parks within the same atmospheric conditions. As presented in PLATIS et al., in review this was the case for the Flights 25, 30 and 31 within the WIPAFF project. Here, a distinct example is shown in Figure 4 for the case study Flight 31. The wakes of the two adjacent parks Meerwind Süd/Ost (MSO) and Nordsee Ost (NO) are similar in their length (15 to 21 km). However, they differ in the initial wind speed deficit, i.e. 29 % for MSO and 19 % for NO. The wake of the very dense wind park AW is significantly longer at 38 km with initial wind deficit of 28 %. Other case studies showed similar observations in PLATIS et al., in review. As a consequence, it can be concluded that a clear influence of the park layout is evident and longer wakes appeared with a denser alignment of wind turbines in contrast to a low-density wind park. Therefore, to minimize the impact of downstream installations a less narrow alignment of the wind turbines could be considered in future offshore wind park planning.

### 4.4 On hypothesis 4: Impact of wind-park wakes on local climate and surface fluxes

Given the warming and cooling in the rotor layer associated with the enhanced vertical mixing at the rotor area (Section 4.1.3) the question arises whether wind parks can alter local climate.

A change in local climate would be equal to a change in the energy budget of the atmosphere. According to TRENBERTH et al. (2001) and PORTER et al. (2011) a change in the energy budget of the atmosphere is associated with a change in radiation budget and/or in the turbulent surface fluxes. Hence, it is relevant whether the temperature and moisture changes at hub height as investigated in SIEDERSLEBEN et al. (2018b) are associated with temperature and moisture changes at the surface that in turn could enhance the turbulent fluxes at the surface resulting in a change of the energy budget of the atmosphere. Temperature and moisture changes were well observed on 10 September 2016, hence, we investigated the potential impact of all planned and existing offshore wind parks in the German Bight on the turbulent surface fluxes (i.e. sensible and latent heat flux) by the use of WRF simulations. The locations of the planned wind parks follow plans of the Bundesamts für Seeschifffahrt und Hydrographie (BSH) published in 2015 (Figure 13). Although such a numerical simulation can not give an answer on whether offshore wind farms have an impact on the local climate or not, we can still determine the maximal impact of offshore wind farms on the boundary layer by simulating a day, that was characterised by large wakes in the German Bight. Based on these results further studies should be conducted, investigating the impact of offshore wind farms on the local climate.



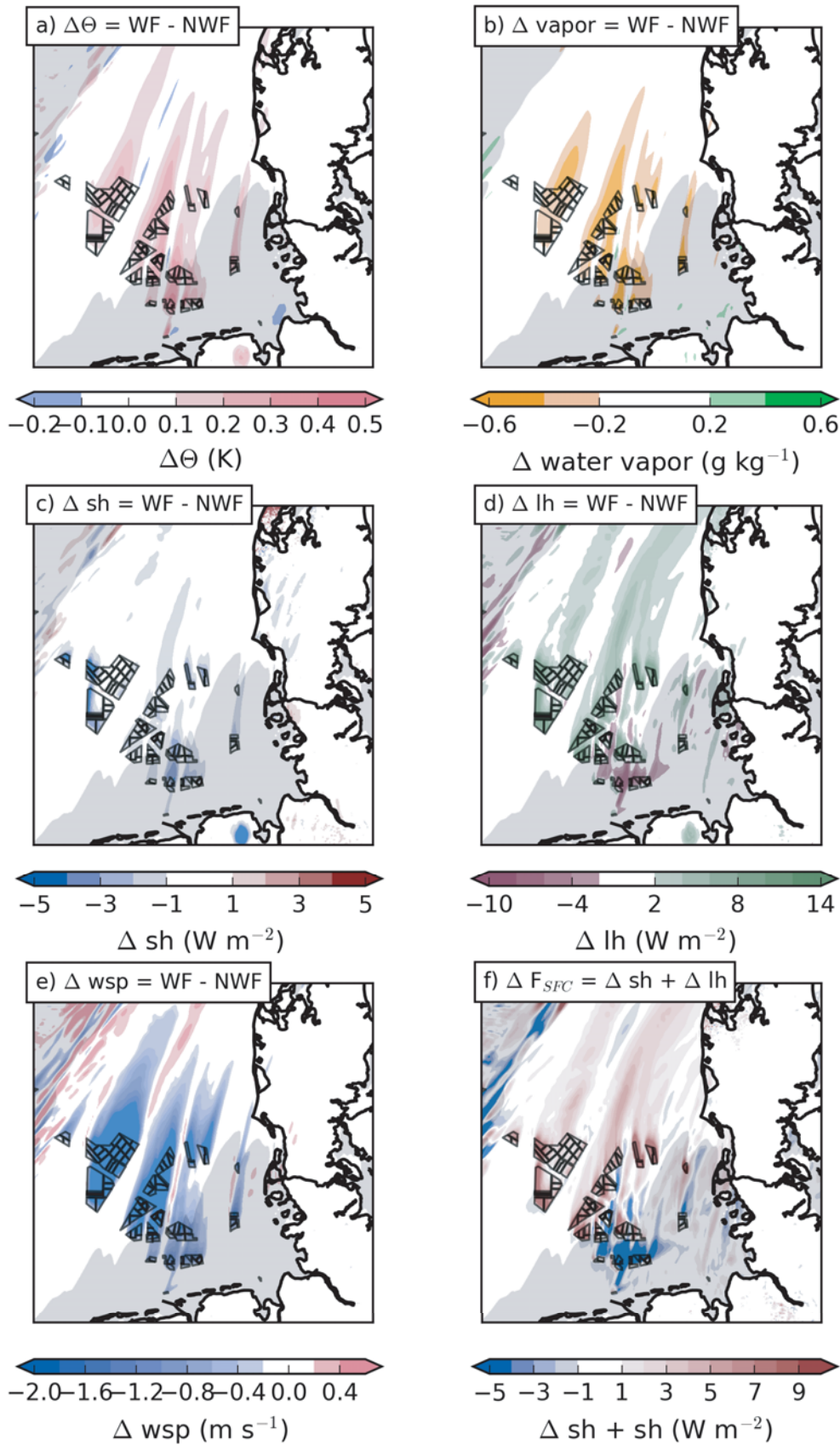


**Figure 13:** The impact of all potentially planned offshore wind parks at the North Sea for the meteorological situation 10 September 2016 averaged from 08:00 UTC to 09:00 UTC. Shown is the difference at hub height of (a) potential temperature, (b) water vapor mixing ratio and (e) wind speed between a simulation with wind parks (WF) and a simulation with no wind parks (NWF). The resulting changes of sensible heat flux (sh) and latent heat flux (lh) are shown in (c) and (d). The sum of differences in sensible and latent heat flux is shown in (f). The gray shading depicts areas where the SST is higher than the air temperature. Taken from [SIEDERSLEBEN \(2019\)](#).

Although some wind parks in the simulations are much bigger than already existing wind parks in the German Bight, the impact on temperature and water vapor at hub height is not larger than observed on 10 September 2016 (Figure 13a–b). For example, the simulations suggest a warming and a drying at hub height in the order of 0.5 K and  $0.5 \text{ g kg}^{-1}$  downwind of the large offshore wind park cluster located in the west of the domain. For comparison, the already existing wind parks around Amrumbank West cause a similar warming signal at hub height.

The warming induced by the wind parks in the rotor area is partly associated with a decreased sensible heat flux at the surface (Figure 13c). Two different processes drive the reduction of the sensible heat flux rooted in the different temperature gradients between the SST and the lowest model level located at 17 m AMSL (Figure 14). On 10 September 2016 we encountered areas with a lower air temperature than SST (i.e. gray shaded area in Figure 13, SIEDERSLEBEN, 2019). During non-waked conditions the sensible heat flux is orientated towards the atmosphere in these regions, resulting in a warming of the lower atmosphere (Figure 14a). According to aircraft measurements recorded on 10 September 2016, the warming induced by the wind turbines was also effective at 60 m AMSL (see Figure 4a in SIEDERSLEBEN et al., 2018b). The simulations indicate that the warming at the rotor area even spread down to the ocean's surface. Consequently, a higher surface temperature results in a reduction of the temperature gradient between air temperature and SST that in turn weakens the sensible heat flux towards the atmosphere as it is schematically sketched in Figure 14a). In contrast, the sensible heat flux is orientated towards the ocean in case of a lower SST than air temperature (*not* gray shaded area in Figure 13) during non-waked conditions. However, a warming at the ocean's surface results in an increased temperature gradient between air temperature and SST, resulting in an larger sensible heat flux pointing towards the ocean (Figure 14b). Therefore, the net effect of the warming at the surface is an increased sensible heat flux towards the ocean (Figure 14b). However, the changes in the sensible heat flux are not larger than  $3 \text{ W m}^{-2}$ .

The impact of offshore wind parks on the latent heat flux is determined by the temperature gradient between SST and the temperature at the lowest model level (Figure 13d). In areas with a higher SST than air temperature the simulated latent heat flux is decreased. In contrast, the latent heat flux is increased in areas with a higher air temperature than SST. As humidity usually has a strong vertical gradient in the marine boundary layer (decreasing with height), the latent heat flux is pointing upward regardless of the temperature gradient. Obviously, the dryer air within the wakes of larger offshore wind parks enhances the vertical moisture gradient, that in turn should enhance the latent heat flux towards the atmosphere. However, this is only true for areas with a higher air temperature than SST (Figure 13d). In contrast, in regions with a lower SST than air temperature,

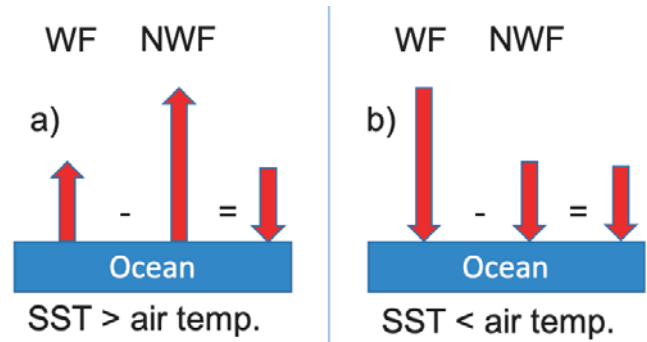


**Figure 14:** Schematic sketch of impact of offshore wind parks on the sensible heat flux in case of (a) a SST higher than the air temperature and (b) vice versa. WF is a wind park simulation with the wind farm parameterization turned on, while NWF has the parameterization switched off. Taken from SIEDERSLEBEN (2019).

we observe a decreased latent heat flux (purple contours in Figure 13e), although the latent heat flux is supposed to increased due to dryer air within the wake. Hence, we suggest, that the weakening of the temperature gradient between SST and air temperature mainly drives the changes in the latent heat flux.

The overall change in the surface fluxes is driven by the changes in the latent heat flux (Figure 13f), in case of inversions close to the rotor height. As the impact on 10 September 2016 on the latent heat flux is almost twice as much than the changes in the sensible heat flux the net impact on the surface fluxes is dominated by the changes in latent heat flux. As the changes in the latent heat flux are determined by the temperature gradient between the lowest model level and SST, so is the overall impact: A cooling effect is present in areas with a higher air temperature than SST and vice versa. However, we only observed a change in the latent heat flux associated with the existence of an inversion close to rotor height SIEDERSLEBEN et al., 2018b. Hence, the latent heat flux only dominates the overall impact in case of an inversion close to the rotor area otherwise only the sensible heat flux is affected.

The effects discussed above were observed in six of our flights, nevertheless for a sound climatology reliable conclusion, further studies are mandatory.

## 5 Conclusion/Outlook

A unique dataset from airborne *in situ* data, remote sensing by laser scanner and SAR gained during the WIPAFF project proves that wakes up to several tens of kilometers exist downstream of offshore wind farms. The wind speed deficits in the wakes and their length tend to be larger in stable than in unstable conditions. The results show that the average wake lengths under stable conditions exceed 50 km, while under neutral/unstable conditions, the wake length amounts to 15 km or less. Data also indicates that a denser wind park layout increases the wake length additionally due

to a higher initial wind speed deficit. Turbulence occurs at the edges of the wakes due to shear between the reduced wind speed inside the wake and the undisturbed flow. The intensity depends on the strength of the wind speed gradient and is further enhanced for denser wind park geometries. In contrast, within the wake, turbulent kinetic energy is reduced even compared to the undisturbed flow.

The observational data of the WIPAFF project was further compared to industrial, analytical and mesoscale models. The respective models show in general a good correlation with the measured wake lengths, nevertheless, they also show deficiencies:

- As a first order approximation the analytical model seems to work well, however it has to be optimized to be able to account for the park layout and turbine turbine-induced turbulence left over from the wind park. This has to be improved in the future.
- The engineering model WindFarmer underestimates the wake length during stable conditions when using the default settings. Therefore, default settings of the engineering model WindFarmer have been modified to account for a slower wind speed recovery in stable stratification (CAÑADILLAS et al., 2020).
- The mesoscale WRF model enables the simulation of a complete area like the German Bight. However, the results of the simulations show that the WRF model is highly sensitive to the upwind conditions. During offshore winds (advecting warm air over the ocean) strong inversions developed at rotor height that are challenging for a mesoscale model. Hence, the up-stream wind speed was sometimes underestimated due to a wrongly predicted stratification in the model.

To accomplish accurate predictions of the wind energy production by numerical models, further effects have to be taken into account, e.g. the blockage effects of wind parks or how the state of the operation of wind parks influences the wakes, which requires the analysis of operational data. As such data was not available in the WIPAFF project, this is a topic of future research and implementation in numerical models.

Besides the wake effects, the influence of offshore wind parks on the marine boundary layer was investigated by using the airborne observations and the WRF model. The impact on the marine boundary layer depends on several parameters. First of all, wind parks can cause a warming or a cooling at hub height during stable conditions as discussed in Section 4.1.3. However, the inversion can also be located such that a cooling at the ocean's surface takes place, although we only presented here a warming case. Secondly, only in case of a pronounced inversion close to hub height we simulated and observed a change in the water vapor mixing ratio corresponding to changes in latent heat flux. Thirdly, the net impact on the latent heat flux was determined by the temperature gradient between SST and the ambient air temperature.

Several potential impacts of offshore wind parks on the marine boundary layer were not discussed in this study i.e the formation of clouds. HUANG and HALL (2015) and BOETTCHER et al. (2015) showed that large offshore wind park could have an influence on the cloud cover. Consequently, wind parks could have an influence on the radiation budget as well. These aspects were not presented as we could not identify a clear impact of offshore wind parks on the cloud cover or any radiation budget due to lacking equipment.

Given the high sensitivity of the simulated impacts of offshore wind farms, studies making general statements about the impacts of offshore wind farms based on numerical climate or mesoscale models should be carefully examined. As discussed above, simulated impact on the local climate is extremely sensible to the simulated stability in the lowest 200 m of the marine boundary layer. Within the WIPAFF project we showed that mesoscale simulations were lacking to represent the stable boundary layer during offshore winds close to the coast, although most wind parks are in the transition area from coast to open sea and their impact is largest during stable conditions (SIEDERSLEBEN et al., 2018b).

The above documented results may have several consequences.

## 5.1 Wind direction-based layout of wind parks

Analysis of data from FINO1 for the year 2005 shows a clear correlation between wind direction and atmospheric stratification in the North Sea (EMEIS et al., 2016). Stable situations are coupled to the main wind direction (South-West). This direction-stability correlation is assumed to be typical for the two temperate latitude west-wind belts on both hemispheres of the globe, because it is caused by the usual sequence of warm sector winds having a poleward component followed by cold sector winds having an equatorward component in eastward moving low-pressure systems. The WIPAFF results clearly documented the dependence of the wake intensity and wake length on atmospheric stratification. Therefore, it could be advisable that wind park layout and park cluster layout take this dependence into account. Figure 15 shows a possible array of wind parks in the German Bight which reflects this correlation. Distances between single turbines within wind parks and between entire parks are larger along the most frequent direction of stably stratified flow (from Southwest to Northeast) and they are shorter along the perpendicular direction of unstably stratified flow.

## 5.2 Additional measurement requirements and stability measures for the marine BL

For future estimations of wind park power output and for improving analyses of offshore wind park wakes, a crucial parameter was found to be profiles of temperature and the stability parameter. Temperature inversions occur at different altitudes above, below and within the rotor area. A near-surface, predominantly convective layer

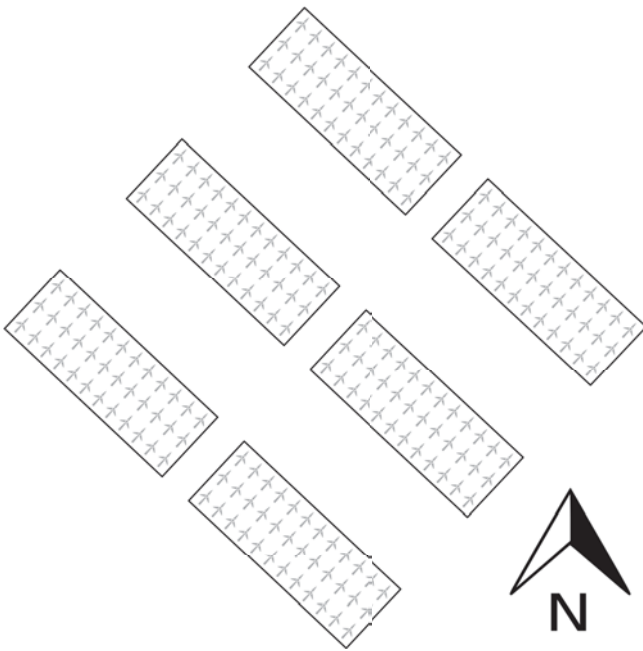


**Figure 15:** Schematic of stability-dependent wind park layout in the German Bight. Crosses denote single wind turbines and boxes indicate wind parks. North is towards the top. (Adapted from [EMEIS et al., 2016](#))

may be present and an inversion with more stable conditions may be found aloft. Therefore, a simple approach for defining stability, e.g. the temperature difference between the sea surface and the atmosphere at one particular altitude, is not suitable for describing stability conditions and wake development. In addition, other stability parameters are partly inconsistent with each other. Therefore, defining stability measures for the marine boundary layers which can be representative for atmospheric stability for an offshore wind park and the evolution of wind park wakes is a very crucial task for the future.

Moreover, the representation of temperature profiles in numerical simulations and the deduced stability need higher accuracy and improvement. The comparison of the airborne observations and WRF simulations show potential for improving the representation of coastal effects, where temperature profiles develop from the coast to the wind parks. For example, from the simulations of 15 October 2017 two profiles are compared to the simulations, one close to the coast, one further offshore (Figure 16). Close to the coast the simulation and observation show an inversion. However, the inversion of the simulation is located above the rotor area, whereby the inversion in the observations is located within the rotor area. Further offshore, the performance of the model improves slightly. Nevertheless, the height of the inversion is still overestimated by 150 m. The numerical simulations were performed with the setup as described in [SIEDERSLEBEN et al. \(2018a\)](#). As the development of the stability for the flow above the coast strongly influences the wake extent, an improvement of the simulations is

required for correctly representing the inflow conditions reaching the wind park. The availability of additional measurements of temperature profiles at a coastal and at an offshore locations could serve as reference and would contribute to a better understanding of the processes in the atmospheric boundary layer and the interaction with wind parks and lead to improvement of numerical simulations.

### 5.3 Impact on cloud development

On three out of 41 measurement flights, the formation of small patches of clouds directly above the wind park was observed. The cloud patches were transported downwind. No such clouds were observed in the lee and next to the wind park. Cloud formation was observed on days with relative humidity close to saturation, and slightly stable conditions. The documentation of the clouds was attempted by photographing. However, the image quality was hampered by other cloud layers above. The sensors on board were not suitable for systematic analyses of the phenomenon and its importance. This should be addressed in future research in combination with the analysis of downward heat and humidity fluxes above wind parks.

### 5.4 Future SAR data evaluation

About one third of the SAR scenes with visible wake structures show increased SAR radar cross section values for roughly the first 10 km of the wake downstream the wind park. There are several approaches to explain this phenomenon, which seems to be a paradox at first sight. One possible explanation proposed in [DJATH et al. \(2018\)](#) is based on the hypothesis of increased downward momentum fluxes caused by turbulence introduced by the wind turbines. Making this assumption, SAR data would provide very valuable information on the advection and dissipation of turbulence in the vicinity of offshore wind parks. However, observational evidence is missing to confirm or refute this or a number of other possible mechanisms to explain the effect. Measurements are a challenge in this context, because the sea surface roughness measured by the radar is strongly dependent on the detailed structure of the atmospheric boundary layer close to the water. New measurement technologies and sampling approaches are currently investigated to obtain more information on this important region. These activities are not only of high value to improve our understanding of the atmospheric processes around offshore wind parks, but are of more general relevance in the context of atmosphere/ocean interaction, which is a field of intense research worldwide.

A topic that is directly related to the phenomenon just described, is the derivation of wind speed information above the sea surface from microwave radar data. Radar measurements have a direct physical connection to the friction velocity at the surface, but wind speeds at higher levels depend on the stability conditions in

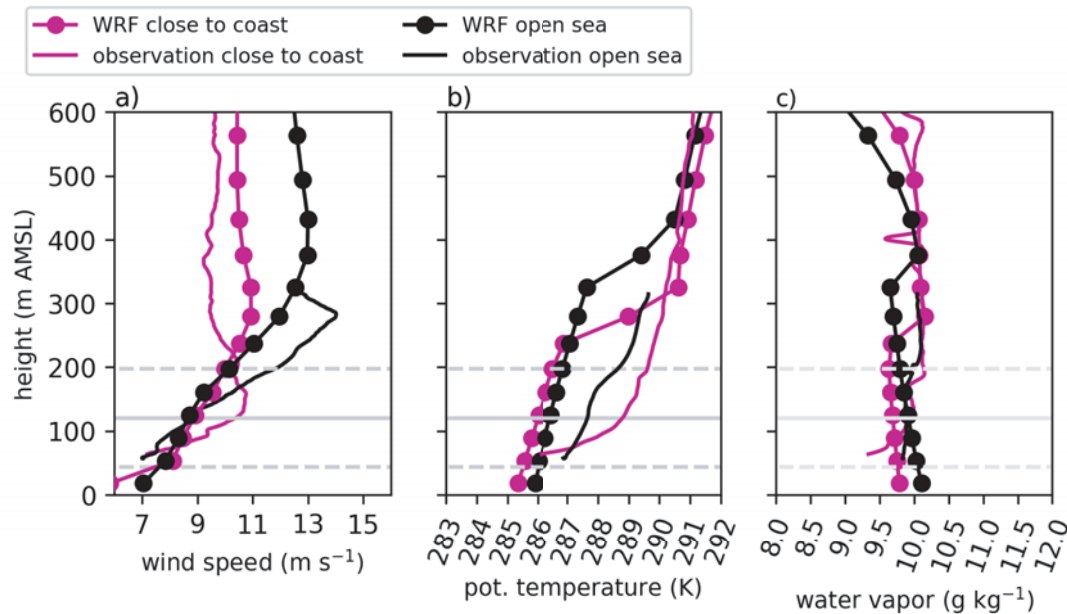


**Figure 16:** Vertical profiles of wind speed (a), potential temperature (b) and water vapour mixing ratio (c) obtained by probing the atmosphere with the research aircraft on 15 October 2017 close to the coast (magenta solid lines) and further offshore (black solid lines). The corresponding locations of the vertical profiles are shown in detail in Figure 1. The interpolated WRF data along the climb flights is shown with the solid lines having the circles on top, whereby each circle represents a vertical level of the simulation.

the boundary layer, which are usually not well known. The empirical functions used for SAR wind speed retrieval so far were usually derived based on observation data sets taken in the open ocean, making very simplifying assumptions about the conditions in the atmosphere. This is another area of research, where more sophisticated measurements of the atmospheric boundary layer in near coastal areas could help to optimise the exploitation of SAR information for offshore wind park applications. This issue is also related to the more general question about the optimal integration of satellite, *in situ* and model data to provide efficient information products to the offshore wind park community.

## Acknowledgments

The authors thank the aircraft crew of the WIPAFF campaign, RUDOLF HANKERS, THOMAS FEUERLE, MARK BITTER and HELMUT SCHULZ from the Technische Universität Braunschweig for their great support. The project WIPAFF is funded by the German Federal Ministry for Economic Affairs and Energy (Bundesministerium für Wirtschaft und Energie) on the basis of a decision by the German Bundestag under grant number: FKZ 0325783.

## References

ABKAR, M., F. PORTÉ-AGEL, 2015a: Influence of atmospheric stability on wind-turbine wakes: A large-eddy simulation study. – *Phys. Fluids* **27**, 035104.

ABKAR, M., F. PORTÉ-AGEL, 2015b: A new wind-farm parameterization for large-scale atmospheric models. – *J. Renew. Sustain. Energy* **7**, 013121.

AINSLIE, J., 1988: Calculating the flow field in the wake of wind turbines. – *J. Wind Engin. Indust. Aerodyn.* **27**, 213–224, DOI: [10.1016/0167-6105\(88\)90037-2](https://doi.org/10.1016/0167-6105(88)90037-2).

ARMSTRONG, A., R.R. BURTON, S.E. LEE, S. MOBBS, N. OSTLE, V. SMITH, S. WALDRON, J. WHITAKER, 2016: Ground-level climate at a peatland wind farm in Scotland is affected by wind turbine operation. – *Env. Res. Lett.* **11**, 044024.

BÄRFUSS, K., R. HANKERS, M. BITTER, T. FEUERLE, H. SCHULZ, T. RAUSCH, A. PLATIS, J. BANGE, A. LAMPERT, 2019: In-situ airborne measurements of atmospheric and sea surface parameters related to offshore wind parks in the German Bight. – PANGAEA, published online. DOI: [10.1594/PANGAEA.902845](https://doi.org/10.1594/PANGAEA.902845).

BARTHELMIE, R., S. FRANDBEN, P. RETHORE, L. JENSEN, 2007: Analysis of atmospheric impacts on the development of wind turbine wakes at the Nysted wind farm. – In: *European Offshore Wind Conference*, volume **6**.

BARTHELMIE, R.J., L. JENSEN, 2010: Evaluation of wind farm efficiency and wind turbine wakes at the Nysted offshore wind farm. – *Wind Energy* **13**, 573–586.

BARTHELMIE, R.J., K. HANSEN, S.T. FRANDBEN, O. RATHMANN, J. SCHEPERS, W. SCHLEZ, J. PHILLIPS, K. RADOS, A. ZERVOS, E. POLITIS, OTHERS, 2009: Modelling and measuring flow and wind turbine wakes in large wind farms offshore. – *Wind Energy* **12**, 431–444.

BLAHAK, U., B. GORETZKI, J. MEIS, 2010: A simple parameterization of drag forces induced by large wind farms for numerical weather prediction models. – In: *Proceedings of the European Wind Energy Conference & Exhibition*.

BODINI, N., D. ZARDI, J.K. LUNDQUIST, 2017: Three-dimensional structure of wind turbine wakes as measured by scanning lidar. – *Atmos. Measur. Techn.* **10**, 2881–2896.

- BOETTCHER, M., P. HOFFMANN, H.J. LENHART, H. SCHLÜNZEN, R. SCHOETTER, 2015: Influence of large offshore wind farms on north german climate. – *Meteorol. Z.* **24**, 465–480.
- BOSSANYI, E., G. WHITTLE, P. DUNN, N. LIPMAN, P. MUSGROVE, C. MACLEAN, 1980: The efficiency of wind turbine clusters. – In: 3rd International symposium on wind energy systems, 401–416.
- CAÑADILLAS, B., R. FOREMAN, V. BARTH, A. PLATIS, S.K. SIEDERSLEBEN, J. BANGE, A. LAMPERT, K. BÄRFUSS, R. HANKERS, J. SCHULZ-STELLENFLETH, B. DJATH, S. EMEIS, T. NEUMANN, 2020: Offshore wind farm wake recovery: Airborne measurements and its representation in engineering models. – *Wind Energy*, published online. DOI: [10.1002/we.2484](https://doi.org/10.1002/we.2484).
- CHAMORRO, L.P., F. PORTE-AGEL, 2011: Turbulent flow inside and above a wind farm: a wind-tunnel study. – *Energies* **4**, 1916–1936.
- CHIN, T.M., R.F. MILLIFF, W.G. LARGE, 1998: Basin-scale, high-wavenumber sea surface wind fields from a multiresolution analysis of scatterometer data. – *J. Atmos. Oceanic Technol.* **15**, 741–763.
- CHO, J.Y., R.E. NEWELL, J.D. BARRICK, 1999a: Horizontal wavenumber spectra of winds, temperature, and trace gases during the pacific exploratory missions: 2. gravity waves, quasi-two-dimensional turbulence, and vortical modes. – *J. Geophys. Res.* **104**, 16297–16308.
- CHO, J.Y.N., Y. ZHU, R.E. NEWELL, B.E. ANDERSON, J.D. BARRICK, G.L. GREGORY, G.W. SACHSE, M.A. CARROLL, G.M. ALBERCOOK, 1999b: Horizontal wavenumber spectra of winds, temperature, and trace gases during the Pacific Exploratory Missions: 1. Climatology. – *J. Geophys. Res. Atmos.* **104**, 5697–5716.
- CHRISTIANSEN, M.B., C.B. HASAGER, 2005: Wake effects of large offshore wind farms identified from satellite SAR. – *Remote Sens. Env.* **98**, 251–268.
- CORSMEIER, U., R. HANKERS, A. WIESER, 2001: Airborne turbulence measurements in the lower troposphere onboard the research aircraft dornier 128-6, D-IBUF. – *Meteorol. Z.* **10**, 315–329.
- DJATH, B., J. SCHULZ-STELLENFLETH, 2020: Wind speed deficits downstream offshore wind parks – a new automatised estimation technique based on satellite synthetic aperture radar data. – *Meteorol. Z.* **28**, 499–515. DOI: [10.1127/metz/2019/0992](https://doi.org/10.1127/metz/2019/0992).
- DJATH, B., J. SCHULZ-STELLENFLETH, B. CAÑADILLAS, 2018: Impact of atmospheric stability on X-band and C-band synthetic aperture radar imagery of offshore windpark wakes. – *J. Renew. Sustain. Energy* **10**, 043301.
- DNV-GL, 2013a: WindFarmer v.5.2 theory manual. – Technical report, Garrad Hassan and Partners, Ltd.
- DNV-GL, 2013b: WindFarmer v.5.2 validation report. – Technical report, Garrad Hassan and Partners, Ltd.
- DÖRENKÄMPER, M., B. WITHA, G. STEINFELD, D. HEINEMANN, M. KÜHN, 2015a: The impact of stable atmospheric boundary layers on wind-turbine wakes within offshore wind farms. – *J. Wind Engineer. Indust. Aerodyn.* **144**, 146–153.
- DÖRENKÄMPER, M., M. OPTIS, A. MONAHAN, G. STEINFELD, 2015b: On the offshore advection of boundary-layer structures and the influence on offshore wind conditions. – *Bound.-Layer Meteor.* **155**, 459–482.
- EMEIS, S., 2010: A simple analytical wind park model considering atmospheric stability. – *Wind Energy* **13**, 459–469.
- EMEIS, S., 2018: Wind energy meteorology: atmospheric physics for wind power generation. – Springer, 255 + XXVI pp.
- EMEIS, S., S. FRANDBSEN, 1993: Reduction of horizontal wind speed in a boundary layer with obstacles. – *Bound.-Layer Meteorol.* **64**, 297–305.
- EMEIS, S., S. SIEDERSLEBEN, A. LAMPERT, A. PLATIS, J. BANGE, B. DJATH, J. SCHULZ-STELLENFLETH, T. NEUMANN, 2016: Exploring the wakes of large offshore wind farms. – *J. Phys. Conference Series* **753**, 092014.
- FIEDLER, B., A. ADAMS, 2014: A subgrid parameterization for wind turbines in weather prediction models with an application to wind resource limits. – *Adv. Meteor.* **2014**, 696202. DOI: [10.1155/2014/696202](https://doi.org/10.1155/2014/696202).
- FITCH, A.C., J.B. OLSON, J.K. LUNDQUIST, J. DUDHIA, A.K. GUPTA, J. MICHALAKES, I. BARSTAD, 2012: Local and mesoscale impacts of wind farms as parameterized in a meso-scale NWP model. – *Mon. Wea. Rev.* **140**, 3017–3038.
- FOREMAN, R., B. CAÑADILLAS, T. NEUMANN, S. EMEIS, 2017: Measurements of heat and humidity fluxes in the wake of offshore wind turbines. – *J. Renew. Sustain. Energy* **9**, 053304.
- FRANDBSEN, S., 1992: On the wind speed reduction in the center of large clusters of wind turbines. – *J. Wind Engin. Indust. Aerodyn.* **39**, 251–265.
- FRANDBSEN, S., R. BARTHELMIE, S. PRYOR, O. RATHMANN, S. LARSEN, J. HØJSTRUP, M. THØGERSEN, 2006: Analytical modelling of wind speed deficit in large offshore wind farms. – *Wind Energy* **9**, 39–53.
- HANSEN, K.S., R.J. BARTHELMIE, L.E. JENSEN, A. SOMMER, 2012: The impact of turbulence intensity and atmospheric stability on power deficits due to wind turbine wakes at horns rev wind farm. – *Wind Energy* **15**, 183–196.
- HASAGER, C., L. RASMUSSEN, A. PEÑA, L. JENSEN, P.E. RÉTHORÉ, 2013: Wind farm wake: The Horns Rev photo case. – *Energies* **6**, 696–716.
- HASAGER, C., N. NYGAARD, P. VOLKER, I. KARAGALI, S. ANDERSEN, J. BADGER, 2017: Wind farm wake: The 2016 Horns Rev photo case. – *Energies* **10**, 317.
- HASAGER, C.B., P. VINCENT, J. BADGER, M. BADGER, A. DI BELLA, A. PEÑA, R. HUSSON, P.J. VOLKER, 2015: Using Satellite SAR to Characterize the Wind Flow Around Offshore Wind Farms. – *Energies* **8**, 5413–5439, DOI: [10.3390/en8065413](https://doi.org/10.3390/en8065413).
- HERSBACH, H., A. STOFFELEN, S. DE HAAN, 2007: An improved C-band scatterometer ocean geophysical model function: CMOD5. – *J. Geophys. Res. Oceans* **112**, published online. DOI: [10.1029/2006JC003743](https://doi.org/10.1029/2006JC003743).
- HÖGSTRÖM, U., J. HUNT, A.S. SMEDMAN, 2002: Theory and measurements for turbulence spectra and variances in the atmospheric neutral surface layer. – *Bound.-Layer Meteor.* **103**, 101–124.
- HUANG, H.Y., A. HALL, 2015: OFFSHORE WIND DEVELOPMENT IMPACTS ON MARINE ATMOSPHERIC ENVIRONMENT. – Available online at <http://www.energy.ca.gov/2016publications/CEC-500-2016-023/CEC-500-2016-023.pdf>.
- JACOBSON, M.Z., C.L. ARCHER, 2012: Saturation wind power potential and its implications for wind energy. – *Proc of the Natl Acad of Sci USA* **109**, 15679–15684.
- JENSEN, N.O., 1983: A note on wind generator interaction. – Risø National Laboratory Roskilde.
- KAFFINE, D.T., C.M. WORLEY, 2010: The windy commons? – *Env. Res. Econom.* **47**, 151–172.
- KAIMAL, J.C., J.C. WYNGAARD, Y. IZUMI, O.R. COTÉ, 1972: Spectral characteristics of surface-layer turbulence. – *Quart. J. Roy. Meteor. Soc.* **98**, 563–589.
- KATIC, I., J. HØJSTRUP, N. JENSEN, 1987: A simple model for cluster efficiency. – In: W. PALZ and E. SESTO (Eds.): EWEC'86. – Proceedings. Vol. 1, 407–410.
- KOCH, W., 2004: Directional Analysis of SAR images aiming at wind direction. – *IEEE Transactions on Geoscience and Remote Sensing* **42**, 702–710.

- LAMPERT, A., K.B. BÄRFUSS, A. PLATIS, S.K. SIEDERSLEBEN, B. DJATH, B. CAÑADILLAS, R. HANKERS, M. BITTER, T. FEUERLE, H. SCHULZ, T. RAUSCH, M. ANGERMANN, A. SCHWITHAL, J. BANGE, J. SCHULZ-STELLENFLETH, T. NEUMANN, S. EMEIS, 2020: In-situ airborne measurements of atmospheric and sea surface parameters related to offshore wind parks in the German Bight. – *Earth Sys. Sci. Data*, **12**, 935–946.
- LEE, S., M. CHURCHFIELD, P. MORIARTY, J. JONKMAN, J. MICHALAKES, 2012: Atmospheric and wake turbulence impacts on wind turbine fatigue loadings. – In: 50th AIAA Aerospace Sciences Meeting including the New Horizons Forum and Aerospace Exposition, 540.
- LI, X., S. LEHNER, 2013a: Observation of TerraSAR-X for studies on offshore wind turbine wake in near and far fields. – *IEEE Journal of Selected Topics in Applied Earth Observations and Remote Sensing* **6**, 1757–1768.
- LI, X.M., S. LEHNER, 2013b: Algorithm for sea surface wind retrieval from terrasarsar-x and tandem-x data. – *IEEE Transactions on Geoscience and Remote Sensing* **52**, 2928–2939.
- LIN, H., Q. XU, Q. ZHENG, 2008: An overview on sar measurements of sea surface wind. – *Prog. Natural Sci.* **18**, 913–919.
- LISSAMAN, P., 1979: Energy effectiveness of arbitrary arrays of wind turbines. – *J. Energy* **3**, 323–328.
- LUNDQUIST, J., K. DU VIVIER, D. KAFFINE, J. TOMASZEWSKI, 2019: Costs and consequences of wind turbine wake effects arising from uncoordinated wind energy development. – *Nature Energy* **4**, 26–34.
- MARTÍNEZ-TOSSAS, L.A., M.J. CHURCHFIELD, C. MENEVEAU, 2015: Large eddy simulation of wind turbine wakes: detailed comparisons of two codes focusing on effects of numerics and subgrid modeling. – *J. Phys. Conference Series* **625**, 012024.
- MUÑOZ-ESPARZA, D., B. CAÑADILLAS, T. NEUMANN, J. VAN BEECK, 2012: Turbulent fluxes, stability and shear in the offshore environment: Mesoscale modelling and field observations at fino1. – *J. Renew. Sustain Energy* **4**, 063136.
- NAKANISHI, M., H. NIINO, 2004: An improved mellor–yamada level-3 model with condensation physics: Its design and verification. – *Bound.-layer Meteor.* **112**, 1–31.
- NEWMAN, B., 1977: The spacing of wind turbines in large arrays. – *Energy conversion* **16**, 169–171.
- NICHOLLS, S., C.J. READINGS, 1981: Spectral characteristics of surface layer turbulence over the sea. – *Quart. J. Roy. Meteor. Soc.* **107**, 591–614.
- NYGAARD, N.G., 2014: Wakes in very large wind farms and the effect of neighbouring wind farms. – *J. Phys. Conference Series* **524**, 012162.
- NYGAARD, N.G., S.D. HANSEN, 2016: Wake effects between two neighbouring wind farms. – *J. Phys. Conference Series* **753**, 032020. DOI: [10.1088/1742-6596/753/3/032020](https://doi.org/10.1088/1742-6596/753/3/032020).
- PEÑA, A., O. RATHMANN, 2014: Atmospheric stability-dependent infinite wind-farm models and the wake-decay coefficient. – *Wind Energy* **17**, 1269–1285, DOI: [10.1002/we.1632](https://doi.org/10.1002/we.1632).
- PEÑA, A., O. RATHMANN, 2014: Atmospheric stability-dependent infinite wind-farm models and the wake-decay coefficient. – *Wind Energy* **17**, 1269–1285.
- PLATIS, A., S.K. SIEDERSLEBEN, J. BANGE, A. LAMPERT, K. BÄRFUSS, R. HANKERS, B. CAÑADILLAS, R. FOREMAN, J. SCHULZ-STELLENFLETH, B. DJATH, OTHERS, 2018: First in situ evidence of wakes in the far field behind offshore wind farms. – *Scientific reports* **8**, 2163.
- PLATIS, A., M. HUNDHAUSEN, S.K. SIEDERSLEBEN, A. LAMPERT, K. BÄRFUSS, J. SCHULZ-STELLENFLETH, B. DJATH, S. EMEIS, T. NEUMANN, B. CAÑADILLAS, J. BANGE, in review: Evaluation of a simple analytical model for offshore wind farm wake recovery by in-situ data and WRF simulations. – *Wind Energy*, in review.
- POND, S., S. SMITH, P. HAMBLIN, R. BURLING, 1966: Spectra of velocity and temperature fluctuations in the atmospheric boundary layer over the sea. – *J. Atmos. Sci.* **23**, 376–386.
- PORTÉ-AGEL, F., Y.T. WU, C.H. CHEN, 2013: A numerical study of the effects of wind direction on turbine wakes and power losses in a large wind farm. – *Energies* **6**, 5297–5313.
- PORTÉ-AGEL, F., H. LU, Y.T. WU, 2014: Interaction between large wind farms and the atmospheric boundary layer. – *Procedia Iutam* **10**, 307–318.
- PORTÉ-AGEL, F., M. BASTANKHAH, S. SHAMSODDIN, 2020: Wind-turbine and wind-farm flows: A review. – *Bound.-Layer Meteor.* **174**, 1–59.
- PORTER, D.F., J.J. CASSANO, M.C. SERREZE, 2011: Analysis of the Arctic atmospheric energy budget in WRF: A comparison with reanalyses and satellite observations. – *J. Geophysical Res. Atmos.* **116**, published online. DOI: [10.1029/2011JD016622](https://doi.org/10.1029/2011JD016622).
- PROSPATHOPOULOS, J., P. CHAVIAROPOULOS, 2013: Numerical simulation of offshore wind farm clusters. – In: European Wind Energy Association, Conference proceedings.
- PRYOR, S., R. BARTHELMIE, A. HAHMANN, T. SHEPHERD, P. VOLKER, 2018: Downstream effects from contemporary wind turbine deployments. – *J. Phys. Conference Series* **1037**, 072010. IOP Publishing.
- RAJEWSKI, D.A., E.S. TAKLE, J.K. LUNDQUIST, S. ONCLEY, J.H. PRUEGER, T.W. HORST, M.E. RHODES, R. PFEIFFER, J.L. HATFIELD, K.K. SPOTH, OTHERS, 2013: Crop wind energy experiment (CWEX): observations of surface-layer, boundary layer, and mesoscale interactions with a wind farm. – *Bull. Amer. Meteor. Soc.* **94**, 655–672.
- RAJEWSKI, D.A., E.S. TAKLE, J.K. LUNDQUIST, J.H. PRUEGER, R.L. PFEIFFER, J.L. HATFIELD, K.K. SPOTH, R.K. DOORENBOS, 2014: Changes in fluxes of heat, H<sub>2</sub>O, and CO<sub>2</sub> caused by a large wind farm. – *Agricult. Forest Meteor.* **194**, 175–187.
- ROHRIG, K., V. BERKHOUT, D. CALLIES, M. DURSTEWITZ, S. FAULSTICH, B. HAHN, M. JUNG, L. PAUSCHER, A. SEIBEL, M. SHAN, OTHERS, 2019: Powering the 21st century by wind energy-options, facts, figures. – *Appl. Phys. Rev.* **6**, 031303.
- ROY, S.B., J.J. TRAITTEUR, 2010: Impacts of wind farms on surface air temperatures. – *Proceedings of the National Academy of Sciences* **107**, 17899–17904.
- SATHE, A., 2010: Atmospheric stability and wind profile climatology over the north Sea-Case study at Egmond aan Zee. – *Proceedings of the conference torque*, 1–10.
- SCHNEEMANN, J., A. ROTT, M. DÖRENKÄMPER, G. STEINFELD, M. KÜHN, 2019: Cluster wakes impact on a far distant offshore wind farm’s power. – *Wind Energy Sci. Discuss.*, published online. DOI: [10.5194/wes-2019-39](https://doi.org/10.5194/wes-2019-39).
- SIEDERSLEBEN, S.K., 2019: Numerical analysis of offshore wind farm wakes and their impact on the marine boundary layer. – PhD thesis, Universität zu Köln.
- SIEDERSLEBEN, S.K., A. PLATIS, J.K. LUNDQUIST, A. LAMPERT, K. BÄRFUSS, B. CAÑADILLAS, B. DJATH, J. SCHULZ-STELLENFLETH, J. BANGE, T. NEUMANN, OTHERS, 2018a: Evaluation of a wind farm parametrization for mesoscale atmospheric flow models with aircraft measurements. – *Meteorol. Z.* **27**, 401–415.
- SIEDERSLEBEN, S.K., J.K. LUNDQUIST, A. PLATIS, J. BANGE, K. BÄRFUSS, A. LAMPERT, B. CAÑADILLAS, T. NEUMANN, S. EMEIS, 2018b: Micrometeorological impacts of offshore wind farms as seen in observations and simulations. – *Env. Res. Lett.*, published online, <https://iopscience.iop.org/article/10.1088/1748-9326/a6ea0b/pdf>.
- SIEDERSLEBEN, S.K., A. PLATIS, J.K. LUNDQUIST, B. DJATH, A. LAMPERT, K. BÄRFUSS, B. CAÑADILLAS, J. SCHULZ-

- STELLENFLETH, J. BANGE, T. NEUMANN, S. EMEIS, 2020: Turbulent kinetic energy over large offshore wind farms observed and simulated by the mesoscale model WRF (3.8.1). – *Geosci. Model Develop.* **13**, 249–268, DOI: [10.5194/gmd-13-249-2020](https://doi.org/10.5194/gmd-13-249-2020).
- SMEDMAN, A.S., U. HÖGSTRÖM, H. BERGSTRÖM, 1996: Low level jets – a decisive factor for off-shore wind energy siting in the baltic sea. – *Wind Engineering* **20**, 137–147.
- SMEDMAN, A.S., H. BERGSTRÖM, B. GRISOGONO, 1997: Evolution of stable internal boundary layers over a cold sea. – *J. Geophys. Res. Oceans* **102**, 1091–1099.
- SMITH, R.B., 2010: Gravity wave effects on wind farm efficiency. – *Wind Energy* **13**, 449–458.
- STULL, R.B., 2012: An introduction to boundary layer meteorology, volume 13. – Springer Science & Business Media.
- TRABUCCHI, D., G. STEINFELD, D. BASTINE, J.J. TRUJILLO, J. SCHNEEMANN, M. KÜHN, 2015: Study of wake meandering by means of fixed point lidar measurements: Spectral analysis of line-of-sight wind component. – *J. Phys. Conference Series* **625**, 012016.
- TRENBERTH, K.E., J.M. CARON, D.P. STEPANIAK, 2001: The atmospheric energy budget and implications for surface fluxes and ocean heat transports. – *Climate Dyn.* **17**, 259–276, DOI: [10.1007/PL00007927](https://doi.org/10.1007/PL00007927).
- TULLOCH, R., K.S. SMITH, 2009: Quasigeostrophic turbulence with explicit surface dynamics: Application to the atmospheric energy spectrum. – *J. Atmos. Sci.* **66**, 450–467.
- VAUTARD, R., F. THAIS, I. TOBIN, F.M. BRÉON, J.G.D. DE LAVERGNE, A. COLETTE, P. YIOU, P.M. RUTI, 2014: Regional climate model simulations indicate limited climatic impacts by operational and planned european wind farms. – *Nature communications* **5**, 3196.
- VEERS, P., K. DYKES, E. LANTZ, S. BARTH, C.L. BOTTASSO, O. CARLSON, A. CLIFTON, J. GREEN, P. GREEN, H. HOLTINEN, OTHERS, 2019: Grand challenges in the science of wind energy. – *Science* **366**, eaau2027, DOI: [10.1126/science.aau2027](https://doi.org/10.1126/science.aau2027).
- VERHOEF, A., M. PORTABELLA, A. STOFFELEN, H. HERSBACH, 2008: CMOD5. n-the CMOD5 GMF for neutral winds. – Technical Report SAF/OSI/CDOP/KNMI/TEC/TN/3, 165, KNMI, De Bilt, Netherlands.
- VERMEER, L., J.N. SØRENSEN, A. CRESPO, 2003: Wind turbine wake aerodynamics. – *Prog. Aerospace Sci.* **39**, 467–510.
- VOLKER, P., J. BADGER, A.N. HAHMANN, S. OTT, 2015: The Explicit Wake Parametrisation v1.0: A wind farm parametrisation in the mesoscale model WRF. – *Geosci. Model Develop.* **8**, 3715–3731.
- WANG, C., R.G. PRINN, 2011: Potential climatic impacts and reliability of large-scale offshore wind farms. – *Env. Res. Lett.* **6**, 025101.
- WESTERHELLWEG, A., B. CANADILLAS, A. BEEKEN, T. NEUMANN, 2010: One year of LiDAR measurements at FINO1-platform: Comparison and verification to met-mast data. – In: 10th German Wind Energy Conference, Bremen, 18–19.
- WIKLE, C.K., R.F. MILLIFF, W.G. LARGE, 1999: Surface wind variability on spatial scales from 1 to 1000 km observed during TOGA COARE. – *J. Atmos. Sci.* **56**, 2222–2231.
- WU, Y.T., F. PORTÉ-AGEL, 2012: Atmospheric turbulence effects on wind-turbine wakes: An LES study. – *Energies* **5**, 5340–5362.
- XIA, G., M.C. CERVARICH, S.B. ROY, L. ZHOU, J.R. MINDER, P.A. JIMENEZ, J.M. FREEDMAN, 2017: Simulating impacts of real-world wind farms on land surface temperature using the WRF model: Validation with observations. – *Mon. Wea. Rev.* **145**, 4813–4836.
- XU, Y., L.L. FU, R. TULLOCH, 2011: The global characteristics of the wavenumber spectrum of ocean surface wind. – *J. Phys. Oceanography* **41**, 1576–1582.
- ZHOU, L., Y. TIAN, S.B. ROY, C. THORNCROFT, L.F. BOSART, Y. HU, 2012: Impacts of wind farms on land surface temperature. – *Nature Climate Change* **2**, 539.



Article

## Using Satellite SAR to Characterize the Wind Flow around Offshore Wind Farms

Charlotte Bay Hasager <sup>1,\*</sup>, Pauline Vincent <sup>2,†</sup>, Jake Badger <sup>1,†</sup>, Merete Badger <sup>1,†</sup>,  
Alessandro Di Bella <sup>1,†</sup>, Alfredo Peña <sup>1,†</sup>, Romain Husson <sup>2,†</sup> and Patrick J. H. Volker <sup>1,†</sup>

<sup>1</sup> Technical University of Denmark, Wind Energy Department, Frederiksborgvej 399, Roskilde 4000, Denmark; E-Mails: [REDACTED]@dtu.dk (J.B.); [REDACTED]@dtu.dk (M.B.); [REDACTED]@dtu.dk (A.D.B.); [REDACTED]@dtu.dk (A.P.); [REDACTED]l@dtu.dk (P.J.H.V.)

<sup>2</sup> Collecte Localisation Satellites, Avenue La Pérouse, Bâtiment le Ponant, Plouzané 29280, France; E-Mails: [REDACTED]@cls.fr (P.V.); [REDACTED]@cls.fr (R.H.)

† These authors contributed equally to this work.

\* Author to whom correspondence should be addressed; E-Mail: [REDACTED]@dtu.dk;  
Tel.: +[REDACTED] Fax: +[REDACTED].

Academic Editors: Vincenzo Dovi and Antonella Battaglini

Received: 16 April 2015 / Accepted: 1 June 2015 / Published: 5 June 2015

---

**Abstract:** Offshore wind farm cluster effects between neighboring wind farms increase rapidly with the large-scale deployment of offshore wind turbines. The wind farm wakes observed from Synthetic Aperture Radar (SAR) are sometimes visible and atmospheric and wake models are here shown to convincingly reproduce the observed very long wind farm wakes. The present study mainly focuses on wind farm wake climatology based on Envisat ASAR. The available SAR data archive covering the large offshore wind farms at Horns Rev has been used for geo-located wind farm wake studies. However, the results are difficult to interpret due to mainly three issues: the limited number of samples per wind directional sector, the coastal wind speed gradient, and oceanic bathymetry effects in the SAR retrievals. A new methodology is developed and presented. This method overcomes effectively the first issue and in most cases, but not always, the second. In the new method all wind field maps are rotated such that the wind is always coming from the same relative direction. By applying the new method to the SAR wind maps, mesoscale and microscale model wake aggregated wind-fields results are compared. The SAR-based findings strongly support the model results at Horns Rev 1.

**Keywords:** wind farm wake; offshore; satellite; SAR; remote sensing

---

## 1. Introduction

In the Northern European Seas offshore wind farms are planned as clusters. The wind farm wake from one wind farm thus has the potential to influence the power production at neighboring wind farms. The expected wake loss due to wind farm cluster effects is investigated in the present study. The wind farm wake cluster effects are strongly dependent upon the atmospheric conditions. These vary spatially and temporally. One remote sensing method for observing ocean surface winds is satellite Synthetic Aperture Radar (SAR). The advantage of SAR is that a large area is observed and several wind farms are covered. The derived wind map from SAR provides a snapshot of the wind field during a few seconds at the time of acquisition.

In the satellite SAR data archives covering the North Sea, thousands of wind turbines are visible as white dots in calm conditions. For low wind speed the backscatter signal over the ocean is low and the images appear dark while hard targets such as wind turbines and ships provide high backscatter and the objects appear very bright. During windy conditions wind farm wakes are sometimes visible as dark elongated areas downwind of a wind farm while the surrounding seas appear brighter. This is a result of the differences in wind speed with reduced winds downwind of large operating wind farms. The intensity of backscatter of microwave electromagnetic radiation from the ocean surface is a non-linear function of the wind speed over the ocean. The physical relationship is due to the capillary and short gravity waves formed at the ocean surface by the wind. For higher wind speeds the backscatter is higher.

Previous wind farm wake studies based on SAR from ERS-1/-2, Envisat, RADARSAT-1/-2, TerraSAR-X and airborne SAR show great variability in wind farm wakes [1–4]. This reflects the natural variability in atmospheric conditions at the micro- and mesoscale. Wind farm wakes are often not clearly visible in the SAR archive data. This may be explained by wind turbines out of operation or presence of oceanic features, e.g., bathymetry, currents, surfactants. However, the great variability in the wind field is most likely a major cause.

In order to show that wind farm wakes are detectable from SAR, we present in this study one case based on RADARSAT-2 ScanSAR Wide. This scene is a good example where ideal conditions for wake analysis occur and the coverage is just right for capturing 10 large offshore wind farms located in the southern North Sea. We compare the instantaneous SAR-based wind farm wakes to micro- and mesoscale wake model results.

For the rest of our SAR wind archive, we wish to find out if wakes can be detected even if they are not so clearly visible. We first use a simple method which has some disadvantages. Next we apply the aggregated method to overcome some of these disadvantages.

This is the first time that a suitable number of SAR scenes covering several large operating wind farms have become available [5]. The present study focuses on the wind farm wake climatology using many overlapping SAR scenes. The wide-swath-mode (WSM) products from the Advanced SAR (ASAR) on-board Envisat are selected. This data source is sampled routinely so there are many more samples but with less spatial detail (original resolution 150 m) than those used in previous studies

(of the order 5 to 30 m spatial resolution) where the data are rare and infrequent and only sampled upon request [1–4]. It is questionable whether wake effects can be detected from Envisat ASAR WSM data as we cannot always visually see the wind farm wakes. However, we hypothesize that the combination of many satellite samples will show an aggregated effect of the wind farm wakes on the mean wind climate in the area. The SAR-based wind farm wake climatology results therefore can be used to validate wake model results. The wind farm wake climatology can be modelled by micro- and mesoscale models but perfect agreement cannot be expected between SAR and wake model results. This is due to the different nature of data with SAR based on the sea surface while wake models operate around wind turbine hub-height.

The main topic of the study is on the potential of using SAR for characterization of wind flow around offshore wind farms. Our mission is to find out how to best utilize SAR for wake mapping. Three modes of investigation are considered: (1) Wind flow observed at 10 offshore farms with wind farm wakes concurrent in one SAR scene; (2) Wind flow observed at two wind farms concurrent and wind farm wakes average value based on 7 to 30 SAR scenes; (3) Wind flow observed at one wind farm at a time and the aggregated wind farm wake based on 100 to 800 SAR scenes. Basic information on the three modes of investigation is listed in Table 1. The advantages and limitations of each investigation mode in regard to wind farm wake model comparison are provided. Selected wake model results are presented as demonstration for each of the modes. Presenting the three modes in such an order clearly shows the evolution of wake studies using SAR.

**Table 1.** SAR source, number of wind farms covered in the method, number of SAR scenes used in each method for wake identification based on no averaging, geo-located SAR wind field averaging and rotated SAR wind field averaging. The spatial resolution of the wind fields are given. The Section in this paper where each mode is presented is also indicated.

Satellite Data	Number of Wind Farms	Number of SAR Scenes	Averaging	Analysis Type	Resolution (km)	Section
RADARSAT-2	10	1	None	Qualitative	1	3
Envisat ASAR	2	7–30	Geo-located	Quantitative	1	4
Envisat ASAR	1	100–800	Rotated	Quantitative	1	5

The structure of the paper includes in Section 2 a description of the study site, satellite data and the two wake models used. In Section 3 the results from the case study based on RADARSAT-2 and the results from two wake models are presented and discussed. Section 4 presents the Envisat SAR-based wind farm wake climatology based on simple averaging of the wind fields at Horns Rev 1 and 2 wind farms and comparison to results from one wake model. Section 5 gives introduction to the new methodology developed in which the wind field maps are rotated such that the wind is always coming from the same relative direction. The Envisat SAR-based results from the new methodology as well as wake model results from two models are presented and Envisat SAR-based results from four other wind farms are presented. In Section 6 is the discussion of results. Conclusions are given in Section 7.

## 2. Study Site, Satellite SAR and Wake Modelling

### 2.1. Study Site

Wind flow around the wind farms in the southern part of the North Sea is investigated. The wind farms studied are listed in Table 2 and the location of most of the wind farms is shown in Figure 1. Those not shown in Figure 1 are the Alpha ventus wind farm located in the German North Sea and Horns Rev 1 and 2 located in the Danish North Sea. The information in Table 2 includes the year of start of operation and key data on the wind turbines and area covered.

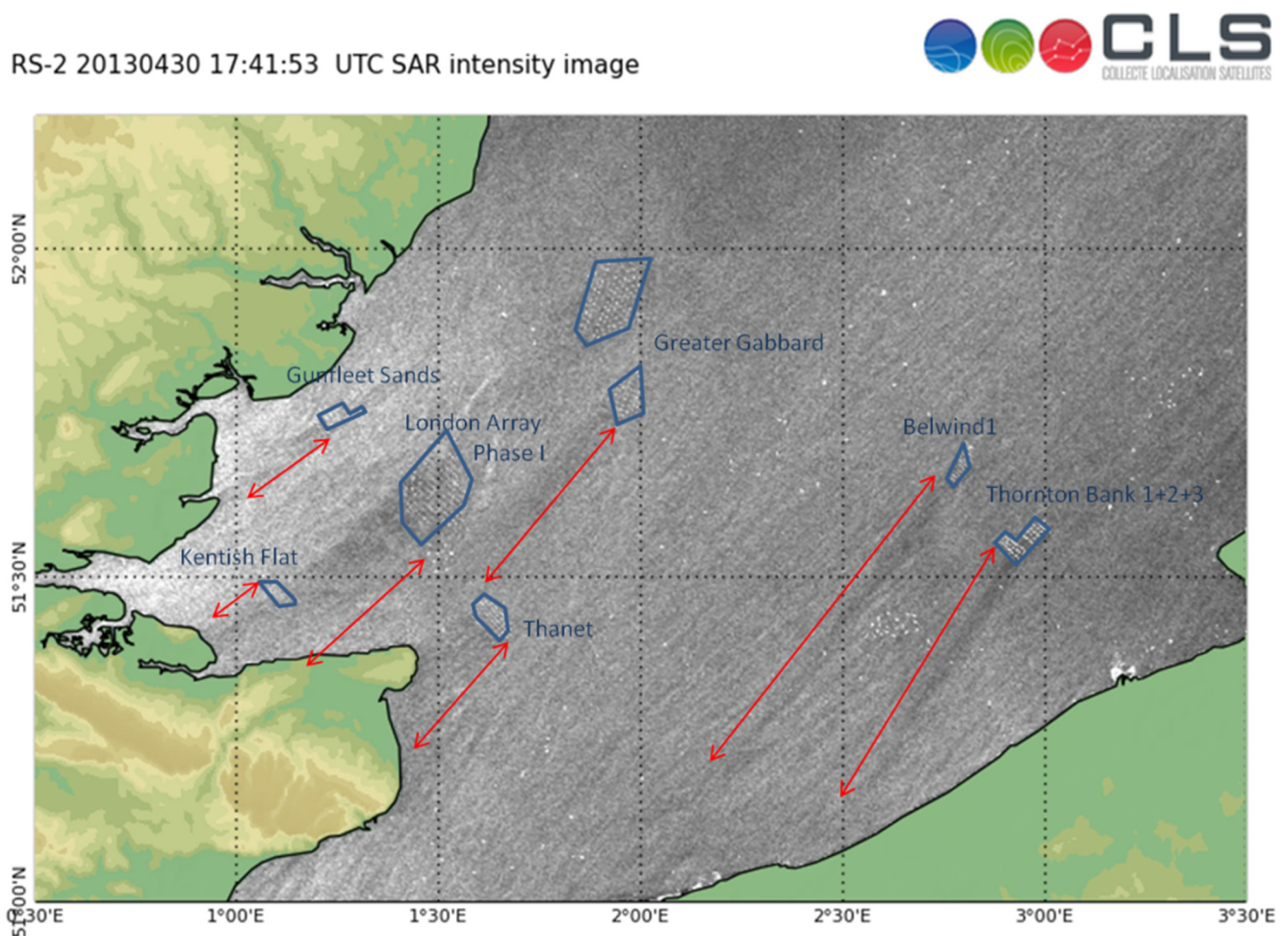


**Figure 1.** RADARSAT-2 intensity map of the southern North Sea observed 30 April 2013 at 17:41 UTC. The blue lines outline wind farms and the red arrows the wind farm wake.

**Table 2.** Wind farm info: Country, start year of operation, approximated latitude and longitude, number and size of turbines, wind park capacity and area covered.

Wind Farm	Nationality	Year	Latitude (°)	Longitude (°)	Number of Turbines	Turbine Size (MW)	Park (MW)	Area (km <sup>2</sup> )
Alpha ventus	Germany	2009	54.010	6.606	12	5	60	4
Belwind 1	Belgium	2010	51.670	2.802	55	3	165	13
Greater Gabbard	United Kingdom	2012	51.883	1.935	140	3.6	504	146
Gunfleet Sands 1 + 2I	United Kingdom	2010	51.730	1.229	48	3.6	172.8	16
Horns Rev 1	Denmark	2002	55.486	7.840	80	2.0	160	21
Horns Rev 2	Denmark	2009	55.600	7.582	91	2.3	209.3	33
Kentish Flats	United Kingdom	2005	51.460	1.093	30	3	90	10
London Array Phase 1	United Kingdom	2012	51.626	1.495	175	3.6	630	100
Thanet	United Kingdom	2010	51.430	1.633	100	3	300	35
Thornton Bank 1	Belgium	2009	51.544	2.938	6	6	30	1
Thornton Bank 2	Belgium	2012	51.556	2.969	30	6.15	184.5	12
Thornton Bank 3	Belgium	2013	51.540	2.921	18	6.15	110.7	7

## 2.2. Satellite SAR

SAR data from RADARSAT-2 and Envisat ASAR WSM are used. From RADARSAT-2 only one scene is investigated. It is ScanSAR Wide in VV polarization. The wind field retrieval requires input information about the wind direction. From the RADARSAT-2 image the wake direction has been estimated as  $40^\circ$  and using this input for wind direction, wind speed has been retrieved using CMOD-IFR2 [6]. It is the equivalent neutral wind (ENW) at the height 10 m. The calculated wind speed is presented in Figure 2a. The original ScanSAR Wide product has spatial resolution 100 m. The spatial resolution is reduced to approx. 1 km in connection with the processing of wind fields. This is performed to eliminate effects of random noise and long-period waves.

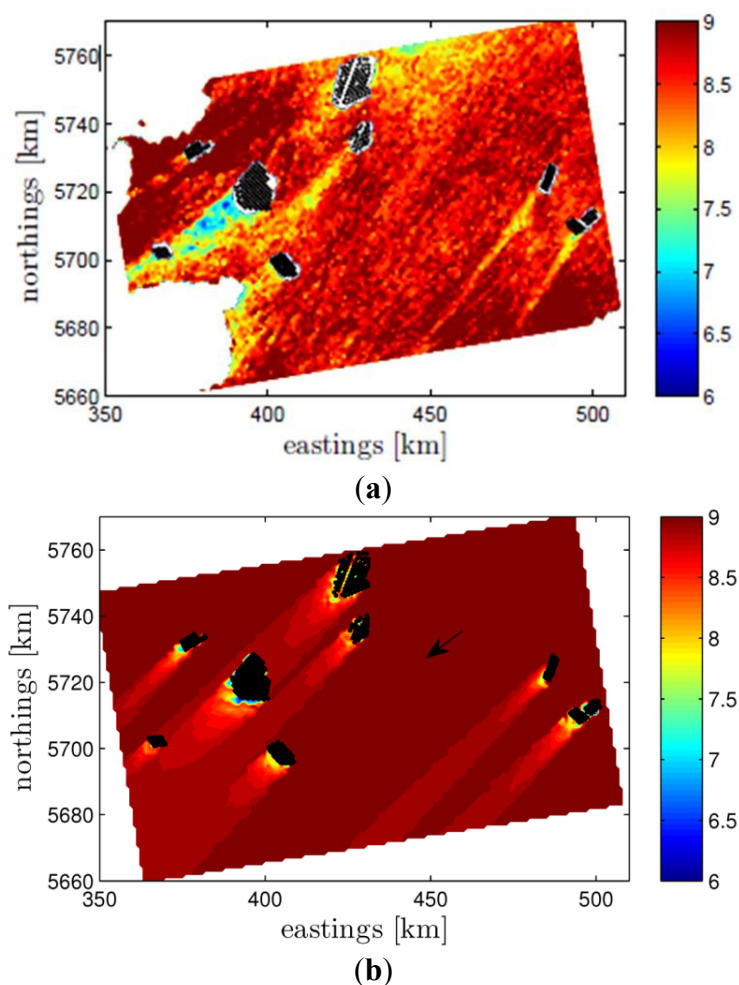


**Figure 2.** (a) Satellite 10-m SAR wind retrieval observed 30 April 2013 at 17:41 UTC and (b) modified PARK wake results at 70 m for the wind farms in the UK and Belgium. The wind direction used for the modeling is indicated with the black arrow.

The Envisat ASAR data were processed to wind fields as part of the project NORSEWInD [5]. The wind field retrieval gives the ENW at the height 10 m. For processing of large image archives, it is desirable to use wind direction information from an atmospheric model. In this case the wind directions were obtained from the European Centre for Medium-Range Weather Forecasts (ECMWF) model and interpolated spatially to match the higher resolution of the satellite data. Further details about the

SAR-wind processing chain, which was setup by Collecte Localisation Satellites (CLS), are given in [5]. The original WSM product has spatial resolution 150 m. The spatial resolution is to approx. 1 km in the wind field.

### 2.3. Wake Modelling with PARK and WRF

A modified version of the PARK wake model [7], also implemented in the Wind Atlas Analysis and Application Program (WAsP) [8], is here used for wake calculations. The main difference between this modified version and that in WAsP is that the former does not take into account the effects of the “ground reflecting back wakes” and so it only takes into account the shading rotors both directly upstream and sideways. The PARK wake model is based on the wake deficit suggested by [9], who derived a mass-conservation-like equation for the velocity immediately before a turbine  $u_2$ , which is affected by a wake:

$$u_2 = u_1 \left[ 1 - \frac{a}{\left(1 + \frac{k_w x}{r_r}\right)^2} \right] \quad (1)$$

where  $u_1$  is the upstream wind speed,  $a$  the induction factor which is a function of the thrust coefficient ( $C_t$ ),  $k_w$  the wake decay coefficient,  $x$  the downstream distance and  $r_r$  the turbine’s rotor radius. The square of the total wake deficit is estimated as the sum of the square of all contributing wake deficits. We implemented the model in a Matlab script. This allows us to compute wake deficits at any given point. The wake model can be compared to satellite derived wind maps which contains information over a large area. We use  $k_w = 0.03$  for the wake computations.

The Weather Research and Forecasting (WRF) mesoscale model [10] is also used for wake modelling. The advantage of WRF is that the dynamic synoptic flow is considered. The computational cost is much higher than that for the PARK model though.

Mesoscale models have been developed to simulate the atmosphere flow over areas on the order of hundreds of kilometers. Due to their low horizontal resolution unresolved processes, such as turbulence and turbine induced wakes have to be parametrized. In common wind farm parametrisations [11–16] the local turbine interaction is not accounted for, instead the wind speed reduction within the wind farm is obtained from the interaction between the turbine containing grid-cells. The Explicit Wake Parametrisation (EWP) is used for the parametrization of wind farms [16]. In this approach a grid-cell averaged deceleration is applied, which accounts for the unresolved wake expansion with the turbine containing grid-cell. Turbulence Kinetic Energy (TKE) is provided by the Planetary Boundary Layer (PBL) scheme from a changed vertical shear in horizontal velocity in the wake. The EWP scheme is independent of the PBL scheme, although, a second order scheme is recommended.

We use WRF V3.4 with the selected mesoscale model physics parametrizations: PBL [17] (MYNN 2.5), convection [18] (Domain I and II), micro-physics [19], long-wave radiation [20], shortwave radiation [21], land-surface [22] and Nudging of U and V in the outer domain (outside PBL). The number of grid cells in the innermost domain were 427 times 304 in the  $x$  and  $y$  direction, with a 2 km grid-spacing. We used [16] for the wind farm parametrization.

The model outer domain is driven by ERA-Interim reanalysis data [23] and two nests are inside. The horizontal resolution for the three domains is 18 km, 6 km and 2 km, respectively. The inner nest is run twice, without and with the wind farm parametrization. The number of vertical layers is set to 60. The second mass level is at around 12 m above sea level and it is used for the comparison to the satellite images.

### 3. Case Study Based on RADARSAT-2

The case study is based on the RADARSAT-2 scene from 30th April 2013 at 17:41 UTC (selected from around 30 images with visible wakes). Figure 1 shows the backscatter intensity map. The wind is from the northeast and the map shows elongated long dark areas downwind of most of the wind farms. These are the wind farm wakes. The approximate extent of the individual wind farm wakes is outlined in the image. The longest is at Belwind around 55 km long while at Thornton Bank it is 45 km, London Array 15 km and Thanet 14 km. At Kentish Flat the wind farm wake is only 10 km long but it is probably passing over the coast and inland in the UK. This cannot be mapped from SAR. It should be noticed that all wakes are very straight and with similar direction. In the intensity map the wind turbines can be seen as small regularly spaced white dots while numerous ships can be noted in irregular spatial pattern. Some large ships show higher backscatter than the turbines.

The retrieved wind speed map is shown in Figure 2a. The wind speed in the northern part of the map is slightly lower than in the southern part. Yet the synoptic flow appears to be fairly homogenous across the entire area. Coastal speed up is seen particular near the UK and Belgium coastlines. The wind speed varies around  $8.5\text{--}9.5\text{ m}\cdot\text{s}^{-1}$  in areas not affected by wind farms while the wind farm wake regions show lower wind speed around  $7\text{--}8\text{ m}\cdot\text{s}^{-1}$  dependent upon location. The wake at London Array is very wide and it appears to influence Kentish Flat at this time. The wake at London Array has a large wake deficit with much lower wind speeds in the wake than in the upwind free stream region. Wake meandering is not pronounced.

The case illustrates a rather unique situation. Firstly because we observe wakes in the satellite image for all wind farms distributed in a large area of the North Sea (all farms in the area show clear speed deficits). Secondly the wind speed and wind the direction do not seem to largely change over such an extended area. Therefore we are able to simulate with the PARK wake model all wind farms at the same time (assuming the same background inflow conditions for all of them). The background wind speed is about  $9\text{ m}\cdot\text{s}^{-1}$  and direction  $40^\circ$ . We use these two values at 70 m as inflow conditions for the wake modeling.

Figure 2a shows the SAR wind retrieval at 10 m, where most of the variability seems to come from the wake deficits downstream the wind farms, and the wake model results at 70 m in Figure 2b. In this case, we do not extrapolate the satellite background conditions up to 70 m or extrapolate downwards the model results to 10 m as we assume the same wind speed at around hub height when performing the wake simulations. The comparison is only qualitative.

Interestingly, the speed deficits seem to be rather well reproduced by the wake model, extending in most cases nearly as long as the wakes observed in the SAR image.

The WRF wake model with the EWP wind farm scheme is also used for simulation. We include only London Array, Greater Gabbard, Thanet, Belwind1 and Thornton Bank which are the largest wind farms.



The domain is rotated around  $10^\circ$  at the wind farm location. The simulation is from the 24 April to 1 May 2013. The velocity deficit at 10 m at 30 April 2013 at 18:00 UTC is shown in Figure 3. We have chosen to plot the velocity deficit since due to the gradients in the background velocity the wake is not visible in the velocity field from the wind farm simulation.

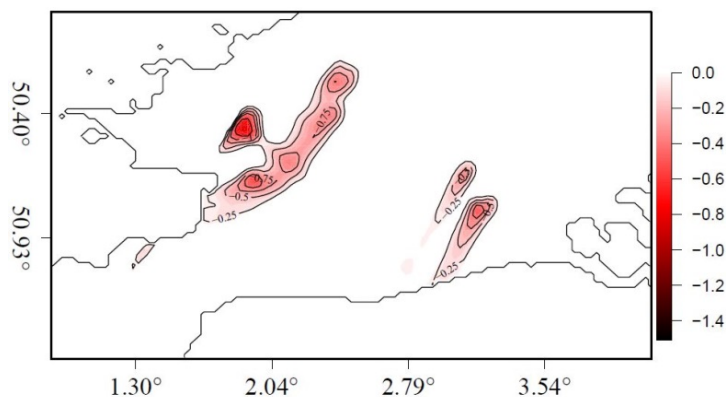


**Figure 3.** WRF wake model results on velocity deficit in  $\text{m}\cdot\text{s}^{-1}$  at 10 m AMSL at 30 April 2013 at 18:00 UTC at the wind farms London Array, Greater Gabbard, Thanet, Belwind 1 and Thornton Bank.

The WRF modelled wakes at the UK wind farms are oriented slightly more towards the eastern direction than the satellite wakes. The orientations differ by around  $10^\circ$ . For the Belgian wind farms we find that the wakes are well aligned in the SAR and WRF results. Regarding the wake extension behind the wind farms we find for the London Array short wakes both in SAR and WRF while the wakes at the Thanet and Greater Gabbard wind farms are considerably longer both in SAR and WRF. However WRF shows even longer wakes than SAR for Greater Gabbard and Thanet. The extension of wakes at the Belgian wind farms compare well in SAR and WRF.

From WRF it is found that the synoptic conditions two hours before 18:00 UTC show intensified pressure gradients, leading to increased wind speeds near the English coast from  $4 \text{ m}\cdot\text{s}^{-1}$  to higher winds in the order of  $10 \text{ m}\cdot\text{s}^{-1}$ . The Greater Gabbard and Thanet wind farms experienced high wind speeds for two hours at 18:00 UTC. The wind speeds started to increase at the London Array only shortly before 18:00 UTC. It might be that the increasing model wind speeds are for some hours out of phase, which would explain the longer wakes behind Greater Gabbard and Thanet wind farms in WRF compared to SAR.

In summary, the wind farm wakes from several wind farms are visually compared between SAR and WRF simulations of the velocity deficit obtained without wind farm and with wind farms using the EWP scheme. The wind farm wake directions and extension of wake are found to compare well despite that mesoscale features, such as that resulting from unsteady flow conditions, are noted in the wind farm wakes in the WRF simulation. We cannot expect the WRF simulations to match the observed velocity and wind direction in SAR satellite data perfectly. The PARK model results do not include unsteady flow but even so the PARK model results have overall good agreement to SAR. This can in part be attributed to the rather unique atmospheric conditions at the time of this SAR acquisition. The results for single events only can be used qualitatively. For a quantitative comparison statistics over longer periods are needed.

#### 4. Wind Farm Wake Climatology Geo-Located Wind Maps

The case in Section 3 was selected based on clear visual observation of wind farm wakes at several wind farms within one satellite SAR image. However, we would like to study the behavior of the wind farm wake in a climatological fashion and investigate whether this can be performed using our Envisat ASAR WSM data set. We select to study the Horns Rev 1 and 2 wind farms for which we have 356 SAR scenes in total for the period of dual wind farm operation from September 2009 to the termination of the Envisat mission in March 2012.

As the wake behavior is highly dependent on the inflow wind conditions, in particular the wind direction, we perform the study for 12 directional sectors based on the ECMWF model wind direction used to retrieve the SAR winds. The SAR scenes are first binned according to the wind directions extracted for a single point near the two wind farms. The data set is then filtered such that only scenes with wind speeds in the range  $4\text{--}14\text{ m}\cdot\text{s}^{-1}$  at the same point are included (total of 241). This is the range where wind farm wakes are expected to be most detectable. At lower wind speeds, the turbines are not operating and at higher wind speeds, wind penetration through the wind farms is expected. For each directional bin, we extract the inflow conditions from a point upstream of the wind farms for every SAR scene in the bin. The reference points are located on two circles circumscribing the wind farms Horns Rev 1 and Horns Rev 2 with radii of 7.5 km and 10 km, respectively, as shown in Figure 4. To get representative inflow conditions, the satellite winds are extracted within a radius of 10 km for Horns Rev 2 and a radius of 7.5 km for Horns Rev 1 wind farm.

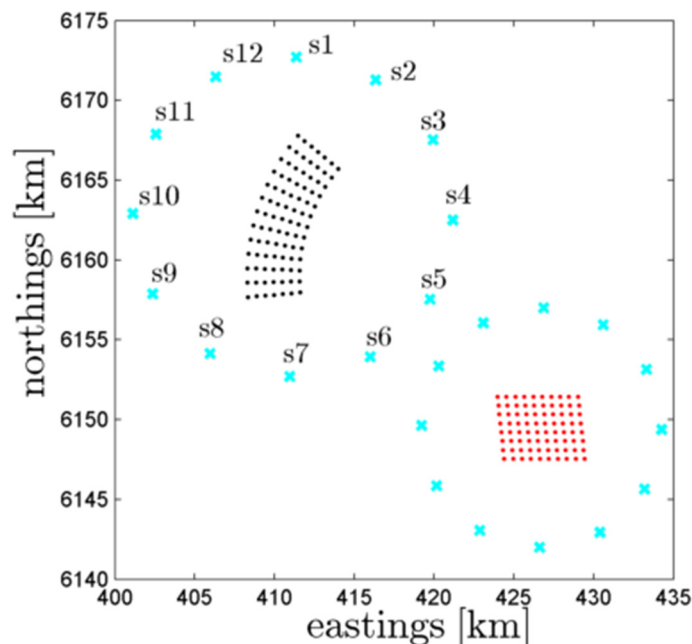


**Figure 4.** Horns Rev 1 and 2 wind farms in red and black markers, respectively. The locations of the points where the inflow conditions are extracted per sector (cyan markers) is also illustrated.

We perform simulations using the modified PARK model at all positions on the satellite grid and for all the inflow conditions per sector. The point around the wind farms where we extract the inflow conditions is selected based on the sector analyzed, e.g., we use the point north of Horns Rev 2 when

performing simulations for Sector 1. In the following subsections we perform qualitative comparisons of the 10 m wind speed SAR retrievals with the results of the wake model per sector at the same height. Both results (wind speed maps) show the average wind speed per sector. We choose to show results for Sector 2 and 3 in Figure 5 because the coastal wind speed gradient and wind farm wakes can be seen in these results even though relatively few data are available. Table 3 shows the number of samples per sector. The inflow wind speed for Sector 2 and Sector 3 is  $8.52$  and  $8.25$   $\text{m}\cdot\text{s}^{-1}$  in average with a standard deviation of  $3.50$  and  $2.55$   $\text{m}\cdot\text{s}^{-1}$ , respectively (these are the values at 70 m height). This means that simulations are performed for a rather wide range of wind speeds. These two examples have several overlapping images and several features can be noted such as the coastal wind speed gradient and wind farm wake.

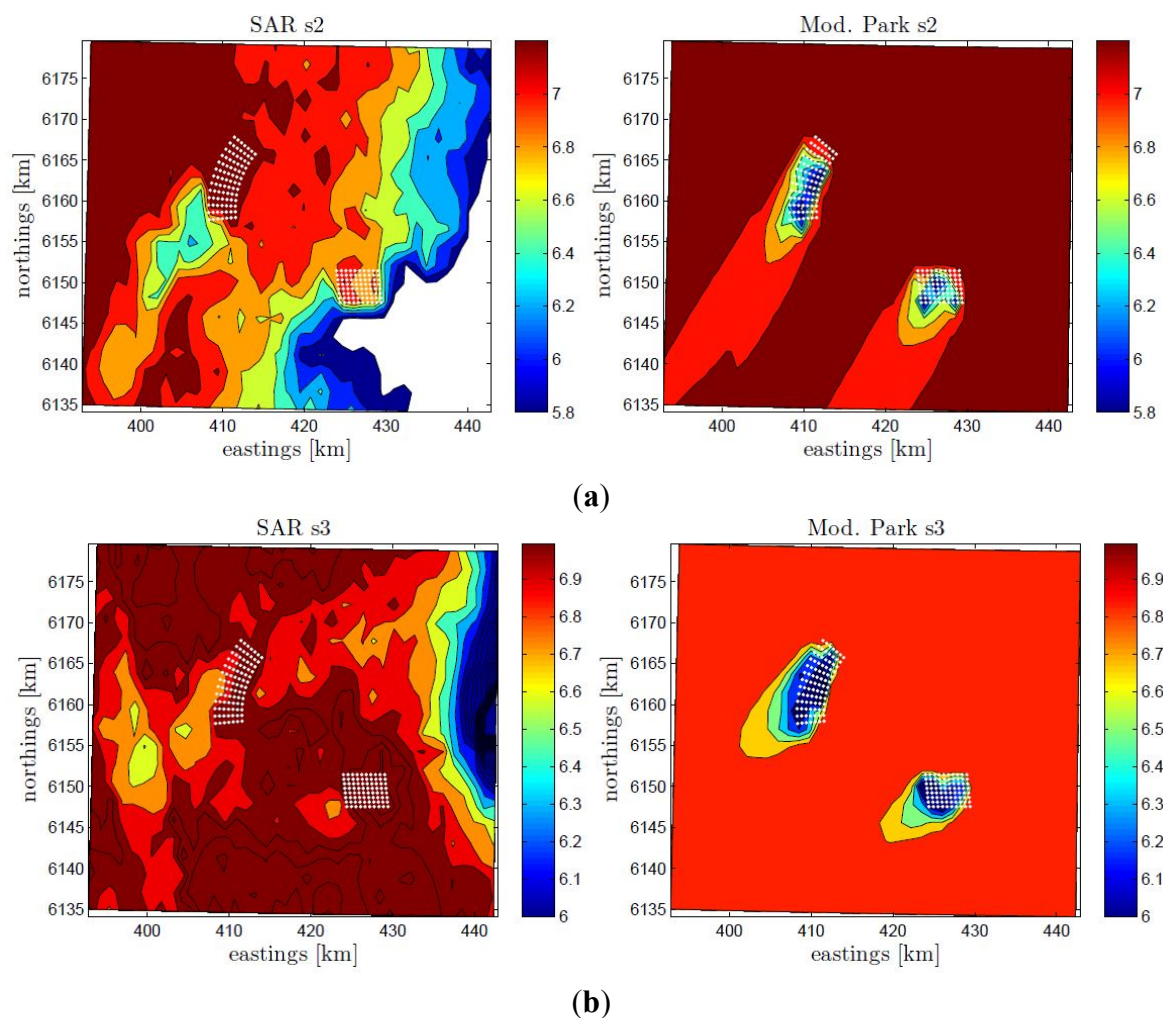


**Figure 5.** Average wind speed based on satellite SAR (left) and modified PARG wake model results (right) at 10 m height for the Horns Rev wind farm area for winds from Sector 2 (a) and Sector 3 (b). The color bar indicates wind speed in  $\text{m}\cdot\text{s}^{-1}$ .

**Table 3.** Number of Envisat ASAR samples available per wind directional bin at Horns Rev.

Sector	1	2	3	4	5	6	7	8	9	10	11	12	Total
Samples	13	7	12	16	24	21	22	28	22	30	20	26	241

For Sector 2 there are seven available SAR images for the analysis and the average wind speed is  $7.2 \text{ m}\cdot\text{s}^{-1}$ . It is surprising we do not observe wakes from the Horns Rev 1 wind farm (Figure 5a). This might be simply because of the high horizontal wind speed gradient approaching the coast, which is located east of Horns Rev 1. There is a clear wake spreading towards the southwest direction of the Horns Rev 2 wind farm. The PARK model results show clear wakes spreading southwest of both wind farms.

For Sector 3 twelve SAR images are available for the analysis (west of Horns Rev 2 the number is reduced to 10) with an average wind speed of  $7.0 \text{ m}\cdot\text{s}^{-1}$ . This case shows agreement in terms of the location of the areas where wakes are observed in both the SAR and the PARK wake model at both wind farms (Figure 5b).

The number of samples per sector varies from 7 to 30 within the 12 sectors. The overall agreement between SAR and the wake model is variable. For some sectors (1 and 7) the bathymetry effect at Horns Rev appears to be particularly strong as previously noted by [1]. This results in the lack of wake effects in the mean wind speed maps from SAR due to the interaction of bathymetry and currents, which sometimes leaves a detectable “imprint” at the sea surface. This effect is most visible when winds blow directly from the north or south at Horns Rev (not shown here).

Another reason for the difficulties to systematically observe wakes of offshore wind farms from satellite-derived wind products are inhomogeneous flow. Although the ocean surface is rather homogenous, e.g., when compared to the land surface, the effects of the horizontal wind variability diminish those of the wakes. In the particular case of the Horns Rev area, there is a systematic wind speed gradient near the coast also obstructing the observation of wakes, particularly for easterly and westerly winds. These effects are not taken into account in the PARK modeling. The coastal gradient in wind speed is noticeable in the SAR images in Figure 5.

Finally it can be noted that the distribution of wind maps into direction sectors is performed with some uncertainty. The model wind directions used to drive the SAR wind speed retrieval are not always accurate. The accuracy of the wind direction input could be improved through implementation of higher-resolution regional model simulations, e.g., from WRF. Another option is to detect the wind direction directly from wake signatures whenever they are visible in the images. The distribution of satellite scenes into the 12 sectors is based on information extracted at a single point. Local turning of the wind is possible but not accounted for in the analysis. Each directional bin is  $30^\circ$  wide thus the peak wake directions are expected to vary within this and it will diffuse the observed aggregated wake features. Due to the nature of the SAR images (specifically its number) and due to other phenomena causing spatial variability in the wind speed (like coastal gradients and mesoscale phenomena), it seems not suitable to perform the SAR wake analysis per sectors this wide.

## 5. Wind Farm Wake Climatology Based on Rotation of Wind Maps

In this section a new approach to analyze SAR-derived wind farm wakes in a climatological way is presented. The method aligns (rotates) all SAR wind field samples such that the wind farm wakes are overlapping before the wake deficit is calculated. This increases the number of samples considerably compared to the method presented in Section 3. Furthermore the  $30^\circ$  wind direction bins used previously give diffuse results whereas in the new method wind directions alignment at  $1^\circ$  resolution is used.

The new method is based on extracting wind speeds along points inscribed by circles centered on the wind farm under analysis. While the method was developed for analysis of wakes in SAR scenes, here it is also applied to the WRF simulations as a way to validate the mesoscale simulated wakes.

### 5.1. Description of the Method

For each SAR scene (or WRF simulated wind field) the wind speeds as a function of compass direction  $\theta$  are extracted along 3 concentric circles centered on the wind farm. The radii depend on the wind farm in question, and are given in Table 3.

Figure 6 gives an example of the circles centered on the Horns Rev 2 wind farm. The wind fields are based on SAR data (1 km). It can be difficult to determine a wake by eye. For each SAR scene the wind speeds along these 3 circles are extracted and stored as  $U_i(\theta_j)$ , where  $U_i$  is the wind speed for circle  $i$  where  $i = 1, 2, 3$  and  $\theta_j$  is the compass direction relative to the center of the wind farm.  $\theta_j$  steps through values from 0 to 359° with a 1 degree increment. The number of scenes used for the analysis depends on the wind farm under examination. The number is given in Table 4. The WRF model is run for all SAR scenes from Horns Rev 1 and 2, and results are extracted in a similar way from the WRF simulation results as for the SAR wind fields. The SAR results are valid at 10 m AMSL while WRF model results are available at 14 m AMSL.

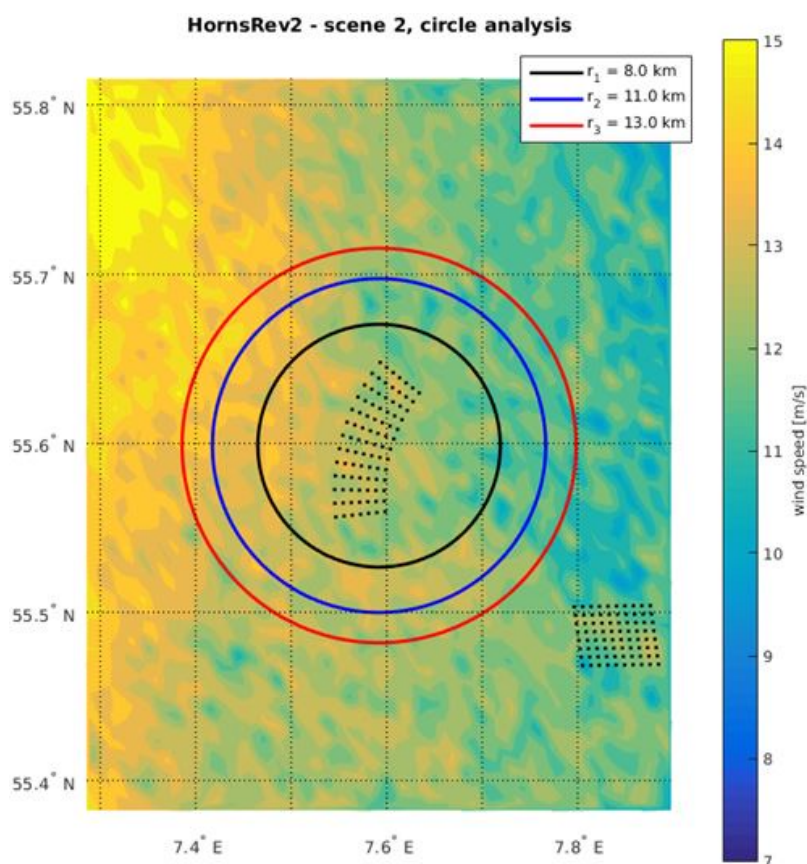


**Figure 6.** Example of the circles centered on Horn Rev 2 wind farm. The radii are 8, 11 and 3 km.

**Table 4.** The radii of the three concentric circles for the different wind farms and the number of Envisat ASAR scenes used for the analysis.

Wind Farm	$r_1$ (km)	$r_2$ (km)	$r_3$ (km)	$N_{scenes}$
Alpha ventus	5	10	15	245
Belwind1	6	11	15	97
Gunfleet Sands 1 + 2	4	5	6	153
Horns Rev 1	6	10	13	835
Horns Rev 2	8	12	15	303
Thanet	7	9	11	128

First the sum of wind speeds is calculated:

$$S_i^N(\theta_j) = \frac{1}{N_{scene}} \sum_{k=1}^{N_{scene}} (U_i(\theta_j))_k \quad (2)$$

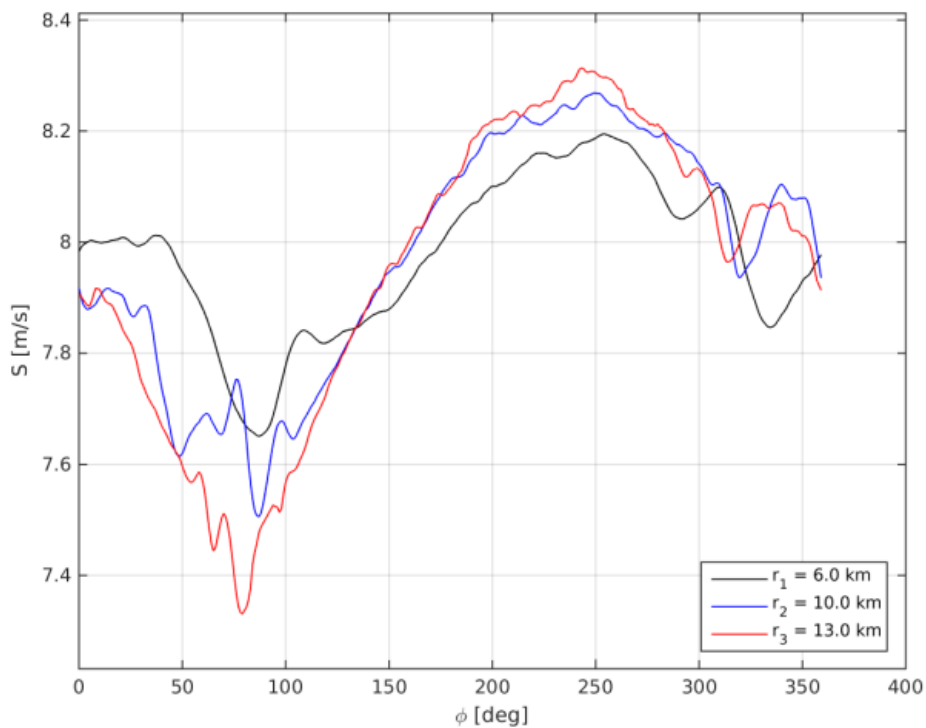
where  $k$  is the scene number, and  $N_{scene}$  is the total number of scenes. Figure 7a shows  $S^N$  plotted against  $\theta$ , for the Horns Rev 1 wind farm. We see from this plot how the mean wind speed depends on  $\theta$ . This can be explained in terms of the gradient of the mean wind in the vicinity of the coastline. We call this the coastal gradient. Similar results of  $S^N$  based on WRF are shown in Figure 7b. The coastal gradient in wind speed at Horns Rev 1 shows lowest values around  $80^\circ$ – $110^\circ$  (east), where the inscribed circles are closest to the coastline, and highest around  $250^\circ$  (west), where the inscribed circles are furthest from the coastline both in SAR and WRF. SAR shows a direction closer to  $80^\circ$  while WRF shows a direction closer to  $110^\circ$ . It is expected that there is an east-west gradient at Horns Rev as reported in [24]. For the eastern sector SAR shows higher wind speed values at the inner radius (6 km) and progressively lower values at outer radii (10 and 13 km) (nearer to the coastline). For the western sector SAR shows slightly higher wind speed at outer radii (further from the coastline).

WRF shows a similar pattern as SAR for the western sector but shows a reverse order in the wind speed at the eastern sector at different radii. This most likely is due to the simulated wake effects of Horns Rev 2 influencing the results at the 13 km radius around  $260^\circ$ – $350^\circ$ . This is supported by examining the results from using WRF without simulating the wind farms, shown in Figure 8. In this plot a very much cleaner signature of the coastal gradient is seen. The next step is to rotate the direction frame of reference for each SAR scene by using each scene's reported wind direction,  $\theta_k$ , to give a new direction reference,  $\varphi$ . In the new direction reference frame for each scene  $\varphi = 0^\circ$  is aligned in the upwind direction and thus one may expect that the wake direction is in the region of  $\varphi = 180^\circ$ . Now we can determine the wind speeds on the inscribed circles as a function of  $\varphi_j$  instead of  $\theta_j$  by using:

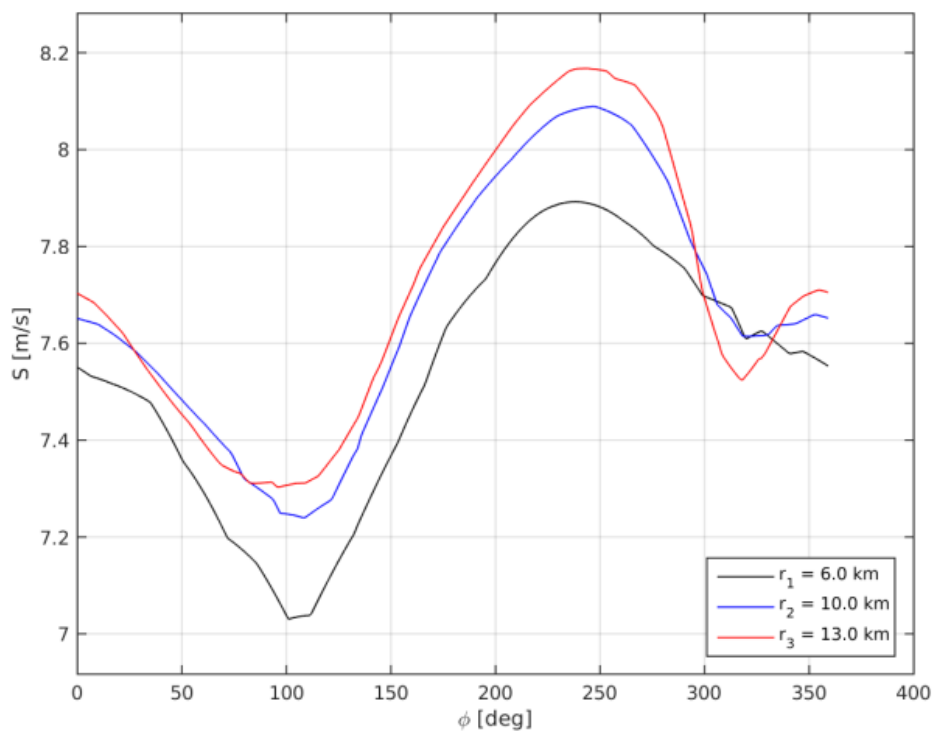
$$\varphi_j = \theta_j - \theta_k \quad (3)$$

The sum of wind speeds for all scenes is now calculated with respect to the new direction frame, *i.e.*:

$$S_i^R(\varphi_j) = \frac{1}{N_{scene}} \sum_{k=1}^{N_{scene}} (U_i(\varphi_j))_k \quad (4)$$



(a)



(b)

**Figure 7.** Horns Rev 1 wind speed summations without rotation (mean wind speed gradient) ( $S$ ) based on SAR (a) and WRF (b).

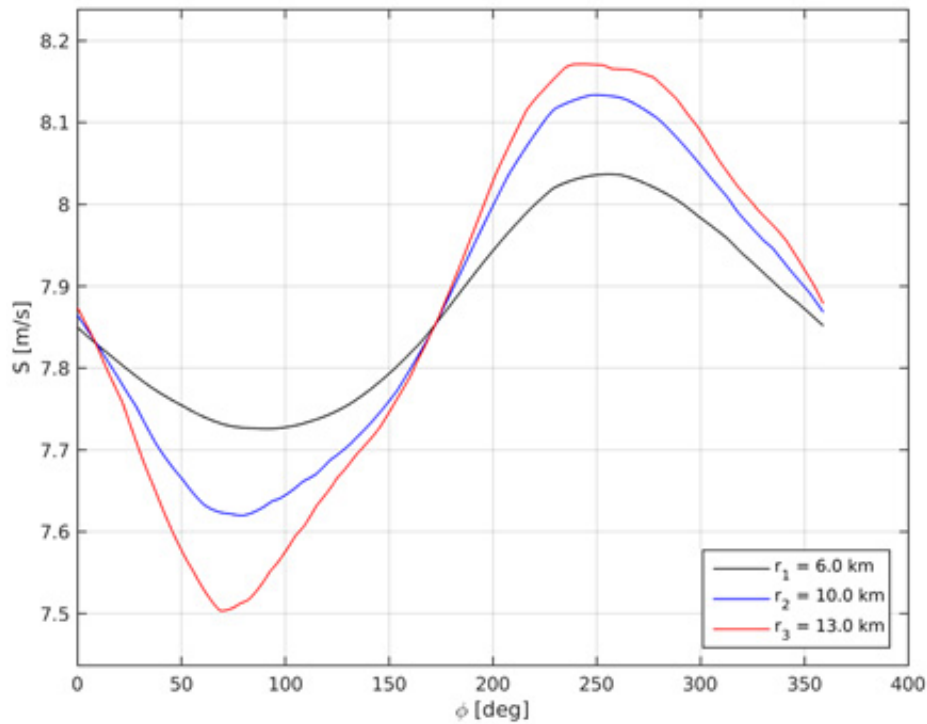


**Figure 8.** Horns Rev 1 wind speed summations without rotation ( $S$ ) based on WRF without wind farms, so showing only the coastal wind speed gradient.

Figure 9a shows  $S^R$  plotted against  $\phi$ , for the Horns Rev 1 wind farm. The corresponding results of  $S^R$  based on WRF simulations are shown in Figure 9b. Please note that the differences between the top and bottom panels are due to the individual rotation of each scene prior to averaging and not the result of a single rotation by one angle. The similarity in form between SAR and WRF for the rotated maps ( $S_{rot}$ ) is very good with low wind speeds showing at all radii at around  $\phi = 180^\circ$ . The inner radius shows more wake effect than outer radii. The SAR derived results are less smooth than those from WRF because the SAR scenes capture variability at smaller scales, due to the heterogeneity of the wind field, than is modelled by WRF.

To further reveal the wind farm wake from the heterogeneous wind field around the wind farm a method to calculate a wake wind speed deficit is employed. It is based on calculating a local perturbation of the wind speed on each SAR scene based on the side lobe wind speeds. The side lobe wind speeds are used at the directions  $\phi + \Delta\phi_i$  and  $\phi - \Delta\phi_i$ . For the smallest radius  $\Delta\phi_1 = 90^\circ$ , this means that the side lobe wind speed is from the left and right of the wind farm, at a distance of  $r_1$  from the farm center. For the other radii, the side lobes have the same distance,  $r_1$ , from the line aligned with the wind direction and passing through the center of the wind farm, thus:

$$\Delta\phi_i = \arcsin\left(\frac{r_1}{r_i}\right) \tag{5}$$

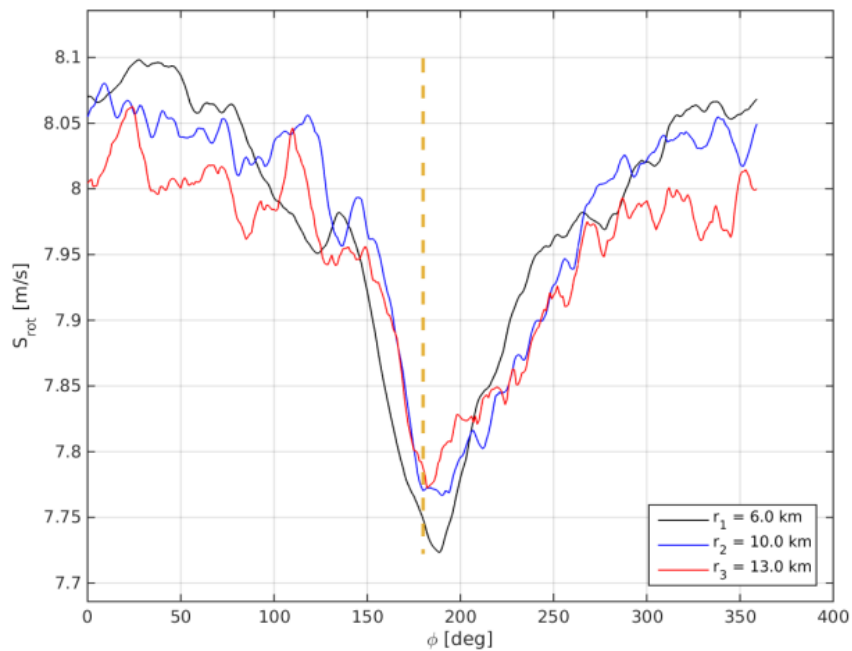
The wake wind speed deficit is defined by:

$$U_i^D = U_i(\phi_j) - \frac{1}{2}(U_i(\phi_j + \Delta\phi_i) + U_i(\phi_j - \Delta\phi_i)) \tag{6}$$

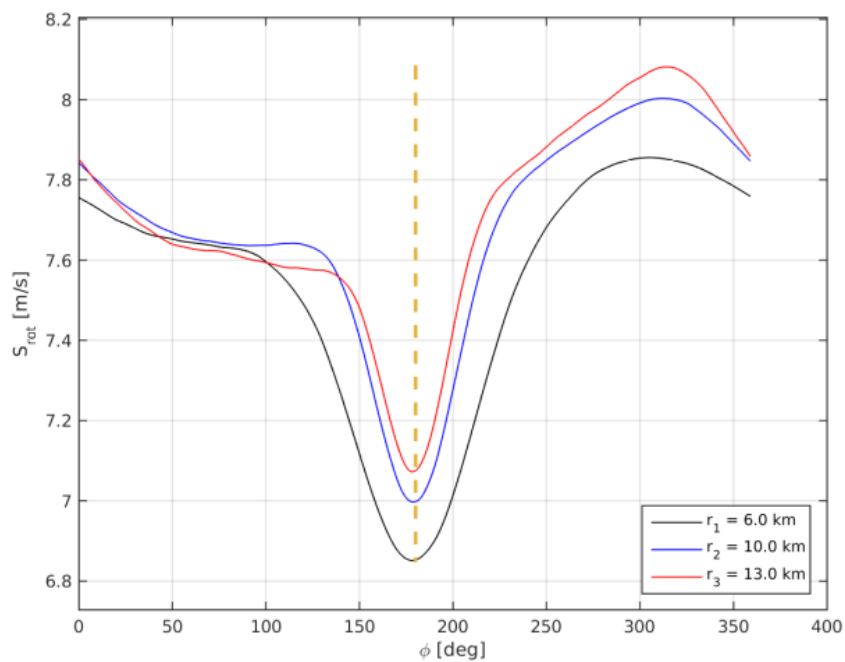
and the wake wind speed deficit summation is:



$$S_i^D(\varphi_j) = \frac{1}{N_{scene}} \sum_{k=1}^{N_{scene}} (U_i^D(\varphi_j))_k \tag{7}$$



(a)



(b)

**Figure 9.** Horns Rev 1 wind speed summations with rotation ( $S_{rot}$ ) based on SAR (a) and WRF (b).

Figure 10 shows  $S^D$  plotted *versus*  $\varphi$  for the Horn Rev 1 wind farm for SAR and WRF. In Figure 10 the wake wind speed deficit results based on SAR wind fields and WRF simulations both show the deepest wake at the inner radius and gradual recovery at the outer radii. Both SAR and WRF results show a speed up along the sides of the wake. This shows most clearly at the inner radius but is also noted

at the outer radii. The SAR results on wake deficit compares well to the WRF results at Horns Rev 1, however the magnitude of the SAR derived wake is weaker compared to the WRF wakes. It should be noted that the WRF simulations here are one embodiment of WRF simulations and that broader variability in WRF-generated wakes would be generated by other choices of PBL schemes, vertical resolution and approach for representing the wind farm effect.

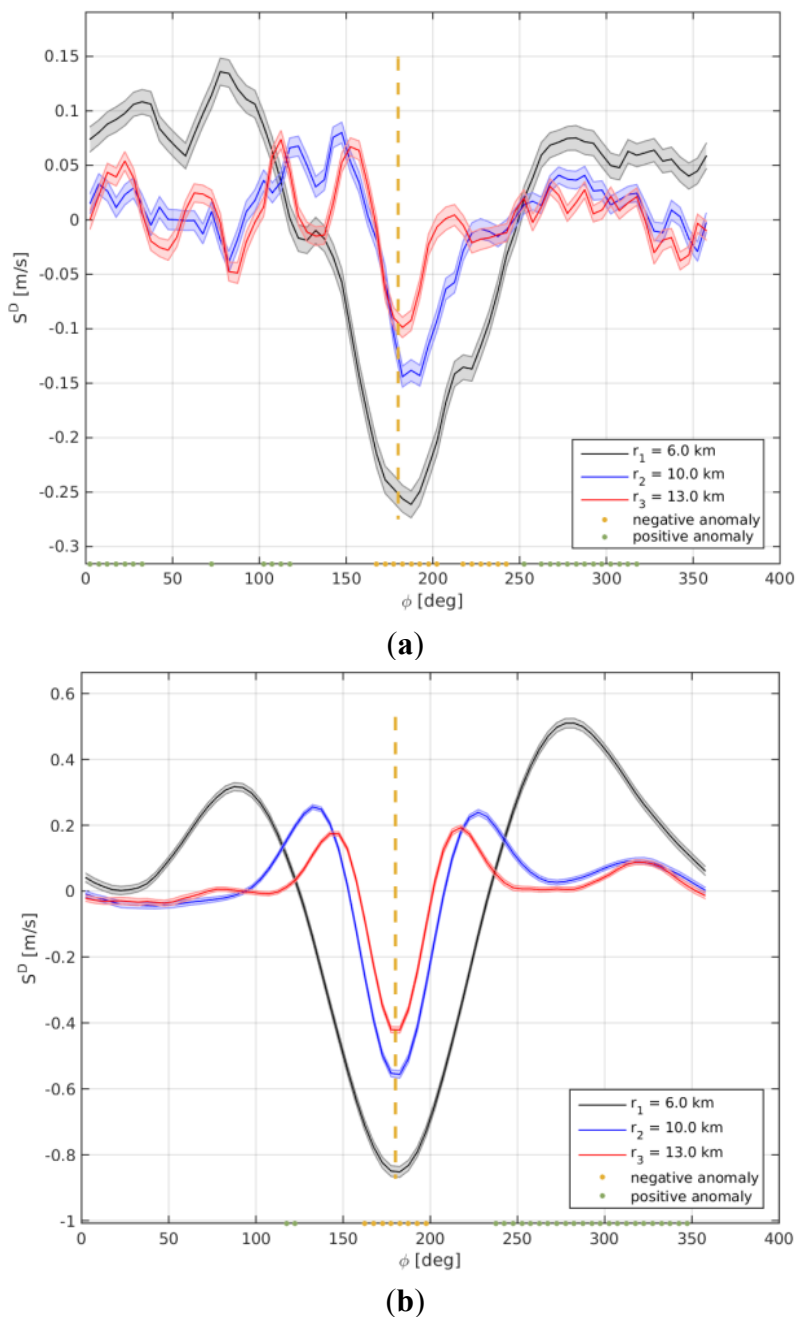
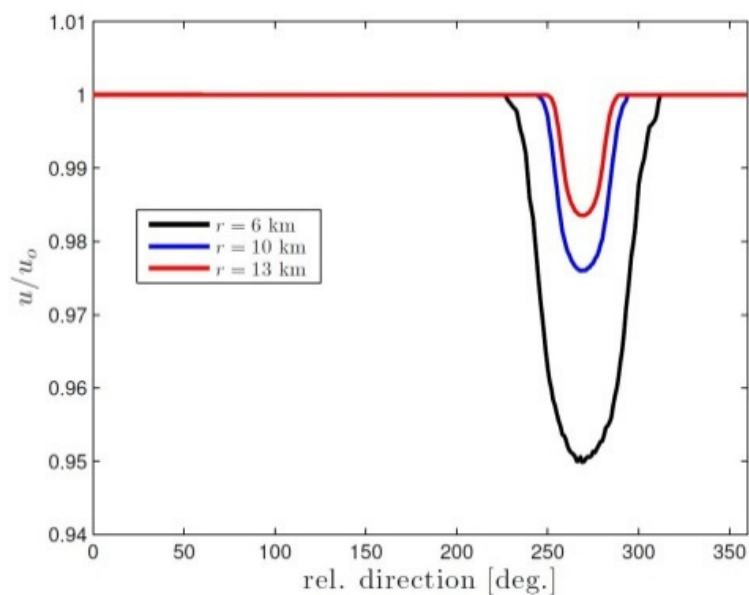


**Figure 10.** Horns Rev 1 wake wind speed deficit ( $S^D$ ) based on SAR (a) and WRF (b). The shaded areas in SAR indicate the standard error.

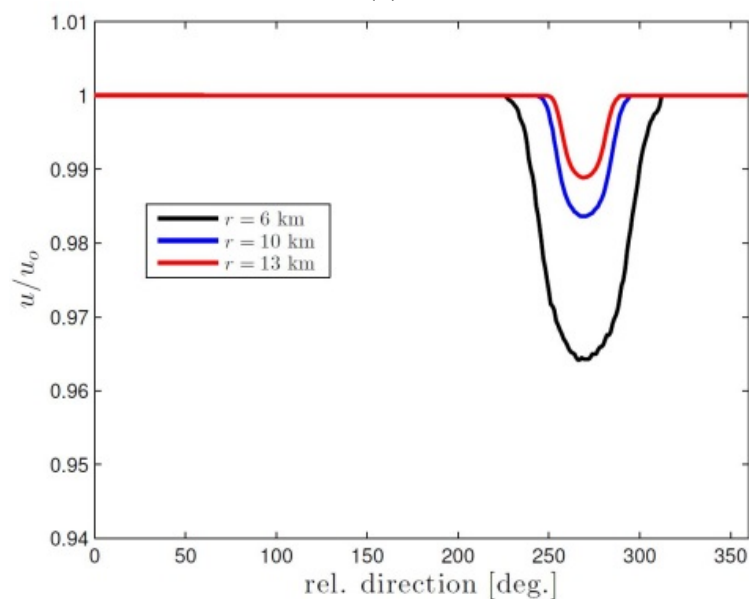
### 5.2. PARK Model Results

The PARK model is used to simulate 855 cases (a few more cases than used above but the results are expected to be comparable) at Horns Rev 1. The SAR wind time series at 10 m is used as input,

the winds are extrapolated to 70 m and the wake is modeled at that height and finally the winds are extrapolated downwards to 10 m again. The extrapolation is done using the logarithmic wind profile assuming a constant roughness length of 0.0002 m. The results are presented at 10 m. Three wake decay coefficients are used. The three wake decay coefficients are: 0.03, 0.04 and 0.05. The wake decay coefficient 0.04 is often used offshore while the lower and higher values are used in case of more stable or unstable cases. The results are rotated and averaged and the results are shown in Figure 11. The coastal gradient is not accounted for in the PARK model results. In case the coastal gradient should be added in the PARK model this could either be from SAR or from WRF, but it has not been attempted in the current study. The results are comparable to the wake wind speed deficit ( $S^D$ ) results.



(a)



(b)

Figure 11. Cont.

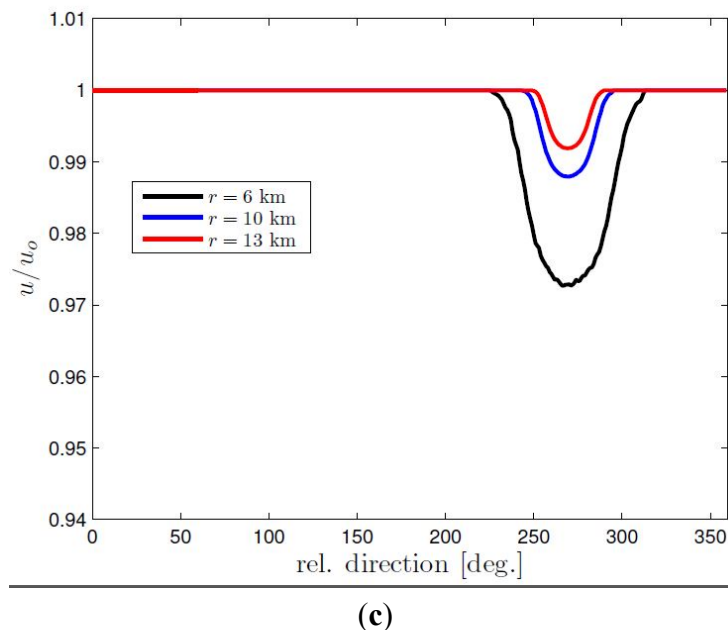


**Figure 11.** Wake results from the modified PARK model at Horns Rev 1 using wake decay coefficients (a) 0.03; (b) 0.04 and (c) 0.05.

Figure 11 shows the systematic variation in wake with deeper wakes at the inner radius and progressively weaker wakes further from the wind farm. The wake decay coefficient of 0.03 gives much deeper wakes than for the higher wake decay coefficients, in particular for the inner radius. The shape of the wake compares well to Figure 10 from SAR and WRF.

### 5.3. Horns Rev 2 Results

Horns Rev 2 is located further offshore than Horns Rev 1 thus similar directional but lower wind speed gradients are expected. The mean wind speed gradient results based on SAR and WRF for Horns Rev 2 are presented in Figure 12a,b. The coastal wind speed gradient observations in SAR at Horns Rev 2 (Figure 12a) show a very peaked and significant minimum around  $110^\circ$  corresponding to the direction of Horns Rev 1. The feature (drop of around  $0.2 \text{ m}\cdot\text{s}^{-1}$ ) is observed at all radii (8, 11 and 13 km) and is most pronounced at the outer radius. This narrow fine-scale feature is only fully observed in SAR. SAR resolves features at smaller spatial scales than the WRF simulations presented here. This minimum value might be related to the wind farm wake from Horns Rev 1. Interestingly WRF shows a broad minimum with a shift in direction between radii from  $100^\circ$  at the 8 km radius to  $110^\circ$  at the 10 km radius and  $120^\circ$  at the 13 km radius (Figure 12b). Thus the WRF simulation may in fact here capture a blend of coastal gradient and wind farm wake from Horns Rev 1. At the western sector SAR shows a peaked maximum around  $250^\circ$  and similar wind speeds at all three radii while WRF shows flatter maximum and slightly higher winds at outer radii.

Figure 12c,d shows the rotated maps ( $S_{\text{rot}}$ ) for Horns Rev 2. For SAR a minimum around  $180^\circ$  at 8 km radius is observed while at 10 km and 13 km the minima are around  $250^\circ$  and  $110^\circ$ , respectively. Only at 8 km do the WRF simulations agree with the SAR observations. The three radii at Horns Rev 2 are each located 2 km further from the wind farm center than the results for Horns Rev 1. This was necessary because the Horns Rev 2 wind farm is larger than the Horns Rev 1 wind farm. This however

means that the wind alignment between inflow conditions and the deepest wind farm wake potentially deviate relatively more at Horns Rev 2 than Horns Rev 1.

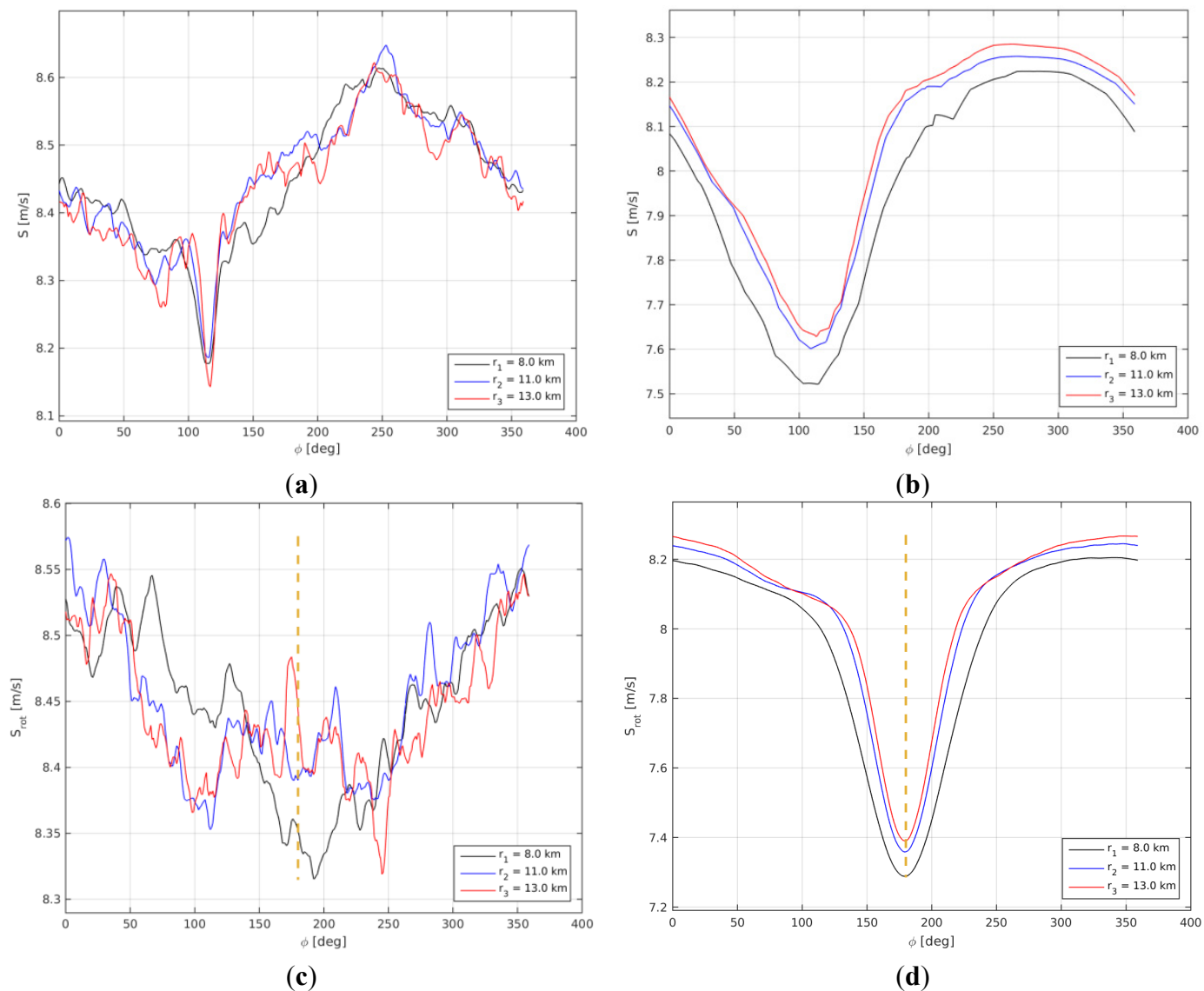


**Figure 12.** Results for Horns Rev 2. (a) wind speed summations without rotation (mean wind speed gradient) ( $S$ ) based on SAR; (b) WRF; (c) wind speed summations with rotation ( $S_{rot}$ ) based on SAR; (d) WRF.

Figure 13 shows the wake wind speed deficit ( $S^D$ ) results from SAR and WRF. The results at the inner radius compare well even though the SAR results show a broader wake than WRF. Speed up in the side lobe winds are noticed both in SAR and WRF at the inner radii and no residual wind speed gradient is noted. At the middle and outer radii WRF shows gradual decrease in the wake winds speed deficit and speed up at the sides while the SAR results are difficult to interpret. In SAR the minimum wake wind speed deficit is not observed around  $180^\circ$  but around  $100^\circ$  and  $250^\circ$ . The analysis appears not to work so well in this case, in part due to the significant minimum around  $110^\circ$  in Figure 12a. This feature may possibly be the wake feature of Horn Rev 1, which acts to contaminate the analysis, as this feature can be as strong as the Horn Rev 2 wake itself.

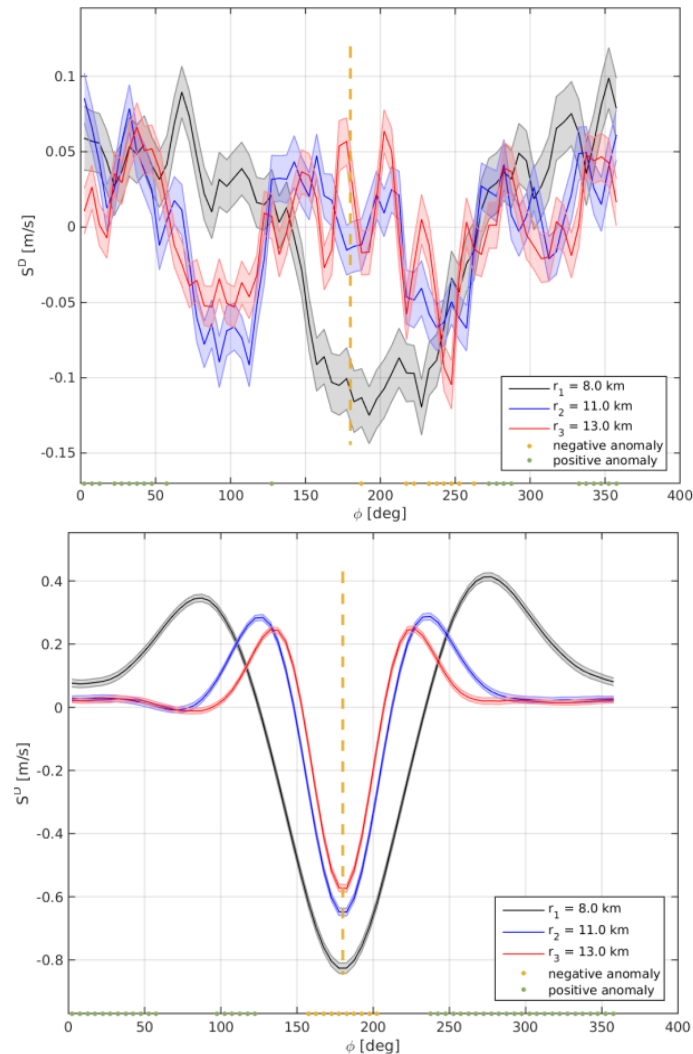


**Figure 13.** Similar to Figure 10 but for Horns Rev 2.

#### 5.4. SAR-Based Results for Six Wind Farms

Based on the available Envisat ASAR wind field archive we find it interesting to compare the observed aggregated wind farm wakes at four other wind farms in the southern North Sea using the new methodology of rotation of the wind maps. The results of the wake wind speed deficit ( $S^D$ ) are shown in Figure 14 together with the results from Horns Rev 1 and Horns Rev 2 already discussed.

It is the results for the average of the three radii (see Table 4) for each wind farm that is shown. Figure 14 shows results for six wind farms. It is noted that Gunfleet Sands 1 + 2 show the deepest wake wind speed deficit. The side lobe speed-up effects are clear. A residual wind speed gradient is not noted. For the wind speed summation ( $S$ ) (not shown) there is a weaker signature of a climatological wind speed gradient across the wind farm compared to other wind farms, this may be because the radii used are smaller.

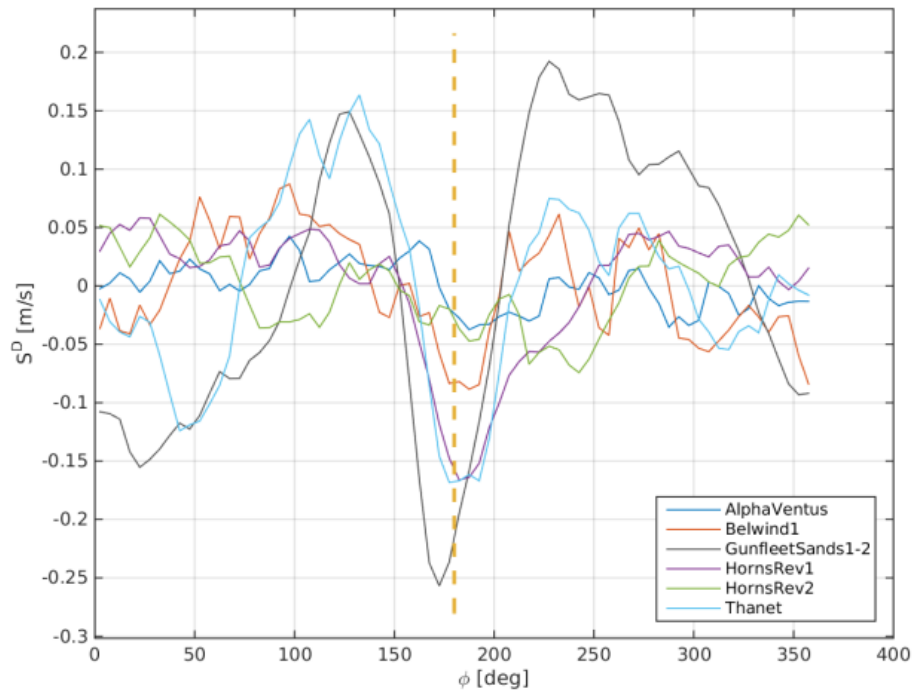


**Figure 14.** SAR-based wind farm wake observed at six wind farms, Alpha ventus, Belwind 1, Gunfleet Sands 1 + 2, Horns Rev 1, Horns Rev 2 and Thanet, showing the wake wind speed deficit ( $S^D$ ).

At the Thanet wind farm, the wake wind speed deficit results show very clear wake at around  $180^\circ$  and side lobe speed-up effects. A residual of the coastal wind speed gradient is noted. There is a feature at  $50^\circ$  with lower winds that would need further investigation.

At the Belwind 1 wind farm the wake wind speed deficit is clear but not as pronounced as for the Gunfleet Sands 1 + 2, Thanet and Horns Rev 1 results. Weak side lobe effects are observed at Belwind 1. A residual of coastal wind speed gradient is not noted in the wake wind speed deficit despite that strong coastal gradient mean wind speed gradient is found in the coastal gradient plot ( $S$ ) (not shown).

Finally, at the Alpha ventus wind farm, the smallest wind farm in terms of installed capacity and area, there is observed wake wind speed deficit at around  $180^\circ$ . The wind farm wake is not as pronounced as for the larger wind farms investigated. This is expected due to the size of the wind farm. The coastal gradient is not observed in the result but is noted in the coastal wind speed gradient ( $S$ ) (not shown).

## 6. Discussion

The very long wind farm wakes observed in the RADARSAT-2 scene have in qualitative terms successfully been modeled both by the PARK and WRF model at several wind farms in the southern North Sea. The comparison is qualitative due the different nature of data. The SAR-based results are near-instantaneous observations of the sea surface while wake model results are time-averaged results with best representation of the conditions at around hub-height. Thus we focus on the apparent wind farm wake direction and the length of the wakes in this comparison instead of the wake deficit at any given location. The SAR image has the advantage of clear visible wake features. Thus the retrieved wind field can be used to evaluate the wake model results in qualitative terms.

We are interested in developing more robust SAR-based wind farm wake data representation for the evaluation of wake models. Therefore the climatology of wind farm wake is necessary. The Envisat ASAR data of wind fields enable us to study the wind farm wake at Horns Rev 1 and 2 with the data set divided into 12 wind directional bins. The results are compared to the PARK model. Occasionally good agreement is found but due to strong coastal wind speed gradients, bathymetry effects and too few samples firm conclusions cannot be drawn.

The new method, in which the wind field maps are rotated, overcomes two of the main issues when trying to isolate the wind farm effect of the wake on the wind fields: the low number of samples and the coastal gradient. The first advantage is that the inflow wind is aligned (rotated) with  $1^\circ$  bins instead of  $30^\circ$  bins. This gives more certainty that the deepest wind farm wake are overlapping in the aggregated results. With the inflow wind speed used to normalize the winds in the wake, the wake are clearly seen but at the same time a residual of the coastal gradient is often noted, e.g., at Horns Rev 1. The clearest wind farm wake results are typically obtained using the side lobe winds for normalization, the wake wind speed deficit method ( $S^D$ ). This is not too surprising as the coastal wind speed gradients at most wind farms are significant and the circles used around the large offshore wind farms need to be at some distance. Therefore any inhomogeneity in the flow, most importantly the coastal gradient, but in fact also meandering and other atmospheric features gain importance. Also in [2] the nearby parallel transects winds along the wind farm wake were optimal for normalization, rather than the inflow winds upwind of the wind farm.

The number of samples at Horns Rev 2 is 303 while at Horns Rev 1 it is 835. So the lower number of samples at Horns Rev 2 could be one reason for the lesser clarity in data at this site when compared to Horns Rev 1. Also the influence of the Horns Rev 1 wind farm wake may hinder full interpretation at Horns Rev 2 in particular at radii far from the Horns Rev 2 wind farm. Finally it should be mentioned that the Horns Rev 1 wind farm has a geometric shape (turbine lay-out) more convenient for the proposed new methodology of analysis than that of the Horns Rev 2 wind farm. We assume that all wind turbines are in operation at all times a characteristic which may not be fulfilled.

The SAR-based aggregated wind farm wake data compare well both to the WRF simulations and the PARK model results. It is the first time that assessment of the wind farm wake climatology has been attempted based on SAR (to our knowledge) and the results are promising. The main importance of the establishment of SAR-based wake wind speed aggregated results is for the validation of wind farm wake models in the far-field wake region where other observations are extremely limited. In the future more wind farms will operate offshore thus cluster-scale wind farm wake therefore become an even more important focus area. It is suggested to continue this type of research using new SAR data from the Sentinel-1 mission.

## 7. Conclusions

The case study based on a RADARSAR-2 scene is a unique situation with fairly homogeneous flow across the southern North Sea. The observed wind farm wakes are visible in the SAR scene and thus appealing for demonstration. Both WRF and PARK reproduce the observed very long wind farm wakes convincingly regarding their direction and extent. SAR archive renders possible climatology studies.



The available Envisat ASAR data archive at Horns Rev is the most comprehensive. It has therefore been used for geo-located wind farm wake climatology studies. However the results are only occasionally clear for interpretation due to the limited number of samples per 30° sectors, the coastal wind speed gradient and oceanic bathymetry effects in SAR at Horns Rev.

The key results are based on a new methodology of rotating wind maps. By applying the new methodology to SAR-based wind fields, mesoscale model WRF and microscale model PARK results comparable aggregated wind farm wake results are obtained. The SAR-based findings strongly support the model results at Horns Rev 1. The new methodology increases the number of samples, aligns the wind direction of inflow much more accurately (1° bins) and in most cases but not always overcome the coastal wind gradient. The most convincing results are obtained for the wind wake deficit results in which the side lobe winds are used for normalization.

### Acknowledgments

Support from the European Energy Research Alliance-Design Tools for Offshore wind farm Clusters (EERA DTOC) project FP7-ENERGY-2011-1/n 282797 and satellite images from RADARSAT-2 from Data and Products © MacDonald, Dettewiler and Associates Ltd and Envisat ASAR data from the European Space Agency are acknowledged. We are thankful to the Northern Seas Wind Index Database (NORSEWIND) project for the Envisat ASAR wind field archive processed by Alexis Mouche.

### Author Contributions

Charlotte Bay Hasager coordinated the main theme of this paper and wrote the manuscript. Pauline Vincent and Romain Husson processed the RADARSAT-2 scene, identified the wind farm wakes and retrieved the wind speed. Jake Badger and Alessandro Di Bella developed the new methodology of rotating the wind maps for aggregated wake results and Alessandro Di Bella programmed and applied the methodology on Envisat ASAR wind fields and WRF model results and produced the graphics. Merete Badger prepared the Envisat ASAR wind field archive and extracted all information for the wake research. Alfredo Peña programmed the PARK model in Matlab and produced results and graphics. Patrick Volker set up the WRF model and produced the results used for wake comparison. All authors discussed the research results and commented on the manuscript. All the authors read and approved the final manuscript.

### Conflicts of Interest

The authors declare no conflict of interest.

### References

1. Christiansen, M.B.; Hasager, C.B. Wake effects of large offshore wind farms identified from satellite SAR. *Remote Sens. Environ.* **2005**, *98*, 251–268.
2. Christiansen, M.B.; Hasager, C.B. Using airborne and satellite SAR for wake mapping offshore. *Wind Energy* **2006**, *9*, 437–455.

3. Li, X.; Lehner, S. Observation of TerraSAR-X for Studies on Offshore Wind Turbine Wake in near and Far Fields. *IEEE* **2013**, *5*, 1757–1768.
4. Hasager, C.B.; Vincent, P.; Husson, R.; Mouche, A.; Badger, M.; Peña, A.; Volker, P.; Badger, J.; Di Bella, A.; Palomares, A.; *et al.* Comparing satellite SAR and wind farm wake models. *J. Phys. Conf. Ser.* **2015**, *625*, in press.
5. Hasager, C.B.; Mouche, A.; Badger, M.; Bingöl, F.; Karagali, I.; Driessenaar, T.; Stoffelen, A.; Peña, A.; Longépé, N. Offshore wind climatology based on synergetic use of Envisat ASAR, ASCAT and QuikSCAT. *Remote Sens. Environ.* **2015**, *156*, 247–263.
6. Quilfen, Y.; Chapron, B.; Elfouhaily, T.; Katsaros, K.; Tournadre, J. Observation of tropical cyclones by high-resolution scatterometry. *J. Geophys. Res.* **1998**, *103*, 7767–7786.
7. Katic, I.; Højstrup, J.; Jensen, N.O. A simple model for cluster efficiency. In Proceedings of the European Wind Energy Association Conference & Exhibition, Rome, Italy, 7–9 October 1986.
8. Mortensen, N.G.; Heathfield, D.N.; Myllerup, L.; Landberg, L.; Rathmann, O. *Getting Started with WAsP 9*; Tech. Rep. Risø-I-2571(EN); Risø National Laboratory: Roskilde, Denmark, 2007.
9. Jensen, N.O. *A Note on Wind Generator Interaction*; Tech. Rep. Risø-M-2411(EN); Risø National Laboratory: Roskilde, Denmark, 1983.
10. Skamarock, W.C.; Klemp, J.B.; Dudhia, J.; Gill, D.O.; Barker, D.M.; Duda, M.; Huang, X.Y.; Wang, W.; Powers, J.G. A description of the advanced research WRF version 3. *Tech. Rep.* **2008**, doi:10.5065/D68S4MVH.
11. Adams, A.S.; Keith, D.W. A wind farm parametrization for WRF. Available online: [http://www2.mmm.ucar.edu/wrf/users/workshops/WS2007/abstracts/5-5\\_Adams.pdf](http://www2.mmm.ucar.edu/wrf/users/workshops/WS2007/abstracts/5-5_Adams.pdf) (accessed on 2 June 2015).
12. Baidya Roy, S. Simulating impacts of wind farms on local hydrometeorology. *J. Wind Eng. Ind. Aerodyn.* **2011**, *99*, 491–498.
13. Blahak, U.; Goretzki, B.; Meis, J. A simple parametrisation of drag forces induced by large wind farms for numerical weather prediction models. In Proceedings of the European Wind Energy Conference & Exhibition 2010 (EWEC), Warsaw, Poland, 20–23 April 2010.
14. Jacobson, M.Z.; Archer, C.L. Saturation wind power potential and its implications for wind energy. *Proc. Natl. Acad. Sci. USA* **2012**, *109*, 15679–15684.
15. Fitch, A.; Olson, J.; Lundquist, J.; Dudhia, J.; Gupta, A.; Michalakes, J.; Barstad, I. Local and mesoscale impacts of wind farms as parameterized in a mesoscale NWP model. *Mon. Weather Rev.* **2012**, *140*, 3017–3038.
16. Volker, P.J.H.; Badger, J.; Hahmann, A.H.; Ott, S. The Explicit Wake Parametrisation V1.0: A wind farm parametrisation in the mesoscale model WRF. *GMDD* **2015**, *8*, 3481–3522.
17. Nakanishi, M.; Niino, H. Development of an improved turbulence closure model for the atmospheric boundary layer. *J. Meteorol. Soc. Jpn.* **2009**, *87*, 895–912.
18. Kain, J.S. The Kain-Fritsch convective parameterization: An update. *J. Appl. Meteorol. Climatol.* **2004**, *43*, 170–181.
19. Thompson, G.; Field, P.R.; Rasmussen, M.; Hall, W.D. Explicit forecasts of winter precipitation using an improved bulk micro- physics scheme. Part II: Implementation of a new snow parameterization. *Mon. Weather Rev.* **2008**, *136*, 5095–5115.

20. Mlaver, E.J.; Taubman, S.J.; Brown, P.D.; Iacono, M.J.; Clough, S.A. Radiative transfer for inhomogeneous atmosphere: RRTM, a validated corrected-k model for the long wave. *J. Geophys. Res.* **1997**, *102*, 16663–16682.
21. Dudhia, J. Numerical study of convection observed during the wind monsoon experiment using a mesoscale two-dimensional model. *J. Atmo. Sci.* **1989**, *46*, 3077–3107.
22. Chen, F.; Dudhia, J. Coupling an advanced land surface-hydrology model with the Penn State-NCAR MM5 modeling system. Part I: Model implementation and sensitivity. *Mon. Weather Rev.* **2001**, *129*, 569–585.
23. Uppala, S.M.; Kallberg, P.W.; Simmons, A.J.; Andrae, U.; Bechtold, V.; Fiorino, M.; Gibson, J.K.; Haseler, J.; Hernandez, A.; Kelly, G.A.; *et al.* The ERA-40 re-analysis. *Quart. J. R. Meteorol. Soc.* **2005**, *131*, doi:10.1256/qj.04.176.
24. Barthelmie, R.J.; Badger, J.; Pryor, S.C.; Hasager, C.B.; Christiansen, M.B.; Jørgensen, B.H. Offshore coastal wind speed gradients: Issues for the design and development of large offshore windfarms. *Wind Eng.* **2007**, *31*, 369–382.

© 2015 by the authors; licensee MDPI, Basel, Switzerland. This article is an open access article distributed under the terms and conditions of the Creative Commons Attribution license (<http://creativecommons.org/licenses/by/4.0/>).